

Hadron properties in the nuclear medium

Ryugo S. Hayano* and Tetsuo Hatsuda†

Department of Physics, The University of Tokyo, Bunkyo-ku, Tokyo 113-0033

The QCD vacuum shows the dynamical breaking of chiral symmetry. In the hot/dense QCD medium, the chiral order parameter such as $\langle \bar{q}q \rangle$ is expected to change as function of temperature T and density ρ of the medium, and its experimental detection is one of the main challenges in modern hadron physics. In this article, we discuss theoretical expectations for the in-medium hadron spectra associated with partial restoration of chiral symmetry and the current status of experiments with an emphasis on the measurements of properties of mesons produced in near-ground-state nuclei.

Contents

I. INTRODUCTION	1	V. VECTOR MESONS: ρ, ω, ϕ IN NUCLEI	21
A. QCD symmetries	2	A. Theoretical background	21
B. Dynamical breaking of chiral symmetry in the vacuum	3	B. Dileptons, why and how?	22
C. Chiral symmetry and hadron spectra	4	1. $\mu^+\mu^-$ -pair detection	22
II. CHIRAL SYMMETRY AND IN-MEDIUM HADRON SPECTRA	4	2. e^+e^- -pair detection	23
A. Chiral condensate in the medium	4	3. Combinatorial background	23
1. Finite temperature	5	C. High Energy Heavy Ion Reactions	23
2. Finite baryon density	5	1. Bevalac/SIS energies ($1 \sim 2A\text{GeV}$)	24
B. Spectral functions in the medium	5	DLS	24
1. In-medium pion	6	HADES	24
2. In-medium scalar meson	7	2. SPS energies ($40 \sim 200A\text{GeV}$)	25
3. In-medium vector meson	8	HELIOS/3 ($\mu^+\mu^-$)	25
C. Dynamical approaches to in-medium hadrons	8	CERES (NA45) (e^+e^-)	25
1. Naive quark model	8	NA60 ($\mu^+\mu^-$)	26
2. Nambu–Jona-Lasinio model	9	CERES (NA45/2) (e^+e^-)	27
3. QCD sum rules	9	3. RHIC ($\sqrt{s_{NN}} = 200\text{ GeV}$)	27
4. Hadron mass scaling	9	4. High energy heavy ion summary	28
5. Bag model	9	D. ρ, ω and ϕ mesons produced in nuclei with elementary reactions	28
6. Hadronic models	9	1. TAGX at INS Electron Synchrotron	28
7. Chiral effective theories	10	2. E325 experiment at KEK	28
8. Lattice QCD	10	E325 results on the ρ/ω mesons	29
III. PSEUDOSCALAR MESON: π IN NUCLEI	10	E325 results on the ϕ meson	30
A. Theoretical background	10	3. J-Lab E01-112 (g7) experiment	31
B. Pion-nucleus optical potential	11	4. CBELSA/TAPS experiment	32
1. s -wave and p -wave parts	11	E. Vector-meson in-medium width from transparency-ratio measurements	34
2. Pionic hydrogen - the πN scattering lengths at threshold	11	The ϕ attenuation	34
3. The missing repulsion problem	12	The ω attenuation	35
C. Deeply-bound pionic atom spectroscopy	12	VI. CONCLUDING REMARKS	35
1. Structure of deeply-bound pionic atoms	13	Pion	35
2. Formation of deeply-bound pionic atoms	14	σ meson	35
3. GSI S236 - Sn($d, {}^3\text{He}$)	14	Vector mesons	35
In-medium isovector scattering length b_1	16	ACKNOWLEDGMENTS	36
In-medium quark condensate	17	REFERENCES	36
IV. SCALAR MESON: σ IN NUCLEI	17	I. INTRODUCTION	
A. Theoretical background	17	Quantum chromodynamics (QCD), which is the color SU(3) gauge theory of quarks and gluons (Nambu, 1966), is now established as the fundamental theory of strong interactions. The Lagrangian density of QCD reads	
B. Experiments	18		
1. CHAOS	18		
2. Crystal Ball	19		
3. TAPS	19		
C. Final-state interaction (FSI) effects	21		

*Electronic address: hayano@phys.s.u-tokyo.ac.jp

†Electronic address: hatsuda@phys.s.u-tokyo.ac.jp

$$\mathcal{L} = \sum_q (\bar{q}_L i \not{D} q_L + \bar{q}_R i \not{D} q_R) - \frac{1}{4} G_{\mu\nu}^\alpha G_{\mu\nu}^\alpha + \sum_q (\bar{q}_L m q_R + \bar{q}_R m q_L) \quad (\text{I.1})$$

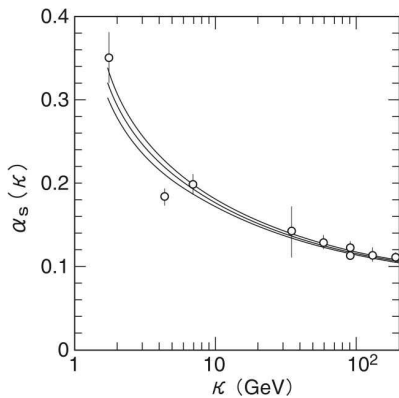


FIG. 1 The running coupling constant determined from τ decay, Υ decay, deep inelastic scattering, e^+e^- annihilation, and the Z -boson resonance shape and width (Amsler *et al.*, 2008).

where we focus on three light flavors $q = (u, d, s)$ with the mass matrix $m = \text{diag}(m_u, m_d, m_s)$ throughout this article. The quark field q belongs to the triplet representation of the color gauge group $SU(3)_C$. The right (left) handed quark $q_R = \frac{1}{2}(1 + \gamma_5)q$ ($q_L = \frac{1}{2}(1 - \gamma_5)q$) is the eigenstate of the chirality operator γ_5 with the eigenvalue $+1(-1)$. The covariant derivative is defined as $D_\mu \equiv \partial_\mu + ig t_C^\alpha \mathcal{A}_\mu^\alpha$ with g being the strong coupling constant, t_C^α being the $SU(3)_C$ generator and \mathcal{A}_μ^α being the color-octet gluon field. The field strength tensor of the gluon is defined as $G_{\mu\nu}^\alpha = \partial_\mu \mathcal{A}_\nu^\alpha - \partial_\nu \mathcal{A}_\mu^\alpha - gf_{\alpha\beta\gamma} \mathcal{A}_\mu^\beta \mathcal{A}_\nu^\gamma$ with $f_{\alpha\beta\gamma}$ being the structure constant of $SU(3)_C$. The QCD Lagrangian Eq.(I.1) is exactly invariant under the local $SU(3)_C$ gauge transformation of quarks and gluons.

The running coupling constant $g(\kappa)$ is defined as an effective coupling strength among quarks and gluons at the energy scale κ . Due to the asymptotic free nature of QCD, $g(\kappa)$ becomes small as κ increases (Gross, 2005; Politzer, 2005; Wilczek, 2005). This is explicitly seen in the two-loop perturbation theory as

$$\alpha_s(\kappa) \simeq \frac{1}{4\pi\beta_0 \ln(\kappa^2/\Lambda_{\text{QCD}}^2)} \cdot \left[1 - \frac{\beta_1}{\beta_0^2} \frac{\ln(\ln(\kappa^2/\Lambda_{\text{QCD}}^2))}{\ln(\kappa^2/\Lambda_{\text{QCD}}^2)} \right], \quad (\text{I.2})$$

where $\alpha_s(\kappa) \equiv \frac{g^2(\kappa)}{4\pi}$, $\beta_0 = (11 - \frac{2}{3}N_f)/(4\pi)^2$, $\beta_1 = (102 - \frac{38}{3}N_f)/(4\pi)^4$, N_f is the number of flavors and Λ_{QCD} is called the QCD scale parameter to be determined from experiment.

Fig.1 and Eq.(I.2) indicate that the running coupling constant increases and becomes strong at low energies $\kappa \sim \Lambda_{\text{QCD}} \sim 200$ MeV. This is the typical energy scale where various non-perturbative effects such as the confinement of quarks and gluons (Wilson, 2005) and the dynamical breaking of chiral symmetry (Nambu and Jona-Lasinio, 1961a,b)(Hatsuda and Kunihiro, 1994). Both effects are responsible for the formation of composite hadrons and nuclei and for the origin of their masses. In this article,

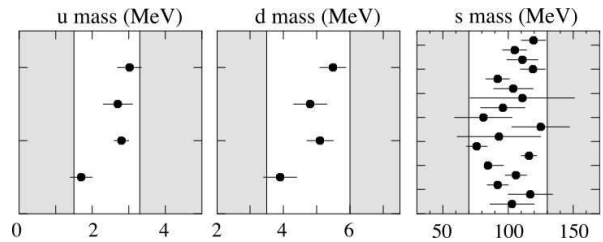


FIG. 2 The masses of u , d , and s quarks at the scale $\kappa = 2$ GeV constrained by various hadron masses using QCD sum rules and lattice QCD simulations (Amsler *et al.*, 2008).

we will focus on the dynamical breaking of chiral symmetry (DBCS) realized in the QCD vacuum and in the hot-dense QCD medium by using in-medium hadrons as useful probes of QCD matter.

A. QCD symmetries

Similar to the running coupling constant $\alpha_s(\kappa)$, the quark masses receive quantum corrections and become scale dependent, $m(\kappa)$. As seen from Fig.2, the current determination of the u and d quark masses show that they are about 50 to 100 smaller than the QCD intrinsic scale Λ_{QCD} , while the s quark mass is comparable to Λ_{QCD} . Therefore, it is legitimate to treat m_u/Λ_{QCD} and m_d/Λ_{QCD} as small expansion parameters.

In the limiting case where $m_{u,d} = 0$, which is called the $SU(2)$ chiral limit, the QCD Lagrangian Eq.(I.1) acquires an exact global symmetry called chiral symmetry under independent $SU(2)$ rotations of the left handed and right handed quarks: $q_L \rightarrow U_L q_L$ and $q_R \rightarrow U_R q_R$ with $U_{L,R}$ being the global $SU(2)$ matrices. Thus we have the exact QCD symmetry for $m_{u,d} = 0$,

$$\mathcal{G} = SU(3)_C \otimes SU(2)_L \otimes SU(2)_R \otimes U(1)_B, \quad (\text{I.3})$$

where $U(1)_B$ corresponds to the baryon number symmetry corresponding to the global phase rotation, $q_{L(R)} \rightarrow e^{i\theta} q_{L(R)}$. Although a similar phase rotation, $q_L \rightarrow e^{i\phi} q_L$ and $q_R \rightarrow e^{-i\phi} q_R$, looks like a symmetry of Eq.(I.1), it is broken explicitly by a quantum effect known as the axial anomaly. Currents associated with these ‘‘symmetries’’ are defined as $V_\mu^a = \bar{q}\gamma_\mu t^a q$ (the triplet vector current), $A_\mu^a = \bar{q}\gamma_\mu \gamma_5 t^a q$ (triplet axial-vector current), $V_\mu^0 = \bar{q}\gamma_\mu t^0 q$ (baryon current), $A_\mu^0 = \bar{q}\gamma_\mu \gamma_5 t^0 q$ (singlet axial current), where $t^{a=1,2,3} \equiv \tau^a/2$ with τ^a being the Pauli matrices and $t^0 \equiv \tau^0/2 \equiv 1/2$. The divergences of these currents are

$$\partial^\mu V_\mu^a = i\bar{q}[m, t^a]q, \quad (\text{I.4})$$

$$\partial^\mu A_\mu^a = i\bar{q}\{m, t^a\}\gamma_5 q, \quad (\text{I.5})$$

$$\partial^\mu V_\mu^0 = 0, \quad (\text{I.6})$$

$$\partial^\mu A_\mu^0 = i\bar{q}m\gamma_5 q - 2\frac{\alpha_s}{4\pi} G_{\alpha}^{\mu\nu} \tilde{G}_{\mu\nu}^\alpha, \quad (\text{I.7})$$

with $\tilde{G}_{\mu\nu}^\alpha = \frac{1}{2}\epsilon_{\mu\nu\lambda\rho}G_\alpha^{\lambda\rho}$ being the dual field strength of the gluon. $[,]$ and $\{ , \}$ are the commutator and the anti-commutator in the flavor-space, respectively. For later convenience, we define the scalar and pseudo-scalar density as

$$S^0 = \bar{q}t^0q, \quad S^a = \bar{q}t^aq, \quad (\text{I.8})$$

$$P^0 = \bar{q}i\gamma_5t^0q, \quad P^a = \bar{q}i\gamma_5t^aq, \quad (\text{I.9})$$

From the time component of the currents, generators of the chiral transformation are defined as $Q^a(t) = \int V_0^a(t, \mathbf{x})d^3x$ and $Q_5^a(t) = \int A_0^a(t, \mathbf{x})d^3x$. Then the bilinear quark operators defined above obey the following relations under the axial transformation Q_5^a ($a = 1, 2, 3$);

$$[Q_5^a(t), V_\mu^b(t, \mathbf{x})] = +i\epsilon_{abc}A_\mu^c(t, \mathbf{x}), \quad (\text{I.10})$$

$$[Q_5^a(t), A_\mu^b(t, \mathbf{x})] = +i\epsilon_{abc}V_\mu^c(t, \mathbf{x}), \quad (\text{I.11})$$

$$[Q_5^a(t), S^0(t, \mathbf{x})] = +iP^a(t, \mathbf{x}), \quad (\text{I.12})$$

$$[Q_5^a(t), P^0(t, \mathbf{x})] = -iS^a(t, \mathbf{x}), \quad (\text{I.13})$$

$$[Q_5^a(t), S^b(t, \mathbf{x})] = +i\delta_{ab}P^0(t, \mathbf{x}), \quad (\text{I.14})$$

$$[Q_5^a(t), P^b(t, \mathbf{x})] = -i\delta_{ab}S^0(t, \mathbf{x}). \quad (\text{I.15})$$

In the past few years, remarkable progress was made in calculating the hadron spectra on the basis of lattice QCD simulations with dynamical u, d, s quarks. This progress was achieved partly because the supercomputer speed is doubled every 1.2 years and partly because of new simulation algorithms: The lattice QCD simulations for quark masses very close to the physical point are now possible in the Wilson fermion formalism (Aoki *et al.*, 2008; Dürr *et al.*, 2008). Shown in Fig.3 is an example of the lattice results for meson and baryon masses extrapolated to the physical quark masses using the simulation data in the interval, $\frac{1}{2}(m_u + m_d)(\kappa = 2\text{GeV}) = 3.5 \text{ MeV} - 67 \text{ MeV}$ (corresponding to $m_\pi = 156 \text{ MeV} - 702 \text{ MeV}$). The experimental data are reproduced with 3% accuracy. The simulations right at the physical quark masses will be performed in the very near future.

B. Dynamical breaking of chiral symmetry in the vacuum

Even if QCD in the SU(2) chiral limit has the symmetries of Eq.(I.3), the ground state of the system may break some of the symmetries dynamically. Let us consider the QCD vacuum $|0\rangle$ at zero temperature and density. Assuming that the vacuum is Lorentz invariant and taking into account the fact that QCD does not allow dynamical breaking of parity and vector symmetry in the vacuum (Vafa and Witten, 1984), we have the following possibility of the symmetry breaking pattern;

$$\text{SU}(2)_L \times \text{SU}(2)_R \rightarrow \text{SU}(2)_{L+R} \equiv \text{SU}(2)_V. \quad (\text{I.16})$$

In terms of the generators of the vector and axial-vector rotations, such a vacuum state is characterized as

$$Q^a|0\rangle = 0, \quad Q_5^a|0\rangle \neq 0. \quad (\text{I.17})$$

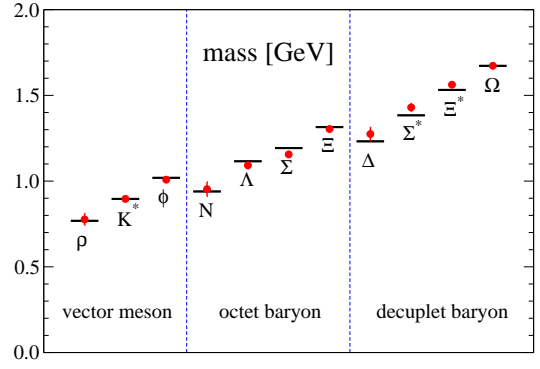


FIG. 3 Light hadron spectrum obtained from lattice QCD simulations with dynamical u, d, s quarks in the Wilson fermion formalism. The hadron masses are extrapolated to the physical quark masses (determined by m_π, m_K and m_Ω) using the data in the interval, $\frac{1}{2}(m_u + m_d)(\kappa = 2\text{GeV}) = 3.5 \text{ MeV} - 67 \text{ MeV}$. The spatial lattice volume V and the lattice spacing a are $(2.9 \text{ fm})^3$ and 0.09 fm , respectively. Horizontal bars denote the experimental values (Aoki *et al.*, 2008).

Strictly speaking, we need to take the SU(2) chiral limit $m_{u,d} \rightarrow 0$ after taking the thermodynamic limit $V \rightarrow 0$ to make the matrix elements of Q_5^a well defined. This is similar to the case of the spin system where the external magnetic field plays the role of $m_{u,d}$.

At this point, it is in order to mention general definition of the order parameter. Consider a symmetry group \mathcal{G} and its generator Q . If there is an operator Φ such that $\langle [iQ, \Phi] \rangle_0 (\equiv \langle 0|[iQ, \Phi]|0\rangle) \neq 0$, this expectation value is called the order parameter. If the vacuum is symmetric under Q , the order parameter becomes zero. On the other hand, if the vacuum is not symmetric under Q , there exists a Nambu-Goldstone boson having the same quantum number as Φ . Note that the order parameter is not unique for a given \mathcal{G} : one can introduce higher dimensional order parameters in principle to characterize the system (Kogan *et al.*, 1999; Watanabe *et al.*, 2004).

For the symmetry breaking pattern as Eq.(I.16), Q is identified as Q_5^a , and a simplest choice of Φ is P^a . Then, it leads to the order parameter $\langle S^0 \rangle_0$. Recent lattice QCD simulation of the chiral condensate using overlap Dirac fermion with dynamical u, d, s quarks indicates (Fukaya *et al.*, 2009)

$$\langle S^0 \rangle_0 = \frac{1}{2} \langle \bar{u}u + \bar{d}d \rangle_0 = -(242(04)_{-18}^{+19} \text{ MeV})^3, \quad (\text{I.18})$$

where the renormalization scale is taken to be $\kappa = 2 \text{ GeV}$ with the statistical and systematic errors in parentheses. This result implies that the QCD vacuum is the Bose-Einstein condensate of quark-anti-quark pairs $\langle \bar{q}q \rangle_0 = \langle (\bar{q}_L q_R + \bar{q}_R q_L) \rangle_0$ and has the power to change left handed quarks to right handed quarks and vice versa: Namely the condensate induces a dynamical quark mass. Since quarks are confined, it is not possible to isolate a single quark to measure the dynamical quark mass. Nevertheless, there is indirect evidence that the quarks inside hadrons have an effective mass (constituent quark

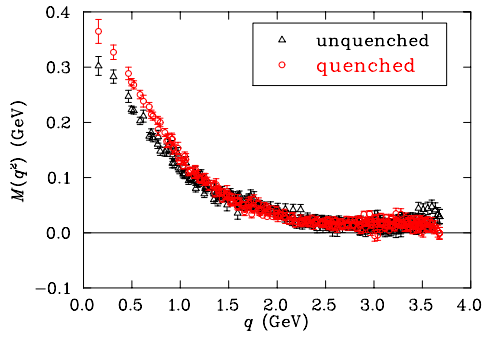


FIG. 4 Effective quark mass M as a function of the Euclidean momentum q obtained from lattice QCD simulations without dynamical quarks (quenched) and with three dynamical quarks (unquenched) (Bowman *et al.*, 2005).

mass) $M \sim 350$ MeV from the phenomenological description of hadrons. The effective quark mass near zero Euclidean momentum in lattice QCD simulations with Landau gauge fixing leads to a similar value as shown in Fig.4.

C. Chiral symmetry and hadron spectra

The Nambu-Goldstone (NG) bosons associated with the DBCS of SU(2) chiral symmetry are nothing but the charged and neutral pions. Moreover, the partially conserved axial current (PCAC) relation, Eq.(I.5), leads to the Gell-Mann–Oakes–Renner (GOR) relation (Gell-Mann *et al.*, 1968) which relates the pion masses to the quark masses as

$$f_\pi^2 m_{\pi^\pm}^2 = -\hat{m} \langle \bar{u}u + \bar{d}d \rangle_0 + O(\hat{m}^2), \quad (\text{I.19})$$

$$f_\pi^2 m_{\pi^0}^2 = -\langle m_u \bar{u}u + m_d \bar{d}d \rangle_0 + O(\hat{m}^2). \quad (\text{I.20})$$

Here $\hat{m} = (m_u + m_d)/2$ is the averaged mass of u and d quarks, $f_\pi (= 92.4$ MeV) is the pion decay constant, and $m_{\pi^\pm} \simeq 140$ MeV ($m_{\pi^0} \simeq 135$ MeV) is the charged (neutral) pion mass. Using these values together with the quark masses in Fig.2, we obtain the finite chiral condensate comparable to Eq.(I.18).

Further experimental evidence of DBCS is obtained from the observed meson spectra. If chiral symmetry is not broken, $Q_5^a|0\rangle = 0$, vacuum expectation values of all the commutators, $\langle [Q_5^{a_n}, \dots [Q_5^{a_2}, [Q_5^{a_1}, \Phi]] \dots] \rangle_0$, should vanish for an arbitrary operator Φ . The contraposition of this statement with $n = 2$ and $\Phi = S^a(x)S^a(y), V_\mu^a(x)V_\nu^b(y)$ leads to a statement that DBCS must occur if the correlation functions of the chiral partners are not degenerate. Namely,

$$\langle S^a(x)S^a(y) - P^a(x)P^a(y) \rangle_0 \neq 0 \rightarrow Q_5^a|0\rangle \neq 0, \quad (\text{I.21})$$

$$\langle V_\mu^a(x)V_\nu^a(y) - A_\mu^a(x)A_\nu^a(y) \rangle_0 \neq 0 \rightarrow Q_5^a|0\rangle \neq 0. \quad (\text{I.22})$$

Experimentally, the pion (the pseudo-scalar meson) does not have a scalar partner at the same mass, and the ρ -meson (the vector meson) does not have an axial-vector

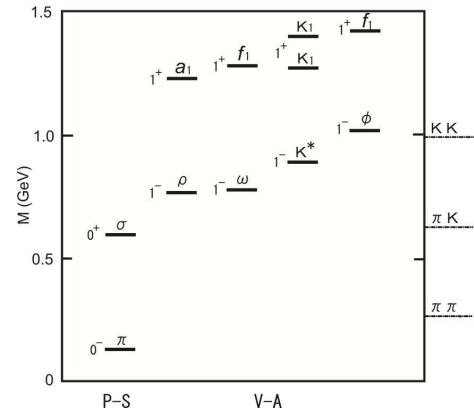


FIG. 5 Light scalar (S), pseudo-scalar (P), vector (V) and axial-vector (A) mesons. Their spin and parity are denoted as J^P . Threshold of the $\pi\pi$, πK and KK decays are also shown (Yagi *et al.*, 2005).

partner at the same mass, which are the direct evidences of DBCS. Such non-degeneracy is also seen in other channels, e.g. ω , K^* and ϕ as illustrated in Fig.5.

II. CHIRAL SYMMETRY AND IN-MEDIUM HADRON SPECTRA

Connections between properties of the QCD vacuum and hadronic correlation functions as discussed in Sec.I.B and Sec.I.C can be generalized to QCD at finite temperature and density. In this section, we will summarize such theoretical connections with special emphasis on the pion, the scalar meson, and vector mesons in the medium.

A. Chiral condensate in the medium

Let us now consider how the simplest chiral order parameter $\langle \bar{q}q \rangle$ changes its value inside the hot and/or dense medium. Exact formula for the in-medium chiral condensate in terms of the QCD partition function Z at finite temperature T and the baryon chemical potential μ is given by

$$\langle \bar{q}q \rangle_{T,\mu} = \frac{1}{Z} \text{Tr} \left[\bar{q}q e^{-K_{\text{QCD}}/T} \right] = -\frac{\partial P(T,\mu)}{\partial m_q}, \quad (\text{II.23})$$

where

$$Z(T,\mu) = \text{Tr} \left[e^{-K_{\text{QCD}}/T} \right] = e^{P(T,\mu)V/T}, \quad (\text{II.24})$$

$$K_{\text{QCD}} = H_{\text{QCD}}^{m=0} + \int (\bar{q}mq - q^\dagger \mu q) d^3x, \quad (\text{II.25})$$

with $H_{\text{QCD}}^{m=0}$ being the QCD Hamiltonian without the quark mass term.

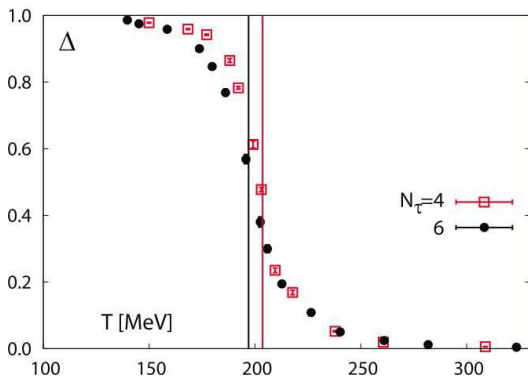


FIG. 6 Normalized chiral condensate $\Delta = [(\bar{u}u)_T - (\hat{m}/m_s)\langle\bar{s}s\rangle_T]/[(\bar{u}u)_0 - (\hat{m}/m_s)\langle\bar{s}s\rangle_0]$ as a function of T for two different lattice spacings, $a = 0.24$ fm ($N_\tau = 4$) and $a = 0.17$ fm ($N_\tau = 6$), calculated by the lattice QCD simulations with dynamical u, d, s quarks in the staggered fermion formalism (Cheng *et al.*, 2008).

1. Finite temperature

Eq.(II.23) can be evaluated analytically in some special cases. For example, in the two-flavor system ($N_f = 2$, i.e., $m_u = m_d < \infty, m_s = \infty$) at low T with $\mu = 0$, thermal pions are the dominant contributor to the pressure. In the leading order of the virial expansion by the pion number density, we have (Gerber and Leutwyler, 1989)

$$\frac{\langle\bar{q}q\rangle_T}{\langle\bar{q}q\rangle_0}\Big|_{N_f=2} \simeq 1 - \frac{3}{4}\Theta(T), \quad (\text{II.26})$$

$$\Theta(T) = \frac{T^2}{6f_\pi^2}B_1(m_\pi/T), \quad (\text{II.27})$$

where $\int \frac{d^3k}{(2\pi)^3 2\varepsilon_k} n_B(k; T) = \frac{T^2}{24}B_1(m_\pi/T)$ with n_B being the Bose-Einstein distribution and $\varepsilon_k = \sqrt{\mathbf{k}^2 + m_\pi^2}$. Eq.(II.27) shows a clear tendency that the magnitude of the chiral condensate decreases as T increases. However, for $T > 150$ MeV, the interaction among pions and the contribution from other mesons become important and the estimate based on Eq.(II.27) is not reliable. The two-flavor system at extremely high T with $\mu = 0$ can be also evaluated because the thermal quarks and gluons are the dominant contributor to the pressure due to asymptotic freedom. In the leading order of $\alpha_s(\kappa \sim T)$, we have $\langle\bar{q}q\rangle_T \simeq \frac{1}{2}m_q T^2$ ($q = u, d$), so that the chiral condensate vanishes in the chiral limit. Lattice QCD simulations at finite T in Fig.6 indeed show a decrease of the normalized chiral condensate for u, d quarks with a rapid crossover around $T \simeq 200$ MeV (Cheng *et al.*, 2008).

2. Finite baryon density

A useful formula for the chiral condensate at fixed baryon density ρ with $T = 0$ is obtained from Eq.(II.23) by using the thermodynamic relations; $P + \varepsilon = \sum_q \mu_q \rho_q$,

$\rho_q = \frac{\partial}{\partial \mu_q} P$ and $\mu_q = \frac{\partial}{\partial \rho_q} \varepsilon$ with ε being the energy density of the system:

$$\langle\bar{q}q\rangle_\rho = \langle\bar{q}q\rangle_0 + \rho \frac{d}{dm_q} \left(\frac{E}{A} \right), \quad (\text{II.28})$$

where $\rho (= \sum_q \rho_q)$, A and E are the total baryon density, the total baryon number, and the total energy, respectively. There is an alternative derivation of this formula using the Hellmann-Feynman theorem (Cohen *et al.*, 1992).

For two-flavor nuclear matter with equal numbers of protons and neutrons, the leading order of the virial expansion in terms of the baryon density reads (Cohen *et al.*, 1992; Drukarev and Levin, 1991; Hatsuda and Lee, 1992)

$$\frac{\langle\bar{u}u + \bar{d}d\rangle_\rho}{\langle\bar{u}u + \bar{d}d\rangle_0} \simeq 1 - \frac{\sigma_{\pi N}}{f_\pi^2 m_\pi^2} \rho F_1(k_F/m_N), \quad (\text{II.29})$$

$$\frac{\langle\bar{s}s\rangle_\rho}{\langle\bar{s}s\rangle_0} \simeq 1 - y \frac{\sigma_{\pi N}}{f_\pi^2 m_\pi^2} \rho F_1(k_F/m_N). \quad (\text{II.30})$$

Here $\sigma_{\pi N} = \hat{m}\langle N|\bar{u}u + \bar{d}d|N\rangle$ is the πN sigma-term, and $y = 2\langle\bar{s}s\rangle_N/\langle\bar{u}u + \bar{d}d\rangle_N$ is the strangeness content of the nucleon. Also, $\int \frac{d^3k}{(2\pi)^3 2E_k} \theta(k_F - |\mathbf{k}|) = \frac{k_F^3}{6\pi^2} F_1(k_F/m_N)$ with k_F being the Fermi momentum and $E_k = \sqrt{\mathbf{k}^2 + m_N^2}$. The low density expansion of F_1 reads $F_1(x) = 1 - \frac{3}{10}x^2 + \frac{9}{56}x^4 + \dots$ (Hatsuda *et al.*, 1995). Using the empirical values, $\sigma_{\pi N} = 45 \pm 10$ MeV and $y = 0.12 - 0.22$ (Gasser *et al.*, 1991; Hatsuda and Lee, 1992) the right hand side of Eq.(II.29) gives almost a 35 % reduction of $\langle\bar{q}q\rangle_\rho$ at nuclear matter density $\rho_0 = 0.17 \text{ fm}^{-3}$. This leading order result together with a calculation of higher order corrections on the basis of in-medium chiral perturbation theory are shown in Fig.7 for nuclear matter and neutron matter (Kaiser and Weise, 2009).

The change of the chiral condensate induced by the strong electric and magnetic fields and strong color electric and magnetic fields is also an interesting subject which may be relevant to the physics of relativistic heavy ion collisions and the structure of compact stars with high magnetic field (Klevansky, 1992; Miransky, 2002; Suganuma and Tatsumi, 1991).

The experimental detection of the change of chiral condensate in the hot and/or dense medium is one of the most interesting challenges in modern hadron physics. Possible tools are hadron-nucleus and photon-nucleus reactions, heavy-ion collisions, and deeply bound mesic atoms and mesic nuclei, which are summarized in the later chapters of this article.

B. Spectral functions in the medium

In the hot and/or dense environment, all the hadrons including the pion undergo spectral changes due to their

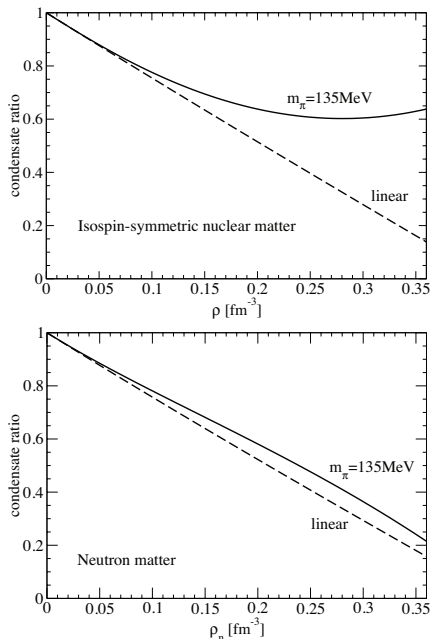


FIG. 7 Comparison of the linear density approximation of the chiral condensate (dashed lines) and the results with higher order terms originating from nucleon-nucleon correlations calculated by the in-medium chiral perturbation theory (solid lines) (Kaiser and Weise, 2009).

strong interactions with the medium. Therefore, it is not enough to talk about the “mass” and “width” of the hadrons, but we need to study the hadronic spectral functions. For mesic resonances coupled to the composite operator $\mathcal{O}(t, \mathbf{x}) = \bar{q}(t, \mathbf{x})\Gamma q(t, \mathbf{x})$ with Γ being an arbitrary combination of Dirac and flavor matrices, we have the spectral decomposition of the retarded correlation as

$$G^R(\omega, \mathbf{k}) = i\text{F.T.}\langle R(\mathcal{O}(t, \mathbf{x})\mathcal{O}^\dagger(0)) \rangle, \quad (\text{II.31})$$

$$= \int_0^\infty \frac{\rho_{\mathcal{O}}(u, \mathbf{k})}{u^2 - (\omega + i\delta)^2} du^2, \quad (\text{II.32})$$

where F.T. stands for the fourier transform, $R(A(t, \mathbf{x})B(t', \mathbf{y})) = \theta(t - t')[A(t, \mathbf{x}), B(t', \mathbf{y})]$ is the retarded product of the operators A and B , and $\langle \cdot \rangle$ implies the expectation value at finite T and μ . The spectral function, $\rho_{\mathcal{O}}(\omega, \mathbf{k})$, has all the information of the states having the same quantum numbers with the operator \mathcal{O} . In particular, P^a and V_μ^a are the relevant operators for studying the in-medium pion and the ρ -meson, respectively.

1. In-medium pion

The Nambu-Goldstone theorem which guarantees massless pions in the QCD vacuum in the chiral limit holds also in the medium. Indeed, by considering the

correlation,

$$\Pi = \int d^4x \partial^\mu \langle R[A_\mu^a(t, \mathbf{x})P^b(0)] \rangle, \quad (\text{II.33})$$

the following sum rule can be derived (Yagi *et al.*, 2005):

$$2m \int_0^\infty \frac{\rho_P^{ab}(\omega, \mathbf{0})}{\omega^2} d\omega^2 = -\delta^{ab}\langle S^0 \rangle, \quad (\text{II.34})$$

where we considered a two-flavor system ($m = m_u = m_d < \infty, m_s = \infty$) for simplicity. ρ_P^{ab} corresponds to the spectral function associated with $\Pi_P^{ab}(x) = \langle R(P^a(t, \mathbf{x})P^b(0)) \rangle$. To have a non-zero chiral condensate in the r.h.s. of Eq.(II.34) in the chiral limit $m \rightarrow 0$, the spectral function must have a pole, $\rho_P^{ab}(\omega, \mathbf{0})|_{m \rightarrow 0} \sim \delta^{ab}[C\delta(\omega^2 - am) + \dots]$, so that m in the numerator is canceled by this pole in the chiral limit. This means nearly massless pions exist even in the medium as long as DBCS takes place.

In the leading order of the virial expansion at $T \neq 0$ with $\mu = 0$, the self-energy of the in-medium pion is dictated by the forward pion-pion scattering amplitude which vanishes in the chiral limit. In this case, the pion is still a real pole with the mass $m_\pi(T)$ and the decay constant $f_\pi^t(T)$ (Goity and Leutwyler, 1989; Pisarski and Tytgat, 1996; Toublan, 1997):

$$\left(\frac{m_\pi(T)}{m_\pi}\right)^2 = 1 + \frac{1}{4}\Theta(T), \quad (\text{II.35})$$

$$\left(\frac{f_\pi^t(T)}{f_\pi}\right)^2 = 1 - \Theta(T). \quad (\text{II.36})$$

Here, the in-medium pion decay constant $f_\pi^t(T)$ is defined by the residue of the pion pole of the correlation function of $A_{\mu=0}^a$. Since the Lorentz symmetry does not hold in the rest frame of the medium, a difference arises between the temporal residue f_π^t and the spatial residue f_π^s in general, although they are equal in the leading order of the virial expansion at finite T . Combining Eq.(II.36) and $\langle \bar{q}q \rangle_T$ in Eq.(II.26), the GOR relation turns out to hold in the dilute pion gas at low T (Pisarski and Tytgat, 1996; Toublan, 1997):

$$\frac{(f_\pi^t(T)m_\pi(T))^2}{\hat{m}\langle \bar{u}u + \bar{d}d \rangle_T} \simeq -1, \quad (\text{II.37})$$

which was originally noticed in the Nambu–Jona-Lasinio model at finite T (Hatsuda and Kunihiro, 1987b).

In the case $\rho \neq 0$ with $T = 0$, the in-medium pion properties at low baryon density is determined by the pion-nucleon forward scattering amplitude which is dictated by several low energy constants (Meissner *et al.*, 2002; Thorsson and Wirzba, 1995). For the symmetric two-flavor nuclear matter, we have

$$\left(\frac{m_\pi(\rho)}{m_\pi}\right)^2 = 1 + \frac{2}{f_\pi^2} \left(2c_1 - c_2 - c_3 + \frac{g_A^2}{8m_N} \right) \rho \quad (\text{II.38})$$

$$\left(\frac{f_\pi^t(\rho)}{f_\pi}\right)^2 = 1 + \frac{2}{f_\pi^2} \left(c_2 + c_3 - \frac{g_A^2}{8m_N} \right) \rho, \quad (\text{II.39})$$

$$\left(\frac{f_\pi^s(\rho)}{f_\pi}\right)^2 = 1 - \frac{2}{f_\pi^2} \left(c_2 - c_3 + \frac{g_A^2}{8m_N} \right) \rho. \quad (\text{II.40})$$

Using Eq.(II.29) and a relation $\sigma_{\pi N} \simeq -4c_1 m_\pi^2$, the GOR relation is shown to hold at low density:

$$\frac{(f_\pi^t(\rho)m_\pi(\rho))^2}{\hat{n}\langle\bar{u}u + \bar{d}d\rangle_\rho} \simeq -1. \quad (\text{II.41})$$

With the empirical values, $c_1 = -0.81 \pm 0.12 \text{ GeV}^{-1}$, $c_2 = 3.2 \pm 0.25 \text{ GeV}^{-1}$, $c_3 = -4.70 \pm 1.16 \text{ GeV}^{-1}$, $f_\pi = 92.4(3) \text{ MeV}$ and $g_A = 1.2695(29) \text{ MeV}$, one finds $f_\pi^t(\rho)/f_\pi = 1 - (0.26 \pm 0.04)(\rho/\rho_0)$, $f_\pi^s(\rho)/f_\pi = 1 - (1.23 \pm 0.07)(\rho/\rho_0)$, $\langle\bar{q}q\rangle_\rho/\langle\bar{q}q\rangle_0 = 1 - (0.35 \pm 0.09)(\rho/\rho_0)$. Note that, in asymmetric nuclear matter, there is splitting between m_{π^-} , m_{π^+} and m_{π^0} : For example, $N/Z = 1.5$ at $\rho = \rho_0 = 0.17 \text{ fm}^{-3}$, there is approximately a +18 MeV shift for π^- , a -12 MeV shift for π^+ , and a +2 MeV shift for π^0 (Meissner *et al.*, 2002). A possible problem of the linear density formula Eq.(II.40) is that f_π^s vanishes even below nuclear matter density.

In the leading order of baryon density and in the SU(2) chiral limit, one can formulate two different representations of the in-medium change of the chiral condensate in terms of the physical observables:

$$\frac{\langle\bar{q}q\rangle_\rho}{\langle\bar{q}q\rangle_0} \simeq \left(\frac{f_\pi^t(\rho)}{f_\pi}\right)^2 \left(\frac{m_\pi(\rho)}{m_\pi}\right)^2, \quad (\text{II.42})$$

$$\simeq Z_\pi^{1/2}(\rho) \left(\frac{b_1}{b_1(\rho)}\right)^{1/2}. \quad (\text{II.43})$$

The first one is the in-medium GOR relation Eq.(II.41), while the second one is a combination of the in-medium Tomozawa-Weinberg relation (Kolomeitsev *et al.*, 2003b), $b_1/b_1(\rho) \simeq (f_\pi^t(\rho)/f_\pi)^2$, and the in-medium Glashow-Weinberg relation (Jido *et al.*, 2008), $\langle\bar{q}q\rangle_\rho/\langle\bar{q}q\rangle_0 \simeq Z_\pi^{1/2}(\rho) \times (f_\pi^t(\rho)/f_\pi)$. Here $b_1(\rho)$ (b_1) is the isovector pion-nucleus (pion-nucleon) scattering length in the chiral limit and $Z_\pi(\rho)$ is the in-medium change of the pion pole residue of the correlation function of the pseudo-scalar operator $P^a(x)$. The slope of $Z_\pi(\rho)$ as a function of ρ at low density is related to the isoscalar pion-nucleon scattering amplitude, while $b_1(\rho)$ is related to the energy levels of the deeply bound π^- -atom. Experimental data at $\rho < \rho_0$ indicate $Z_\pi(\rho) < 1$ and $b_1/b_1(\rho) < 1$, so that the chiral condensate indeed decreases at finite baryon density.

2. In-medium scalar meson

The light scalar-isoscalar meson has been customarily called the σ . Since it has the same quantum number as the vacuum, σ is analogous to the Higgs boson H in the electro-weak (EW) theory. The σ

may be interpreted as the excitation associated with the amplitude fluctuation of the chiral condensate $\langle\bar{q}q\rangle$ (Nambu, 1960; Nambu and Jona-Lasinio, 1961a,b) (Gell-Mann and Levy, 1960) (Delbourgo and Scadron, 1982; Weinberg, 1990). However, there is a marked difference between H and σ : In the EW theory, the NG bosons associated with spontaneous symmetry breaking $\text{SU}(2) \times \text{U}(1)_Y \rightarrow \text{U}(1)_{\text{em}}$ are absorbed into the gauge bosons, while the NG bosons in QCD (the phase fluctuation of $\langle\bar{q}q\rangle$) are nothing but physical pions. Therefore, σ is allowed to have s -wave decay into two pions as long as $m_\sigma > 2m_\pi$. Thus σ should be a very broad resonance even if it exists.

Because of the above reason, it has been long debated whether there is unambiguous experimental evidence of such a light and broad resonance in $\pi-\pi$ scattering, $\gamma-\gamma$ collision, heavy meson decays, and so on (Pennington, 2007). Recently, an analysis based on the model independent Roy equation for the partial wave amplitude in the scalar-isoscalar channel, $t_{J=0}^{I=0}(s)$, has been carried out using precise inputs of the $\pi-\pi$ scattering lengths obtained from chiral perturbation theory. The mass and the width of σ corresponding to the second sheet pole are then deduced with high accuracy (Caprini *et al.*, 2006; Leutwyler, 2008):

$$m_\sigma = 441_{-8}^{+16} \text{ MeV}, \quad \Gamma_\sigma = 544_{-25}^{+18} \text{ MeV}. \quad (\text{II.44})$$

Although the existence of σ is established, its quark-gluon structure is still unknown and is actively studied theoretically, experimentally (Pennington, 2007) and also numerically in lattice QCD simulations (Kunihiro *et al.*, 2009; Prelovsek, 2008).

The medium modification of σ has not been established yet even at low temperature and density unlike the case of the pion. Nevertheless, we may expect from general grounds that there would be a partial degeneracy between σ and π if the system approaches to the point of chiral symmetry restoration (Hatsuda and Kunihiro, 1985, 1987a,b) (Bernard *et al.*, 1987) (Chiku and Hatsuda, 1998b; Hatsuda and Kunihiro, 2001; Hatsuda *et al.*, 1999). At finite T , such a chiral degeneracy can be detected, e.g., by the thermal hadronic susceptibilities associated with the operator $\mathcal{O}(\tau, \mathbf{x})$ defined in the Euclidean time τ ;

$$\begin{aligned} \chi_\sigma &= \int_0^{1/T} d\tau \int d^3x \langle \mathcal{O}(\tau, \mathbf{x}) \mathcal{O}^\dagger(0, \mathbf{0}) \rangle_T, \quad (\text{II.45}) \\ &= \int_0^\infty d\omega^2 \frac{\rho_\sigma(\omega)}{\omega^2}. \quad (\text{II.46}) \end{aligned}$$

Shown in Fig.8 is the lattice QCD simulation of $\sqrt{1/\chi_\sigma}$ with dynamical quarks in two-flavor (Karsch, 2002). One can see the degeneracy between the susceptibilities in the σ channel and the π channel as T increases to the left. Also, $\sqrt{1/\chi_\sigma}$ for σ is smaller than that for a_0 (scalar-isovector meson, traditionally called δ) at low T , which indicates that the spectral strength in the σ channel has

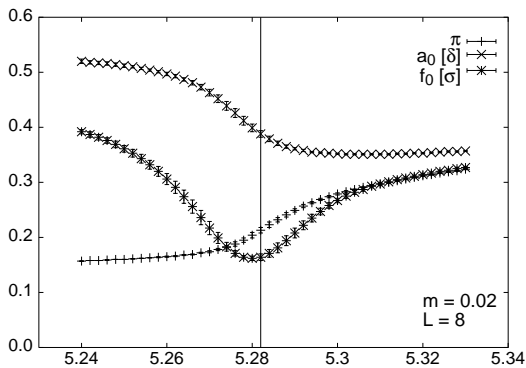


FIG. 8 Thermal susceptibilities in three different channels (π , σ , and a_0) for two-flavor QCD with staggered fermion on the $8^3 \times 4$ lattice with $m_{u,d} = 0.02$. The vertical (horizontal) axis denotes $\sqrt{1/\chi_C}$ (the lattice coupling : $6/g^2$) (Karsch, 2002). Low (high) T corresponds to the left (right) of the figure.

more weight in the low frequency region (σ is lighter than a_0) as can be seen from Eq.(II.46). Splitting between a_0 and π even when σ - π degeneracy is realized at high T reflects the explicit breaking of $U(1)_A$ symmetry. We note that the close relevance of the scalar-isoscalar susceptibility at finite baryon density to the nuclear matter properties is also pointed out (Ericson and Chanfray, 2007).

3. In-medium vector meson

Unlike the case of Eq.(II.34) which relates the chiral condensate $\langle \bar{q}q \rangle$ and the spectral function in the pion channel, no such relation is known in the vector channel. Still, one can derive useful relations by using the in-medium generalization of the QCD sum rules (Hatsuda *et al.*, 1993; Hatsuda and Lee, 1992). In particular, the in-medium Weinberg relations (Kapusta and Shuryak, 1994) for the vector and axial-vector spectral functions at zero spatial momentum read

$$\int_0^\infty \frac{d\omega^2}{\omega^2} (\rho_V(\omega) - \rho_A(\omega)) = 0, \quad (\text{II.47})$$

$$\int_0^\infty d\omega^2 (\rho_V(\omega) - \rho_A(\omega)) = 0, \quad (\text{II.48})$$

$$\int_0^\infty d\omega^2 \omega^2 (\rho_V(\omega) - \rho_A(\omega)) = -\frac{4\pi}{3} \alpha_s \langle \mathcal{O}_{4q} \rangle, \quad (\text{II.49})$$

where $\mathcal{O}_{4q} = \mathcal{O}_\mu^\mu + 2\mathcal{O}^{00}$ with

$$\mathcal{O}_{\mu\nu} = \frac{4}{3} (\bar{q}_L \gamma_\mu t_C^\alpha t_F^\alpha q_L) (\bar{q}_R \gamma_\nu t_C^\alpha t_F^\alpha q_R). \quad (\text{II.50})$$

Note that there are longitudinal and transverse spectral functions in the medium, but they coincide at zero spatial momentum, so that such a distinction is not made in the above formula. As is obvious from Eq.(II.50), the

DBCS in the vector and axial-vector channels is manifested as the higher dimensional four-quark operator and not by the simple bilinear operator $\bar{q}q = \bar{q}_L q_R + \bar{q}_R q_L$: The in-medium changes of $\langle \mathcal{O}_{4q} \rangle$ and $\langle \bar{q}q \rangle^2$ are different in general (Eletsky, 1993; Hatsuda *et al.*, 1993). At finite T with zero baryon density, it has been proven that there is no exotic phase in which $\langle \bar{q}q \rangle = 0$ and $\langle \mathcal{O}_{4q} \rangle \neq 0$ take place simultaneously (Kogan *et al.*, 1999). However, such a phase is not ruled out at finite baryon density and is indeed realized in the color superconducting phase (Hatsuda *et al.*, 2008).

The spectral modifications of vector and axial-vector channels at low T with zero μ are realized as a mixing of the two channels due to thermal pions. In the leading order of the virial expansion in the two-flavor system, one finds (Dey *et al.*, 1990)

$$\rho_V = (1 - \Theta(T))\rho_V^{\text{vac}} + \Theta(T)\rho_A^{\text{vac}}, \quad (\text{II.51})$$

$$\rho_A = (1 - \Theta(T))\rho_A^{\text{vac}} + \Theta(T)\rho_V^{\text{vac}}, \quad (\text{II.52})$$

with $\Theta(T)$ given by Eq.(II.27). The spectral functions in the vacuum are measured experimentally (see, e.g., Fig.9 in the vector channel). The above mixing formulas show that the pole positions of the correlation functions do not change at low T , while the pole residues are modified as $(f_\rho^t(T)/f_\rho)^2 = 1 - \Theta(T)$. Note also that these formulas satisfy the Weinberg sum rules. In fact, the T -dependence of $\langle \mathcal{O}_{4q} \rangle_T$ in the r.h.s. of Eq.(II.49) calculated by using the soft pion theorem coincides with that obtained from Eqs.(II.51,II.52) (Hatsuda *et al.*, 1993).

The density dependence of the four-quark condensate $\langle \mathcal{O}_{4q} \rangle_\rho$ is not known precisely. In the leading order of the virial expansion in terms of the baryon density, we have $\langle \mathcal{O} \rangle_\rho \simeq \langle \mathcal{O} \rangle_0 + \langle \mathcal{O} \rangle_N \rho$. The nucleon matrix element of $\mathcal{O} = \mathcal{O}_{4q}$ corresponds to higher twist terms in the deep inelastic lepton-nucleon scattering, but the value is still uncertain. A crude approximation originally made was a factorization ansatz (Hatsuda and Lee, 1992): $\langle \bar{q}_i q_j \bar{q}_k q_l \rangle_N \propto \langle \bar{q}q \rangle_0 \langle \bar{q}q \rangle_N$ with appropriate Fierz coefficients. It is not obvious, however, whether this estimate is accurate enough and further studies are necessary (Thomas *et al.*, 2007).

C. Dynamical approaches to in-medium hadrons

Although there are numerous attempts to relate hadronic spectral functions to $\langle \bar{q}q \rangle$ in the medium (Alam *et al.*, 2001; Cassing and Bratkovskaya, 1999; Mosel, 2008; Rapp and Wambach, 2000), no rigorous relations have been established yet except for the pion. In the following, we briefly outline various theoretical approaches that have been attempted so far.

1. Naive quark model

Assuming that the constituent quark mass M originates mainly from DBCS according to the idea of Nambu

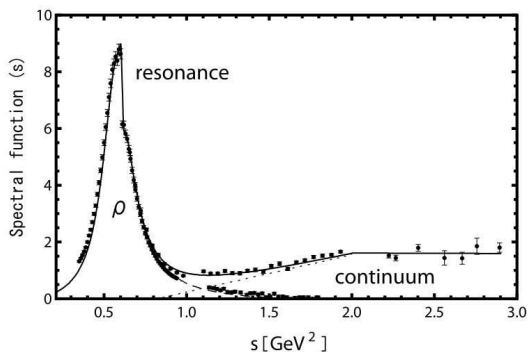


FIG. 9 Spectral function in the isovector channel in the vacuum ($\rho_V^{\text{vac}}(s)$ with $s = \omega^2$) obtained from the e^+e^- annihilation into even numbers of pions (Kwon *et al.*, 2008).

and Jona-Lasinio, and assuming further that the vector meson mass follows the additive rule $m_V \simeq 2M$, one may expect a reduction of m_V associated with the partial restoration of chiral symmetry. Such a shift could be detected through the decay of the neutral vector meson into dileptons (Pisarski, 1982).

2. Nambu–Jona-Lasinio model

As a field-theoretical model to treat the meson properties in the medium beyond the simple additive rule, the Nambu–Jona-Lasinio (NJL) model at finite temperature and density has been studied. In particular, the spectral degeneracy between π and σ in hot and/or dense matter was explicitly demonstrated (Hatsuda and Kunihiro, 1985, 1987a) (Bernard *et al.*, 1987). Further progress along these lines and a similar dynamical model based on the Dyson-Schwinger equation can be seen in (Buballa, 2005; Hatsuda and Kunihiro, 1994; Klevansky, 1992; Vogl and Weise, 1991) and in (Roberts and Schmidt, 2000), respectively.

3. QCD sum rules

The QCD sum rule (QSR) is a method which can relate the hadronic spectral functions to the QCD condensates through the operator product expansion and the dispersion relation (Shifman *et al.*, 1979a,b). This approach has been generalized to attack the problems of hadron properties in the hot/dense medium (Bochkarev and Shaposhnikov, 1986; Hatsuda *et al.*, 1993; Hatsuda and Lee, 1992), and further theoretical elaborations were made (Asakawa and Ko, 1993; Jin and Leinweber, 1995; Klingl *et al.*, 1997; Koike and Hayashigaki, 1997; Leupold *et al.*, 1998; Ruppert *et al.*, 2006). A major difference of the in-medium QSR from the in-vacuum QSR is that there arise Lorentz-tensor condensates. The weighted average of the spectral function $\langle \rho \rangle_W = \int d\omega \rho(\omega) W(\omega)$ obtained from the in-medium QSR gives useful QCD constraints

on various models (Eichstaedt *et al.*, 2007; Kwon *et al.*, 2008; Thomas *et al.*, 2005).

4. Hadron mass scaling

It was conjectured that the masses of light vector mesons (ρ, ω) scale universally as a function of density and/or temperature (Brown and Rho, 1991). Near the chiral restoration point, $\langle \bar{q}q \rangle / \langle \bar{q}q \rangle_0 \ll 1$, the scaling law reads

$$\frac{m_\rho^*}{m_\rho} \simeq \frac{m_\omega^*}{m_\omega} \simeq \frac{\langle \bar{q}q \rangle}{\langle \bar{q}q \rangle_0}, \quad (\text{II.53})$$

where m^* denote the pole mass of in-medium vector mesons (Brown *et al.*, 2008). The theoretical foundation of such a scaling law may be obtained by an approach in which the vector mesons are considered to be the gauge bosons associated with the hidden local symmetry of the chiral effective Lagrangian (Harada *et al.*, 2002; Harada and Sasaki, 2002, 2006; Harada and Yamawaki, 2003; Hidaka *et al.*, 2006).

5. Bag model

The bag model is a phenomenological approach in which quarks and gluons are confined in a “bag” inside non-perturbative QCD vacuum. In the nuclear medium, the non-vanishing expectation values of the scalar-isoscalar meson $\langle \sigma \rangle$ and the time-component of the vector-isoscalar meson $\langle \omega_0 \rangle$ develop, so that they act as effective scalar and vector potentials on the quarks inside the bag. In such a quark-meson coupling model, in-medium baryons composed of three valence quarks feel both scalar and vector potentials with opposite sign, while the in-medium mesons composed of quark and anti-quark feel only the scalar potential and obey a universal scaling law dictated by the density dependence of $\langle \sigma \rangle$ (Saito and Thomas, 1995; Saito *et al.*, 1997b, 2007).

6. Hadronic models

There are purely hadronic descriptions of the in-medium vector mesons. In the Walecka type models, the one-loop self-energy of vector mesons in nuclear matter receives contributions from the low-energy particle-hole (p - h) excitations and the high energy nucleon–anti-nucleon (N - \bar{N}) excitations. The former gives the standard plasmon effect which increases the pole mass of the vector meson, while the latter tends to decrease the pole mass: These effects are simply understood from the quantum mechanical level repulsion. The net effect with a standard parameter set of the Walecka model shows that the N - \bar{N} effect wins and the pole mass decreases (Caillon and Labarsouque, 1993; Jean *et al.*, 1994; Kurasawa and Suzuki, 1990; Saito *et al.*, 1989;

Shiomi and Hatsuda, 1994). For more details of such a model, see the review (Hatsuda *et al.*, 1996). The actual vector meson in nuclear matter receives not only the nucleon effect but also effects from resonances such as Δ and N^* . They modify the spectral structure non-trivially and cause spectral shift, spectral broadening, and even new peaks (Asakawa *et al.*, 1992; Chanfray and Schuck, 1993; Friman and Pirner, 1997; Herrmann *et al.*, 1993; Post *et al.*, 2004; Rapp *et al.*, 1997; Rapp and Wambach, 2000).

7. Chiral effective theories

Spectral change of the broad resonance σ in the hot and/or dense medium is one of the interesting signals of chiral symmetry restoration (Hatsuda and Kunihiro, 1985, 1987a). An example is the enhancement of the spectral function in the scalar-isoscalar channel near the 2π threshold at finite T (Chiku and Hatsuda, 1998a,b; Volkov *et al.*, 1998) and at finite baryon density (Aouissat *et al.*, 1995; Hatsuda *et al.*, 1999; Schuck *et al.*, 1988). Since σ and ρ are both resonances in the π - π system, it is necessary to take into account multiple scattering of the pions inside the medium to study their spectral structures. For this purpose, unitarization of the in-medium π - π scattering amplitude of the chiral Lagrangian on the basis of the N/D method and the inverse amplitude method has been extensively explored (Cabrera *et al.*, 2008, 2005; Fernandez-Fraile *et al.*, 2007; Jido *et al.*, 2001; Oller *et al.*, 2000; Yokokawa *et al.*, 2002). The large N expansion of the $O(N)$ symmetric scalar model has also been studied as a toy model (Hidaka *et al.*, 2004; Patkos *et al.*, 2002).

8. Lattice QCD

The best quantitative method to study the medium modification of hadrons should be the lattice QCD simulations. The maximum entropy method (MEM), which allows us to extract the in-medium spectral functions from the Euclidean correlation functions measured on the lattice has been proposed and tested in the quenched lattice QCD simulations at finite temperature (Asakawa *et al.*, 2001, 2003; Karsch and Laermann, 2003). Its application to the lattice data with dynamical quarks has been started at finite T although it is still limited to heavy quarkoniums at the moment (Aarts *et al.*, 2007). The application of this method to QCD at finite density is still not attainable due to the sign problem which invalidates the importance sampling in Monte Carlo simulations (Muroya *et al.*, 2003). In the mean time, it would be useful to study in-medium hadronic properties by analytic lattice approaches such as the strong coupling expansion at finite T and μ (Ohmishi *et al.*, 2008).

III. PSEUDOSCALAR MESON: π IN NUCLEI

A. Theoretical background

As we have shown in the introduction, a sizable reduction of the chiral condensate in nuclear matter of about 30% is theoretically expected. A possible way to detect this reduction is to study the in-medium pion properties through precision spectroscopy of deeply bound pionic atoms and through precision measurements of the low-energy pion-nucleus scattering.

The basic tool to relate the in-medium chiral condensate and the experimental data is the pion-nucleus optical potential $U_{\text{opt}}(\mathbf{r})$. The starting point is the pion propagator in asymmetric nuclear matter,

$$[D_\pi(\omega, \mathbf{q})]^{-1} = \omega^2 - \mathbf{q}^2 - m_\pi^2 - \Pi(\omega, \mathbf{q}). \quad (\text{III.54})$$

Here Π denotes the in-medium pion self-energy which is written in the linear density approximation as

$$\Pi(\omega, \mathbf{q}) = -\mathcal{T}^+ \rho - \epsilon \mathcal{T}^- \delta\rho, \quad (\text{III.55})$$

where $\rho = \rho_p + \rho_n$ (total baryon density), $\delta\rho = \rho_p - \rho_n$ (total isospin density), and $\epsilon = +1, 0, -1$ for π^-, π^0, π^+ . The off-shell isoscalar (isovector) forward scattering amplitude $\mathcal{T}^{+(-)}$ for small ω and at $\mathbf{q} = 0$ reads (Ericson and Weise, 1988)

$$\mathcal{T}^+(\omega) = \frac{\sigma_{\pi N} - \beta\omega^2}{f_\pi^2}, \quad \mathcal{T}^-(\omega) = \frac{\omega}{2f_\pi^2}. \quad (\text{III.56})$$

From the constraints $\mathcal{T}^+(\omega = m_\pi, \mathbf{0}) = 4\pi(1 + m_\pi/M)a_{\pi N}$ with the accidentally small isoscalar scattering length $a_{\pi N} = (0.0016 \pm 0.0013)m_\pi^{-1}$ (Schröder *et al.*, 2001), we have $\beta \simeq \sigma_{\pi N}/m_\pi^2$. This approximation is valid in 5% accuracy to β . The π^0 does not have a mass shift in the nuclear medium in the same approximation.

One may introduce the energy independent optical potential as $\omega^2 = m_\pi^2 + 2m_\pi U_{\text{opt}}$ which is a solution of the dispersion relation $\omega^2 - m_\pi^2 - \Pi(\omega) = 0$. As long as $U_{\text{opt}} \ll m_\pi$ and the linear density approximation is valid, one finds

$$U_{\text{opt}} \simeq \epsilon \frac{\delta\rho}{4[f_\pi^t(\rho)]^2}. \quad (\text{III.57})$$

This implies that there is an extra repulsion (attraction) for π^- (π^+) from the medium associated with the reduction of the pion decay constant (Weise, 2000, 2001a).

In the local density approximation, $\rho_{p,n} \rightarrow \rho_{p,n}(\mathbf{r})$, the Klein-Gordon equation corresponding to Eq.(III.54) reads $[\bar{\omega}^2 + \nabla^2 - m_\pi^2 - \Pi(\bar{\omega}, \nabla; \rho_{p,n}(\mathbf{r}))] \Phi(\mathbf{r}) = 0$, or equivalently near the mass shell,

$$[\bar{\omega}^2 + \nabla^2 - m_\pi^2 - 2m_\pi U_{\text{opt}}(\rho_{p,n}(\mathbf{r}))] \Phi(\mathbf{r}) = 0, \quad (\text{III.58})$$

with $\bar{\omega} = \omega - V_{\text{Coul}}(\mathbf{r})$ where V_{Coul} is the Coulomb potential between π^\pm and the nucleus. There are several important contributions to U_{opt} other than Eq.(III.57)

in studying the experimental data of the deeply bound pionic atoms and the low energy π -nucleus scattering: (i) higher order terms in ω and m_π to the s -wave part of \mathcal{T}^+ and \mathcal{T}^- (Döring and Oset, 2008; Kolomeitsev *et al.*, 2003a,b), (ii) the two-nucleon absorption of the pion, and (iii) the p -wave contribution with spatial derivatives (Ericson and Weise, 1988; Friedman and Gal, 2007). Their explicit forms are given in the next section.

B. Pion-nucleus optical potential

1. s -wave and p -wave parts

The pion-nucleus potential (Ericson and Ericson, 1966) is composed of the s -wave and p -wave parts:

$$U_{\text{opt}}(r) = U_s(r) + U_p(r), \quad (\text{III.59})$$

$$U_s(r) = -\frac{2\pi}{m_\pi} [b(r) + \varepsilon_2 B_0 \rho^2(r)], \quad (\text{III.60})$$

$$U_p(r) = \frac{2\pi}{m_\pi} \vec{\nabla} \cdot [c(r) + \varepsilon_2^{-1} C_0 \rho^2(r)] L(r) \vec{\nabla}, \quad (\text{III.61})$$

with

$$b(r) = \varepsilon_1 \{b_0 \rho(r) + b_1 [\rho_n(r) - \rho_p(r)]\}, \quad (\text{III.62})$$

$$c(r) = \varepsilon_1^{-1} \{c_0 \rho(r) + c_1 [\rho_n(r) - \rho_p(r)]\}, \quad (\text{III.63})$$

$$L(r) = \frac{1}{1 + \frac{4}{3}\pi\lambda [c(r) + \varepsilon_2^{-1} C_0 \rho^2(r)]}, \quad (\text{III.64})$$

where λ is the Lorentz-Lorenz-Ericson-Ericson correction parameter. The kinematical factors ε_1 and ε_2 are defined as $\varepsilon_1 = 1 + m_\pi/m_N$ and $\varepsilon_2 = 1 + m_\pi/2m_N$ with the nucleon mass m_N . The complex parameters B_0 and C_0 are the s -wave and p -wave absorption parameters, respectively.

From the pionic-atom x-ray data, the p -wave parameters have been fairly precisely determined, while the x-ray data are less sensitive to the s -wave parameters. This situation can be understood from Fig. 10, which shows that the $1s$ strong-interaction shift is dominated by the s -wave potential while the $3d$ (and higher) level shifts are dominated by the p -wave potential. It is therefore important to obtain experimental information on the $1s$ level in order to precisely determine the s -wave parameters.

2. Pionic hydrogen - the πN scattering lengths at threshold

In the low-density limit, the potential is described by just two parameters, b_0 and b_1 in Eq.(III.62), which are nothing but isoscalar and isovector πN scattering lengths, respectively¹. These have been very precisely

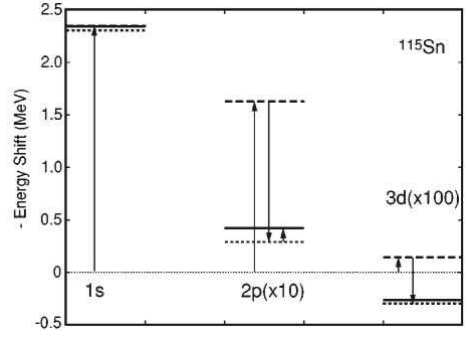


FIG. 10 The binding energies with finite-size Coulomb potential only, B_{Coul} , and Coulomb plus optical potential, B_{full} , are calculated. The energy shifts $B_{\text{Coul}} - B_{\text{full}}$ are shown as the solid bars for pionic $1s$, $2p$, and $3d$ states for ^{115}Sn . The shifts due to the real local terms in the potential are shown by dashed bars. Dotted bars are the results with all real terms (local plus nonlocal) in the optical potential (Umemoto *et al.*, 2000).

determined by the pionic hydrogen x-ray spectroscopy at the Paul Scherrer Institut (PSI) (Gotta *et al.*, 2008; Schröder *et al.*, 2001).

The πN scattering lengths can be determined from the observed strong-interaction shift ϵ_{1s} and width Γ_{1s} of pionic hydrogen:

$$\frac{\epsilon_{1s}}{B_{1s}} = -\frac{4}{r_B} a_{\pi^- p \rightarrow \pi^- p} (1 + \delta_\epsilon) \propto b_0 - b_1, \quad (\text{III.65})$$

$$\frac{\Gamma_{1s}}{B_{1s}} = 8 \frac{q_0}{r_B} \left(1 + \frac{1}{P}\right) [a_{\pi^- p \rightarrow \pi^0 n} (1 + \delta_\Gamma)]^2 \propto (b_1)^2, \quad (\text{III.66})$$

where $B_{1s} = 3.24$ keV and $r_B = 216$ fm respectively are the $1s$ binding energy and the ‘Bohr radius’ of pionic hydrogen, $q_0 = 0.1421$ fm $^{-1}$ the center-of-mass momentum of the π^0 in the charge-exchange reaction $\pi^- p \rightarrow \pi^0 n$ and $P = 1.546 \pm 0.009$ the branching ratio of charge exchange and radiative capture (Panofsky ratio). The quantities $\delta_{\epsilon, \Gamma}$ represent the corrections to be applied to the experimentally determined scattering length in order to obtain pure strong-interaction quantities.

The PSI experiment R-98.01 (Fig. 11) used a superconducting cyclotron trap to produce a high stop density for pions in a hydrogen gas target, a Johann-type bent-crystal spectrometer, and a two-dimensional CCD focal-plane detector to determine the pionic-hydrogen x-rays. The $1s$ strong-interaction shift was determined from the $3p - 1s$ energy to be $\epsilon_{1s}^{\pi H} = 7120 \pm 11$ meV. The $1s$

¹ Ericson and Ericson (1966) defines $b_0 \equiv (a_{1/2} + 2a_{3/2})/3$, $b_1 \equiv (a_{3/2} - a_{1/2})/3$, while isoscalar a^+ and isovector a^- scattering

lengths are $a^+ \equiv (a_{1/2} + 2a_{3/2})/3$, $a^- \equiv (a_{1/2} - a_{3/2})/3$ in pionic hydrogen literatures (e.g., (Gotta *et al.*, 2008)). Here, $a_{1/2}$ and $a_{3/2}$ respectively are the isospin 1/2 and 3/2 scattering lengths. Note therefore $b_0 = a^+$ and $b_1 = -a^-$.

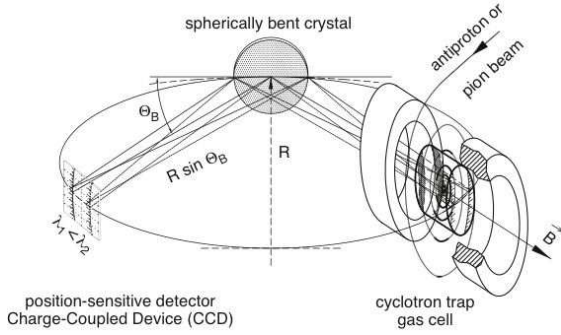


FIG. 11 A schematic drawing of the PSI pionic hydrogen setup (Gotta *et al.*, 2008).

hadronic broadening was deduced from the widths of $4p - 1s$, $3p - 1s$ and $2p - 1s$ transitions, so as to correct for the kinematical broadening caused by the preceding transitions width, to be $\Gamma_{1s}^{\pi H} = 823 \pm 18$ meV. With the corrections δ_ϵ and δ_Γ obtained within chiral perturbation theory (Gasser *et al.*, 2002; Zemp, 2003), the scattering lengths have been obtained to be (Gotta *et al.*, 2008)

$$b_0 = 0.0069 \pm 0.0031 m_\pi^{-1}, \quad (\text{III.67})$$

$$b_1 = -0.0864 \pm 0.0012 m_\pi^{-1}. \quad (\text{III.68})$$

These values are near the leading-order result derived from current algebra (called Tomozawa-Weinberg (TW) values) (Tomozawa, 1966; Weinberg, 1966) of

$$b_0^{TW} = 0, \quad (\text{III.69})$$

$$b_1^{TW} = -\frac{1}{4\pi\epsilon_1} \frac{m_\pi}{2f_\pi^2} = -0.079 m_\pi^{-1}, \quad (\text{III.70})$$

with $\epsilon_1 = 1 + m_\pi/m_N = 1.149$, $m_\pi = 139.57$ MeV and $f_\pi = 92.4$ MeV, revealing an important feature of the underlying chiral symmetry. The $\sim 10\%$ gap between the experimental value of b_1 and b_1^{TW} gets closed by pion-loop corrections of order m_π^3 (Bernard *et al.*, 1993, 1995).

3. The missing repulsion problem

It has long been known that the available pionic-atom x-ray data cannot be fitted with b_0 and b_1 values, but some enhancement of the s -wave repulsive strength is required. This is known as the ‘missing repulsion’ problem.

The situation is illustrated in Fig. 12, in which the s -wave parameters b_0 and $\text{Re}B_0$ obtained by various authors are plotted. We note, firstly, that there is a strong correlation between b_0 and $\text{Re}B_0$, approximated by $b_0 + 0.215 \text{Re}B_0 = -0.028$ (known as the Seki-Masutani relation (Seki and Masutani, 1983))². Secondly, the Seki-

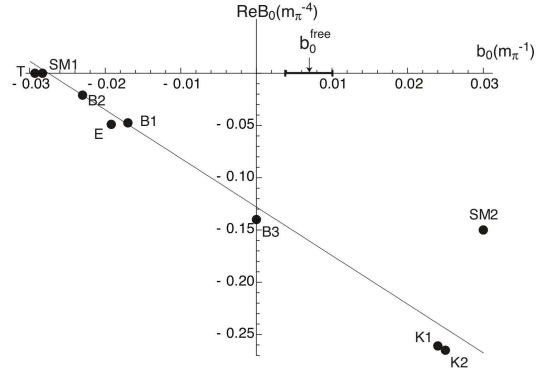


FIG. 12 The s -wave parameters b_0 vs $\text{Re}B_0$ obtained by fitting the x-ray data; T: (Tauscher, 1971), B1-3: (Batty *et al.*, 1979, 1983, 1997), SM1-2: (Seki and Masutani, 1983), K1-2: (Konijn *et al.*, 1990), E: (Ericson and Tauscher, 1982). The line is $b_0 + 0.215 \text{Re}B_0 = -0.028$.

Masutani relation implies that the $\text{Re}B_0$ value must be around -0.15 if we are to take the ‘free’ b_0 value, which is much larger in magnitude than expected from the pion deuteron scattering length (Chatellard *et al.*, 1997). If on the other hand $\text{Re}B_0$ is forced to be small ($\simeq 0$), the fitted b_0 is about -0.03 , quite far away from the ‘free’ value.

Part of the repulsion is known to be provided by the ‘double scattering’ correction to b_0 (Ericson and Ericson, 1966; Loiseau *et al.*, 2001),

$$b_0 \rightarrow \bar{b}_0 = b_0 - [b_0^2 + 2b_1^2] \left\langle \frac{1}{r} \right\rangle, \quad (\text{III.71})$$

where the inverse correlation length is expressed by the Fermi momentum k_F as

$$\left\langle \frac{1}{r} \right\rangle = \frac{3}{2\pi} k_F(\rho) = \frac{3}{2\pi} \left[\frac{3\pi^2}{2} \rho(r) \right]^{1/3}, \quad (\text{III.72})$$

but this correction is still insufficient to account for the missing repulsion. The experiment S236 at GSI, discussed in the next section, established that the in-medium value of b_1 is enhanced relative to b_1 , which, through Eq.(III.71), provides the extra s -wave repulsion.

C. Deeply-bound pionic atom spectroscopy

In 1996, the experiment S160 at GSI reported the first observation of the *deeply bound pionic states* in ^{207}Pb (Yamazaki *et al.*, 1996), whose existence and formation had been predicted previously (Friedman and Soff, 1985; Hirenzaki *et al.*, 1991; Toki *et al.*, 1991a, 1989; Toki and Yamazaki, 1988). This discovery opened an entirely new way to study the hadron properties in the nuclear medium. As illustrated in Fig. 13, the $1s$ wavefunction of π^- bound to a heavy nucleus overlaps appreciably with the nuclear density distribution, and hence the in-medium modification of the pion properties may have detectable effects on the binding energy and/or width.

² This linear relation arises since the mean density probed by the π^- happens to be about $0.5 - 0.6\rho_0$ regardless of element, so that $b_0\rho + \text{Re}B_0\rho^2$ can be linearized as $b_0\rho + (\text{Re}B_0\rho_0/2)\rho$ (Yamazaki and Hirenzaki, 2003).

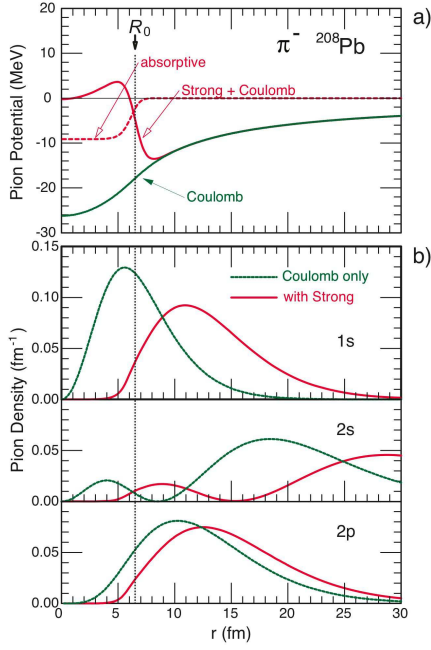


FIG. 13 a) The pion optical potential for ^{208}Pb . The finite-size Coulomb potential is expressed by the dotted curve and the one with the optical potential by the solid curve. The imaginary part is depicted by the dashed curve. b) The pionic wavefunctions of the $1s$, $2s$ and $2p$ states in coordinate space. The dashed curves and the solid curves are obtained with the finite-size Coulomb potential and with the optical potential. The half-density radius R_0 of ^{208}Pb is indicated by the broken line (Toki *et al.*, 1991b).

Although this was not clearly recognized when the deeply-bound pionic-atom spectroscopy was initially conceived (Toki and Yamazaki, 1988), it was later established that the in-medium value of the isovector πN scattering length b_1 , derived from the $1s$ binding energies, is connected to the (temporal part of the) in-medium pion decay constant f_π^t via the in-medium Tomozawa-Weinberg relation (Tomozawa, 1966; Weinberg, 1966), (Kolomeitsev *et al.*, 2003b),

$$b_1(\rho) = -\frac{4\pi}{1 + m_\pi/m_N} \frac{m_\pi}{2 [f_\pi^t(\rho)]^2} \quad (\text{III.73})$$

which is in turn connected to the in-medium chiral condensate via the in-medium Gell-Mann–Oakes–Renner (GOR) relation Eqs. (II.41) and (II.42), or via the Glashow-Weinberg (GW) relation Eq.(II.43).

In the case of deeply-bound pionic atoms, the π^- quantum number is well defined. Moreover, as will be shown, the use of recoilless ($d, {}^3\text{He}$) kinematics ensures that the nucleus is in the ground state. The pion wavefunction and its overlap with the nuclear density are therefore precisely calculable by solving the Klein-Gordon equation. This makes it possible to compare the experimental results with theoretical predictions, and to quantitatively deduce the effects of partial restoration of chiral symmetry.

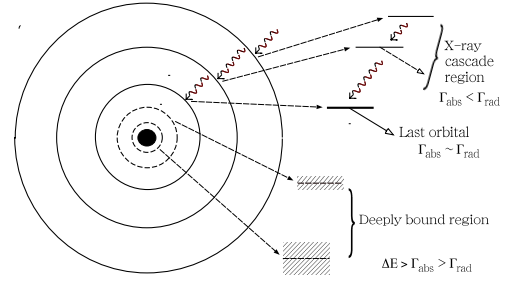


FIG. 14 A schematic figure of pionic atom states with x-ray transitions down to the last orbital and deeply bound inner orbits with large widths which cannot be populated following the x-ray cascade. They have large widths due to nuclear absorption but are still discrete states with $\Gamma_n < E_n - E_{n-1}$. (Yamazaki *et al.*, 2008).

A wealth of data on pionic atoms has been collected by means of pionic x-ray spectroscopy (Batty *et al.*, 1997). In the x-ray spectroscopy experiments (e.g., de Laat *et al.* (1991)), pions, injected into a target, slow down and form pionic atoms, and x-rays emitted in the cascade are measured, as schematically depicted in Fig. 14. While high-lying states do not show detectable strong-interaction effects, the energy levels of low-lying states get shifted from those calculated by using the electromagnetic interaction. The level widths also become larger due to pion absorption on the nucleus. From the measured strong-interaction shifts (ϵ) and widths (Γ), the pion-nucleus strong-interaction potential parameters can be deduced.

The measured pion-nucleus strong-interaction shifts are shown in Fig. 15 as function of atomic number Z . This plot shows that the information on the $1s$ level shift is available only up to the atomic number of $Z = 14$. This is because beyond the *last orbital* (Fig. 14) x-rays cannot be observed due to the increase of the pion-nucleus absorption width. As shown in Fig. 15, $3d$ is the last orbital for medium-to-heavy nuclei, meaning that it is not possible to obtain the information on $1s$ and $2p$ levels by means of x-ray spectroscopy. The $1s$ and $2p$ levels which cannot be populated by x-ray cascade are often referred to as the *deeply-bound pionic states*.

1. Structure of deeply-bound pionic atoms

This, however, does not mean that those states do not exist, as was recognized by Friedman and Soff (1985) and by Toki and Yamazaki (1988). In Fig. 16, a typical pion-nucleus optical potential set (see section III.B) was used to calculate the binding energies and widths of pionic Zr (left) and Pb (right) atoms. The $1s$ level width Γ_{1s} is found to be much smaller than the $2p - 1s$ level interval ($\Delta E_{2p-1s} < \Gamma_{1s}$) even for heavy pionic atoms such as pionic ^{208}Pb . Namely, the deeply-bound pionic atoms are metastable, despite the strong pion-nucleus absorption.

This somewhat counter-intuitive result arises due to

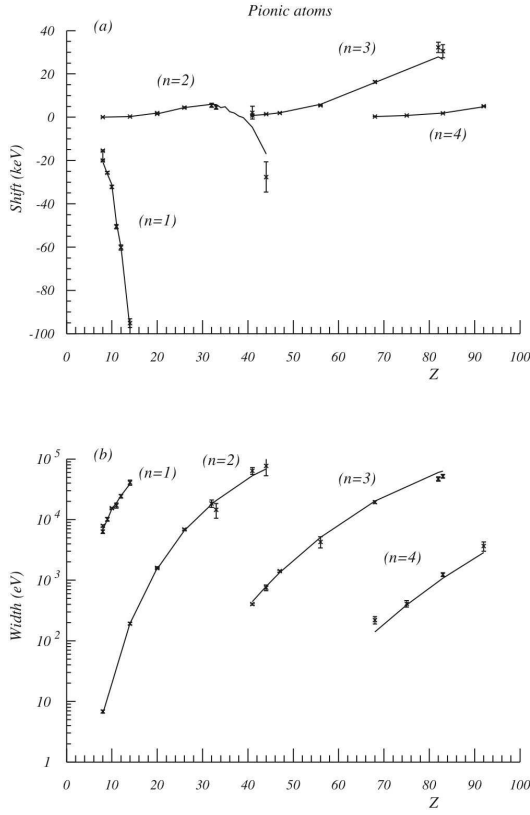


FIG. 15 Strong-interaction shift (top) and width (bottom) of pionic atoms. The continuous lines join points calculated with the best-fit optical potential (Batty *et al.*, 1997).

the repulsive nature of the pion-nucleus s -wave interaction, which causes the $1s$ binding energies to decrease (Fig. 16) and also pushes the wavefunction outwards (see the difference between the solid and dashed curves in Fig. 13(b)). This then reduces the pion-nucleus overlap, making the level width narrower.

2. Formation of deeply-bound pionic atoms

The original deeply-bound pionic atom formation scheme proposed by Toki and Yamazaki (1988) was to use the $^{208}\text{Pb}(n, p)$ reaction. This was tested at TRIUMF (Iwasaki *et al.*, 1991), but no bound-state peak was observed. It was soon recognized that (n, d) or $(d, ^3\text{He})$ reactions (see Fig. 17) are more suitable (Hirenzaki *et al.*, 1991). These are *recoilless* as well as *substitutional* reactions, in which a neutron in the s shell is picked up and the produced π^- is left in the $1s$ orbit with a small momentum transfer (Fig. 18). Due to the substitutional nature of the reaction, the angular momentum transfer is $\Delta L = 0$. The small momentum transfer makes it possible to satisfy the angular momentum matching in surface reactions, thereby minimizing the nuclear distortion.

Using the $(d, ^3\text{He})$ reaction, the experiment S160 at GSI succeeded to observe the $2p$ and $1s$ states of pionic

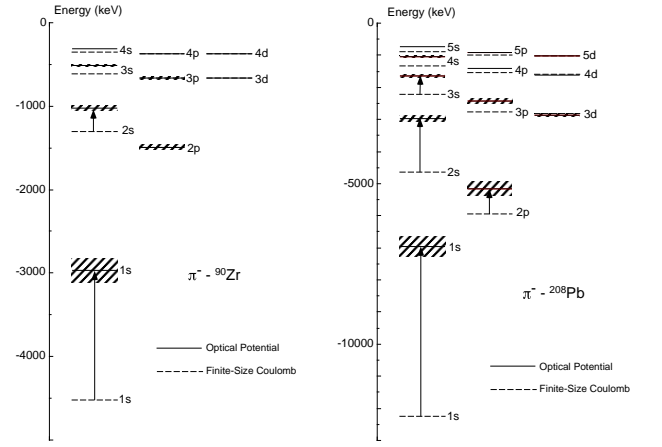


FIG. 16 Energy levels of pionic atoms of ^{90}Zr and ^{208}Pb . The results with the finite-size Coulomb potential (i.e., taking account of the nuclear charge distribution) are shown by dashed lines, while those with the optical potential by solid lines with hatched area indicating the level widths (Toki and Yamazaki, 1988).

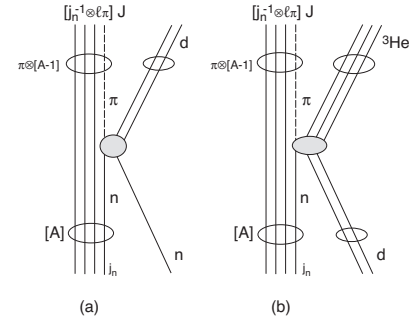


FIG. 17 Diagrams for proton-pick-up pion-transfer (a) (n, d) and (b) $(d, ^3\text{He})$ reactions to form pionic bound states on a neutron-hole state (Hirenzaki *et al.*, 1991).

^{207}Pb (Yamazaki *et al.*, 1996). As shown in Fig. 19, the experimental result agrees remarkably well with the theoretical prediction. This firmly established the methodology of deeply-bound pionic atom spectroscopy.

3. GSI S236 - $\text{Sn}(d, ^3\text{He})$

In principle, the s -wave parameters may be obtained by analyzing the $1s$ -level energies and widths of light pionic atom x-rays ($Z \leq 14$, Fig. 15). However, since the available data are on $N = Z$ nuclei, the sensitivity of the dataset to the isovector parameter b_1 is quite limited.

The S236 experiment at GSI, a successor to S160, measured the $1s$ binding energies and widths of pionic $^{115,119,123}\text{Sn}$ using the $^{116,120,124}\text{Sn}(d, ^3\text{He})$ reactions. Sn isotopes were chosen since the $1s$ states are expected to be produced as the most dominant quasi-substitutional states, $(1s)_{\pi^-} - (3s)_n^{-1}$, because of the presence of the $3s$ orbital near the Fermi surface (Fig. 20). Another merit

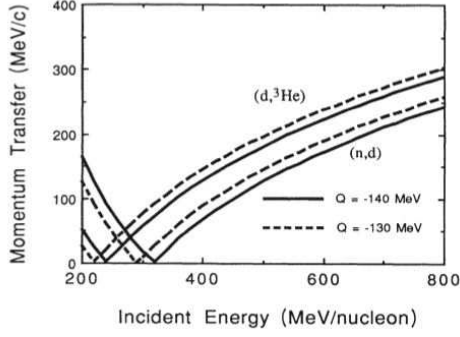


FIG. 18 Momentum transfers in the (n,d) and ($d,^3\text{He}$) reactions on Pb for $Q = -130$ and -140 MeV as a functions of the incident energy per nucleon (Hirenzaki *et al.*, 1991).

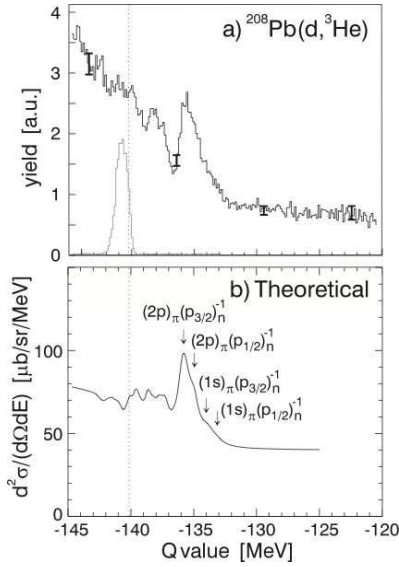


FIG. 19 (a) The $^{208}\text{Pb}(d,^3\text{He})$ spectrum. The abscissa is the reaction Q value. and the π^- emission threshold ($Q = -140.14\text{MeV}$) is shown by a dotted line. The $p(d,^3\text{He})\pi^0$ reaction peak used as a calibration is also shown in the Q value scale of the $^{208}\text{Pb}(d,^3\text{He})$ reaction kinematics. (b) Theoretical prediction by Hirenzaki *et al.* (1991). A FWHM resolution of 0.5 MeV is assumed (Yamazaki *et al.*, 1996).

is to make use of isotopes over a wide range of $(N - Z)/A$ to sensitively deduce the isovector parameter b_1 .

The experiment S236 used a deuteron beam from the heavy-ion synchrotron SIS at GSI, Darmstadt, combined with the fragment separator (FRS) as a high-resolution forward spectrometer (Fig. 21). They chose the exact recoilless condition to suppress minor states other than the enhanced $1s$ states with quasi-substitutional $1s$ states, with a deuteron beam of a small momentum spread and an accurately measured energy of 503.388 ± 0.100 MeV. The Q -value resolution was 394 ± 33 keV (FWHM), and the absolute Q -value scale was calibrated to an accuracy of ± 7 keV using the $p(d,^3\text{He})\pi^0$ reaction, where a thin Mylar layer put on the surface of each Sn target was used

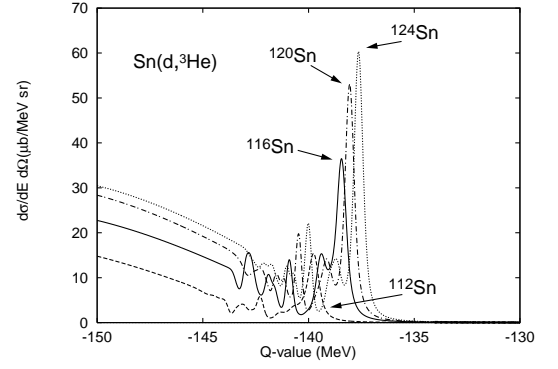


FIG. 20 The Sn isotope dependence of the total ($d,^3\text{He}$) spectrum for the pionic atom formation at $T_d = 500$ MeV with 300 keV experimental resolution. The target nucleus is indicated in the figure. (Umemoto *et al.*, 2000).

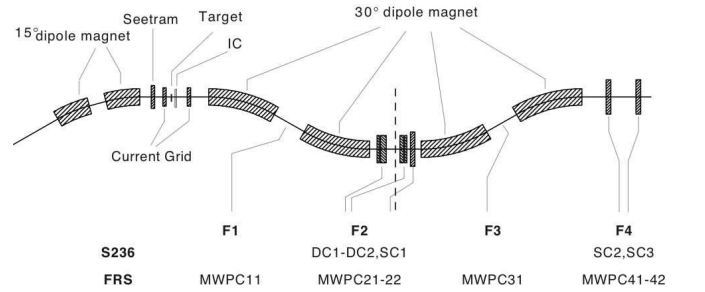


FIG. 21 The Fragment Separator of GSI used for the ($d,^3\text{He}$) spectroscopy.

as the proton source.

The observed spectra, $d^2\sigma/dE/d\Omega$, on Mylar-covered ^{116}Sn , ^{120}Sn , ^{124}Sn targets as a function of the ^3He kinetic energy, are shown in Fig. 22. In each spectrum of Fig. 22 a distinct peak at around 365 MeV was observed, which was assigned to a dominant configuration of $(1s)_\pi(3s)_n^{-1}$. The skewed peaks at around 371 MeV arise from $p(d,^3\text{He})\pi^0$. The overall spectrum shapes for the three Sn targets were found to be in good agreement with the predicted ones (Fig. 20). The spectra were decomposed according to the theoretical prescription of Umemoto *et al.* (2000), from which the $1s$ binding energies (B_{1s}) and widths (Γ_{1s}) were determined as:

$$\begin{aligned}
 ^{115}\text{Sn} : B_{1s} &= 3.906 \pm 0.021 \text{ (stat)} \pm 0.012 \text{ (syst)} \text{ MeV}, \\
 \Gamma_{1s} &= 0.441 \pm 0.068 \text{ (stat)} \pm 0.054 \text{ (syst)} \text{ MeV}, \\
 ^{119}\text{Sn} : B_{1s} &= 3.820 \pm 0.013 \text{ (stat)} \pm 0.012 \text{ (syst)} \text{ MeV}, \\
 \Gamma_{1s} &= 0.326 \pm 0.047 \text{ (stat)} \pm 0.065 \text{ (syst)} \text{ MeV}, \\
 ^{123}\text{Sn} : B_{1s} &= 3.744 \pm 0.013 \text{ (stat)} \pm 0.012 \text{ (syst)} \text{ MeV}, \\
 \Gamma_{1s} &= 0.341 \pm 0.036 \text{ (stat)} \pm 0.063 \text{ (syst)} \text{ MeV}.
 \end{aligned}$$

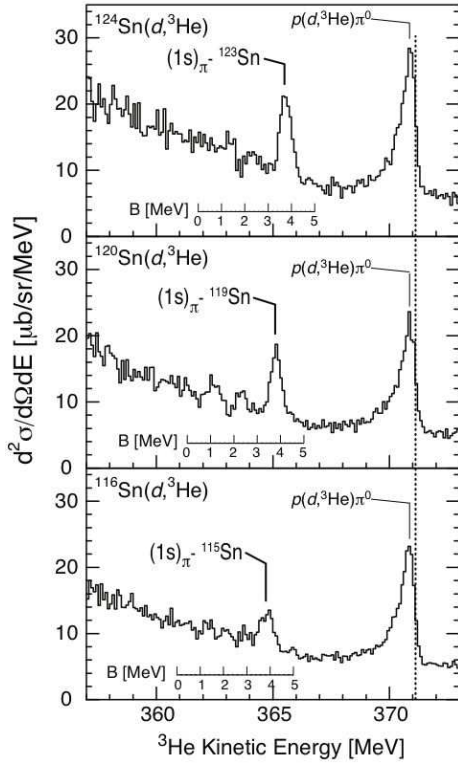


FIG. 22 Double differential cross sections versus the ${}^3\text{He}$ kinetic energy of the ${}^{124,120,116}\text{Sn}(d,{}^3\text{He})$ reactions measured at the incident deuteron energy of 503.388 MeV. The scales of the π^- binding energies in ${}^{123,119,115}\text{Sn}$ are also indicated. From Suzuki *et al.* (2004).

In-medium isovector scattering length b_1

The s -wave potential parameters $\{b_0, b_1, \text{Re}B_0, \text{Im}B_0\}$ were deduced by simultaneously fitting B_{1s} and Γ_{1s} of the three Sn isotopes together with those of symmetric light nuclei (${}^{16}\text{O}$, ${}^{20}\text{Ne}$ and ${}^{28}\text{Si}$), with the p -wave parameters fixed to the known values from pionic x-ray data listed in Batty *et al.* (1997).

The obtained values are:

$$\begin{aligned} b_0 &= -0.0233 \pm 0.0038 m_\pi^{-1}, \\ b_1 &= -0.1149 \pm 0.0074 m_\pi^{-1}, \\ \text{Re}B_0 &= -0.019 \pm 0.017 m_\pi^{-4}, \\ \text{Im}B_0 &= 0.0472 \pm 0.0013 m_\pi^{-4}. \end{aligned}$$

The effective density probed by the π^- was $\rho \simeq 0.6\rho_0$ (obtained from the overlap of the nuclear density and the pion wavefunction, such as shown in Fig. 13 (Yamazaki and Hirenzaki, 2003)). Figure 25 shows the likelihood contours in the plane of $\{b_1, \text{Im}B_0\}$. As shown, the best-fit b_1 value deviates significantly from the ‘free’ value obtained from pionic hydrogen.

Also shown therein is how the best-fit values move if the shape of the neutron distribution was changed. In fact, the most serious problem in the analysis was the

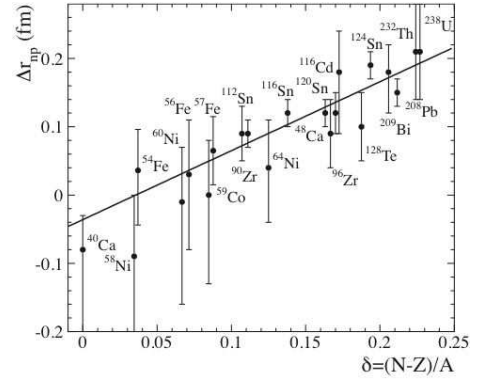


FIG. 23 Difference Δr_{np} between the rms radii of the neutron and proton distributions as deduced from the antiprotonic atom x-ray data, as a function of $\delta = (N - Z)/A$. The proton distributions were obtained from electron scattering data (De Vries *et al.*, 1987) (Sn nuclei) or from muonic atom data (Fricke *et al.*, 1995) (other nuclei). The full line represents the linear relationship between δ and Δr_{np} as obtained from a fit to the experimental data. From Trzcińska *et al.* (2001).

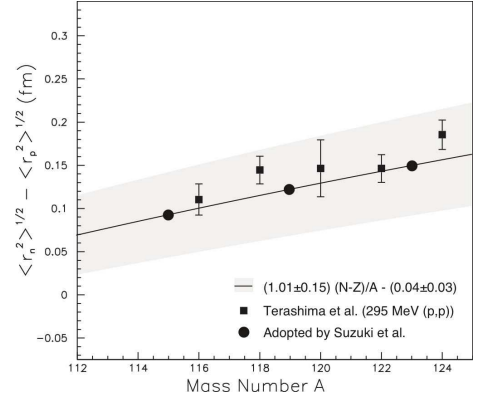


FIG. 24 Difference Δr_{np} between the rms radii of the neutron and proton distributions for various tin isotopes deduced from proton elastic scattering at 295 MeV (Terashima *et al.*, 2008) (squares) compared with the values adopted in the analysis of Suzuki *et al.* (2004) (filled circles), which used the relation $\Delta r_{np} = (1.01 \pm 0.15)(N - Z)/A + (-0.04 \pm 0.03)$ obtained by Trzcińska *et al.* (2001).

relatively poor knowledge concerning the neutron distribution $\rho_n(r)$ in Sn isotopes, whereas the proton distribution $\rho_p(r)$ is well known (Fricke *et al.*, 1995). In the fit, the neutron diffuseness (a_n) and half-density radius (c_n) parameters in the two-parameter Fermi distribution were chosen so as to satisfy the difference between the neutron and proton rms radii, $\Delta r_{np} = (1.01 \pm 0.15)(N - Z)/A + (-0.04 \pm 0.03)$ fm (Fig. 23), based on experimental data of antiprotonic atoms of Sn isotopes (Trzcińska *et al.*, 2001) as well as of many other nuclei. The two extreme assumptions, the ‘‘skin’’ type ($c_p < c_n, a_p = a_n$) and the ‘‘halo’’ type ($c_p = c_n, a_p < a_n$), where c_p (c_n) is the proton (neutron) half-density radius and a_p (a_n) is the proton (neutron) diffuseness of the two-parameter Fermi distri-

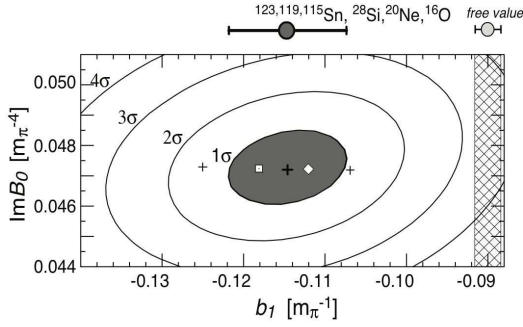


FIG. 25 Likelihood contours in the $\{b_1, \text{Im}B_0\}$ plane from the simultaneous fitting of $\{B_{1s}, \Gamma_{1s}\}$ of the $1s$ pionic states in the three Sn isotopes and three light symmetric nuclei (Suzuki *et al.*, 2004).

bution, are shown in Fig. 25 in open diamonds and open squares, respectively. The best-fit values were obtained by using the parameters halfway between these two assumptions. The two crosses in the figure indicate the dependence of b_1 on the uncertainty of ± 0.04 fm in Δ_{np} . The quoted errors on the best-fit values do not include these uncertainties in the neutron distribution³.

In-medium quark condensate

From the observed enhancement of the b_1 parameter relative to the free value, $b_1/b_1(\rho) = 0.78 \pm 0.05$, Suzuki *et al.* (2004) deduced that the chiral order parameter f_π is subject to the in-medium reduction of $(f_\pi^t(\rho)/f_\pi)^2 \simeq 0.64$ at the normal nuclear density $\rho = \rho_0$, based on the suggestion (Kienle and Yamazaki, 2001; Weise, 2000, 2001b) that the missing repulsion may be explained in terms of a possible in-medium change of the pion decay constant. A global fit (Friedman, 2002a,b) to the pionic x-ray as well as the deeply-bound ^{205}Pb data (Geissel *et al.*, 2002) supported this view. Recent direct calculation of $b_1/b_1(\rho)$ in the unitarized chiral approach (Fig. 26) is also consistent with the above result (Döring and Oset, 2008).

Here, we adopt a new model independent relation obtained by exploiting operator relations in QCD, Eq.(II.43). Jido *et al.* (2008) showed that $Z_\pi^{1/2}(\rho) \simeq \left(1 - \gamma \frac{\rho}{\rho_0}\right)$, with $\gamma = 0.184$. Using $b_1/b_1(\rho) = 0.78$ at $\rho = 0.6\rho_0$, the ratio of the quark condensates is found to be

$$\frac{\langle \bar{q}q \rangle_\rho}{\langle \bar{q}q \rangle} \simeq 1 - 0.37 \frac{\rho}{\rho_0}. \quad (\text{III.74})$$

³ Recently, Terashima *et al.* (2008) have determined the neutron rms radii of Sn isotopes using proton elastic scattering at 295 MeV. Their results are in good agreement with the radii assumed in (Suzuki *et al.*, 2004). See Fig. 24

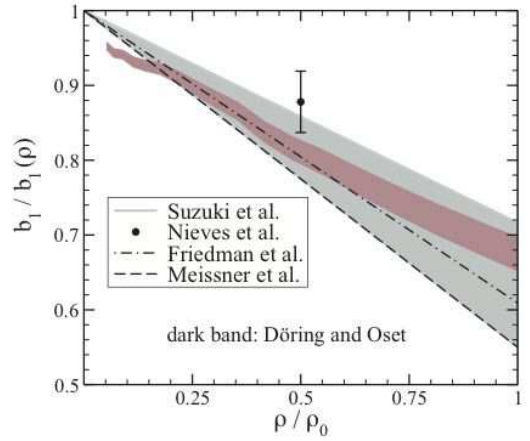


FIG. 26 In-medium isovector $b_1(\rho)$ compared to the vacuum isovector term b_1 . The gray band, the experimental result from Suzuki *et al.* (2004), is compared with chiral calculations by Döring and Oset (2008) (dark band), Meissner *et al.* (2002) (dashed line) and Friedman *et al.* (2004) (dash-dot line). The point is a phenomenological fit by Nieves *et al.* (1993). From Döring and Oset (2008)

A similar conclusion, $\langle \bar{q}q \rangle_\rho / \langle \bar{q}q \rangle \simeq 1 - 0.39\rho/\rho_0$, was obtained from the differential cross sections for π^\pm -nucleus elastic scattering data at 21.5 MeV (Friedman *et al.*, 2005, 2004).

IV. SCALAR MESON: σ IN NUCLEI

A. Theoretical background

The σ -meson in the vacuum is a very broad resonance in the scalar-isoscalar channel as discussed in Sec.II.B.2. It is an excitation having the same quantum number as the vacuum, and may be interpreted as the Higgs boson in QCD. The fate of such scalar-isoscalar excitation in hot and/or dense medium is strongly correlated with chiral symmetry restoration (Hatsuda and Kunihiro, 1985, 1987a). The basic idea is rather simple and general: If a sizable reduction of the chiral condensate takes place in the medium, the ground state becomes “soft” against the amplitude fluctuation of the order parameter due to the reduction of the stiffness. In fact, the frequency of the σ excitation (the amplitude fluctuation) is red-shifted toward the frequency of the π excitation (the phase fluctuation). Similar softening phenomena are well known in solid state physics, e.g., the soft phonon modes in anti ferro-elastic crystals such as SrTiO_3 (Gebhardt and Krey, 1980) and in ferro-electric crystals such as SbSI (Kittel, 2004).

In the case of QCD, an interesting signal associated with the chiral softening is the spectral enhancement in the scalar-isoscalar channel near the 2π threshold at finite temperature and density as mentioned in Sec.II.C.7. Consider the retarded propagator of σ at

rest in the medium, $D_\sigma(\omega)$. The spectral function is defined as $\rho_\sigma = -\frac{1}{\pi}\text{Im}D_\sigma = \frac{1}{\pi}\text{Im}D_\sigma^{-1}/[(\text{Re}D_\sigma^{-1})^2 + (\text{Im}D_\sigma^{-1})^2]$. Because of the softening and strong $\sigma\pi\pi$ coupling, $\text{Re}D_\sigma^{-1}(\omega \simeq 2m_\pi)$ becomes small or even vanishes at a certain temperature or baryon density. In that situation, the spectral function is dominated by the imaginary part of the inverse propagator with the phase space factor (Chiku and Hatsuda, 1998a,b; Hatsuda *et al.*, 1999; Volkov *et al.*, 1998),

$$\rho_\sigma(\omega) \simeq \frac{1}{\pi} \frac{1}{\text{Im}D_\sigma^{-1}(\omega)} \propto \frac{\theta(\omega - 2m_\pi)}{\sqrt{1 - \frac{4m_\pi^2}{\omega^2}}}. \quad (\text{IV.75})$$

This implies a large enhancement of the spectral function near 2π threshold. Such an enhancement may be seen in, e.g., the dipion production and diphoton production from the hot/dense medium. Also, a σ -mesic nuclei (or the bound dipion in nuclei) could be formed by (d, t) , $(d, {}^3\text{He})$ and (γ, p) reactions, if there is large enough softening (Hirenzaki *et al.*, 2002; Nagahiro *et al.*, 2005).

In reality, the pion has a width inside the medium, so that the spectral function in the σ -channel does not have a simple form such as Eq.(IV.75). Nevertheless, more sophisticated approaches indicate similar enhancement of the in-medium $\pi\pi$ scattering amplitude in the scalar-isoscalar channel near the 2π threshold (see the references cited in Sec.II.C.7). Shown in Fig. 27 is one of such examples obtained by using the chiral unitary model. Here we note that the expansion parameter of the non-linear chiral models is a ratio, [typical momentum of the pion or nucleon fields]/ [chiral symmetry breaking scale $4\pi f_\pi$]. Therefore, non-linear chiral approaches lose their predictive power at high temperature and/or high baryon density.

B. Experiments

1. CHAOS

The CHAOS (Canadian high acceptance orbit spectrometer) collaboration at TRIUMF was the first to report such a low-mass enhancement in the $(\pi\pi)_{I=J=0}$ channel. They used $\pi^+A \rightarrow \pi^+\pi^-X$ reactions on hydrogen (Kermani *et al.*, 1998) and on nuclear targets (Bonutti *et al.*, 1996, 1997, 1999, 2000; Camerini *et al.*, 2004, 2001; Grion *et al.*, 2005) at pion kinetic energy $T_\pi = 243 - 305$ MeV, and observed the spectral “softening” in the $\pi^+\pi^-$ channel but not in the $\pi^+\pi^+$ (i.e., $I = 2$) channel. The nuclear data were taken at $T_\pi = 283$ MeV on ${}^2\text{H}$, ${}^{12}\text{C}$, ${}^{40}\text{Ca}$ and ${}^{208}\text{Pb}$ targets, as well as at $T_\pi = 243, 264, 284, 305$ MeV on ${}^{45}\text{Sc}$.

Figure 28 shows a typical reconstructed $\pi^+\pi^-$ event. The spectrometer is based on a cylindrical dipole magnet producing vertical magnetic fields up to 1.6 T (0.5 T for the 2π experiments)(Smith *et al.*, 1995). The target is located in the center of the magnet. Charged particle tracks produced by pion interactions are identified using four concentric cylindrical wire chambers (WC1, 2,

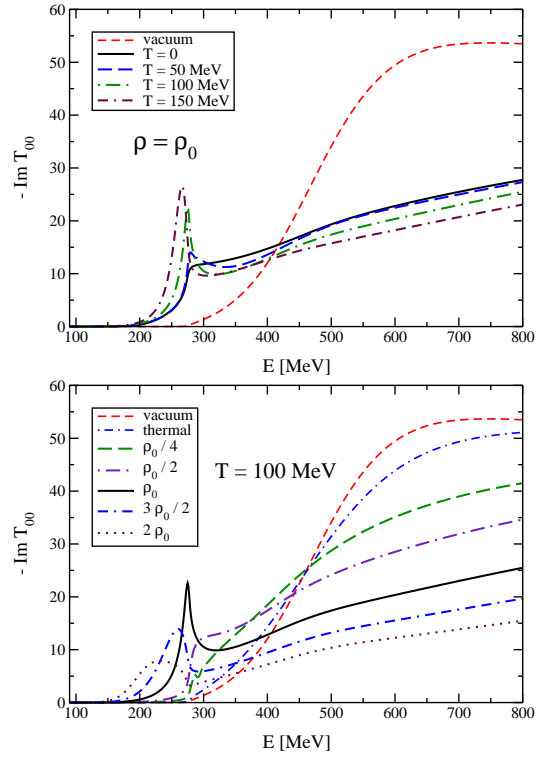


FIG. 27 Imaginary part of the $\pi - \pi$ amplitude $T_{00}(E)$ in the scalar-isoscalar channel calculated in the chiral unitary model (Cabrera *et al.*, 2008).

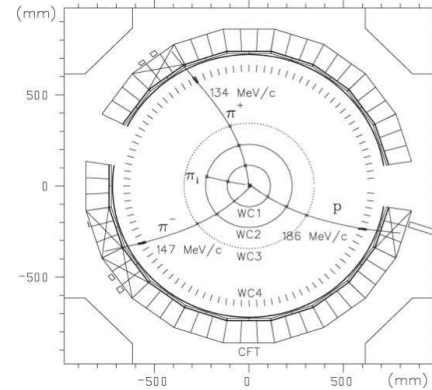


FIG. 28 A typical reconstructed event in CHAOS for the $\pi_i^+ \rightarrow \pi^+\pi^-p$ reaction on ${}^{12}\text{C}$. WCs are the four wire chambers, CFTs are the CHAOS First-level Trigger counters, which are also used for particle identification. Of the 20 CFTs, two are removed to free the pion beam path. (Bonutti *et al.*, 2000).

3, 4) surrounding the target. Particles are identified by cylindrical layers of scintillation counters and lead-glass Čerenkov counters, which also provide a first level trigger (CFTs). The detector subtends approximately 10% of 4π . The momentum resolution delivered by the detector system is 1% . The pion-detection threshold energy is 11 MeV.

Fig. 29 shows the $\pi^+\pi^-$ (left) and $\pi^+\pi^+$ (right)

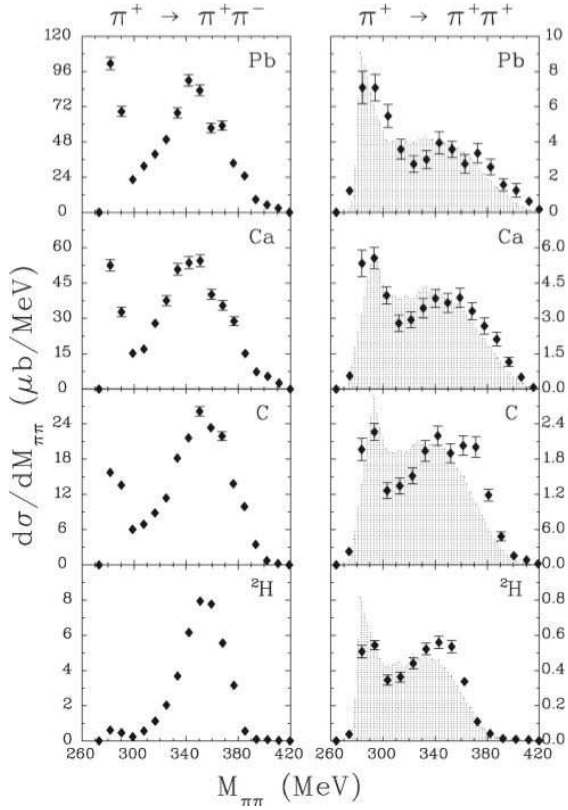


FIG. 29 Invariant mass distributions (diamonds) for the $\pi^+ \rightarrow \pi^+\pi^-$ and $\pi^+ \rightarrow \pi^+\pi^+$ reactions on ${}^2\text{H}$, ${}^{12}\text{C}$, ${}^{40}\text{Ca}$ and ${}^{208}\text{Pb}$. The shaded regions represent the results of phase-space simulations for the pion-production reaction $\pi A \rightarrow \pi\pi N[A-1]$ (Bonutti *et al.*, 2000).

invariant-mass spectra taken on nuclear targets. The distributions span the range from $2m_\pi$ up to the 420 MeV, the maximum allowed by the reaction. While the $\pi^+\pi^+$ spectra can be fairly well represented by the phase-space simulations (shaded region), the $\pi^+\pi^-$ spectra show a peak in the low-mass region, increasing with mass number A .

Instead of comparing the raw spectra with theoretical predictions or with results of other experiments, a composite observable was used:

$$C_{\pi\pi}^A = \frac{\sigma(M_{\pi\pi}^A)/\sigma_T^A}{\sigma(M_{\pi\pi}^N)/\sigma_T^N},$$

where $\sigma(M_{\pi\pi}^A)$ ($\sigma(M_{\pi\pi}^N)$) is the triple differential cross section $d^3\sigma/dM_{\pi\pi}d\Omega_\pi d\Omega_\pi$ for nuclei (nucleon), $M_{\pi\pi}$ represents the $\pi\pi$ invariant mass, Ω_π denotes the pion-detection solid angle, and σ_T^A (σ_T^N) is the total cross section in nuclei (nucleon). The ratios are presented in Fig. 30. The ratios $C_{\pi^+\pi^-}^A$ (right panel) show that the low-mass $\pi^+\pi^-$ pairs are more abundant in heavier targets, while no such trend can be seen in $C_{\pi^+\pi^+}^A$ (left panel).

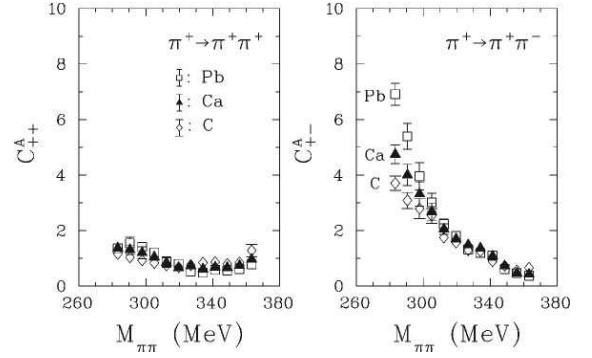


FIG. 30 (left): $C_{\pi\pi}^A$, the bin-by-bin ratio (see text) of $\pi\pi$ invariant mass distributions for the two reactions $\pi^+A \rightarrow \pi^+\pi^+A'$ and $\pi^+p \rightarrow \pi^+\pi^+n$, as a function of the $M_{\pi\pi}$ energy. The nuclei (A) examined are ${}^2\text{H}$ (which plays the role of a proton, p), ${}^{12}\text{C}$ (open diamonds), ${}^{40}\text{Ca}$ (full triangles), and ${}^{208}\text{Pb}$ (open squares). (right): Same as the left panel but for the $\pi^+ \rightarrow \pi^+\pi^-$ reaction channel (Bonutti *et al.*, 1999).

2. Crystal Ball

The Crystal Ball (CB) collaboration at the AGS investigated the $\pi^-A \rightarrow \pi^0\pi^0A'$ reaction on CH_2 , CD_2 , C , Al and Cu targets at $p_{\pi^-} = 408 \text{ MeV}/c$ (Starostin *et al.*, 2000). The Crystal Ball comprises 672 optically isolated NaI(Tl) crystals that cover 93% of 4π , and has a $\pi^0\pi^0$ acceptance of 11 – 17%. The invariant mass resolution is about 1.2% at $m_{\pi^0\pi^0} = 2m_{\pi^0}$ and reaches a plateau of 2.2% at $m_{\pi^0\pi^0} \simeq 0.3 \text{ GeV}/c^2$. The measured $\pi^0\pi^0$ invariant-mass spectra (left panel of Fig. 31) show a gradual shift of intensity towards lower $m_{\pi\pi}$ for heavier targets, but a sharp strong peak near $2m_\pi$ as reported by the CHAOS collaboration cannot be seen.

However, Camerini *et al.* (2001) pointed out that if the composite ratios $C_{\pi\pi}^A$ are used to compare the CHAOS and CB results, so as to (mostly) remove uncertainties arising from acceptance corrections⁴, the two results are not statistically inconsistent, at least in the case of ${}^{12}\text{C}$ (the only nucleus common to the two experiments). See Fig. 31 right panel.

3. TAPS

The TAPS (Two Arms Photon Spectrometer) collaboration used the tagged photon facility at the MAMI accelerator (Anthony *et al.*, 1991) to measure $A(\gamma, \pi^0\pi^0)$ as well as $A(\gamma, \pi^0\pi^{+/-})$ cross sections (Bloch *et al.*, 2007; Messchendorp *et al.*, 2002).

The experiment covered the photon energy range from 200800 MeV with an energy resolution of 2 MeV per

⁴ Note that the CHAOS acceptance is about 10% of 4π while that of Crystal Ball is 93% of 4π . The small acceptance of CHAOS may be the origin of the sharp peaks close to the threshold.

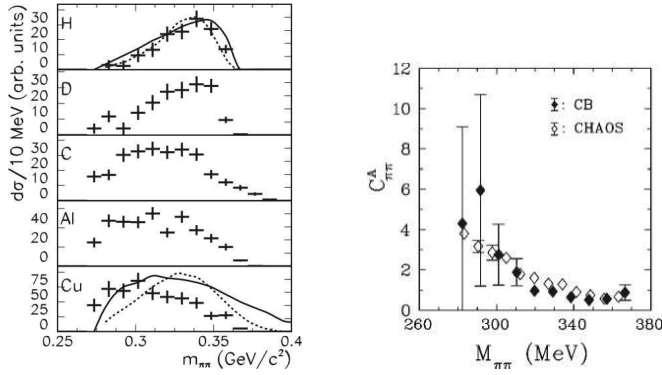


FIG. 31 (Left) Experimental results for the $2\pi^0$ invariant mass distributions obtained for the H, D, C, Al, and Cu targets corrected for Crystal Ball acceptance. The vertical scale is in arbitrary units. The solid lines show the results of calculations made for the TAPS group by Rapp, and the dashed line is the prediction by Vicente Vacas. (Starostin *et al.*, 2000). (Right) The composite ratios $C_{\pi\pi}^A$ as a function of the $\pi\pi$ invariant mass for the ^{12}C target. Full diamonds, the $C_{\pi^0\pi^0}^C$ distribution deduced from the CB data of Starostin *et al.* (2000); open diamonds, the CHAOS $C_{\pi^+\pi^-}^C$ distribution taken from Bonutti *et al.* (1999) (Camerini *et al.*, 2001).

tagger channel. The targets used were ^1H , ^{12}C , $^{\text{nat}}\text{Pb}$ (Messchendorp *et al.*, 2002) as well as ^{40}Ca (Bloch *et al.*, 2007). The reaction products from the target were detected with the electromagnetic calorimeter TAPS, comprising 510 hexagonally shaped BaF_2 crystals of 25 cm length with an inner diameter of 5.9 cm. They were arranged in six blocks of 64 modules and a larger forward wall of 138 modules (see Fig. 32). The blocks were arranged in one plane around the target at a distance of 55 cm from the target center and at polar angles of $\pm 54^\circ$, $\pm 103^\circ$, and $\pm 153^\circ$, while the forward wall was placed 60 cm away from the target center at 0° and the photon beam passed through a hole in the center of the forward wall. Each detector module was equipped with an individual plastic veto detector, read out by a separate photomultiplier. The setup covered 37% of the full solid angle. The two- π^0 invariant-mass resolution was between 2.0% and 2.5% in the incident-photon energy range of interest.

Figure 33 shows the $\pi^0\pi^0$ (left) and $\pi^0\pi^+/\pi^0\pi^-$ (right) spectra measured at the incident photon energy range of 400 – 460 MeV. This energy range was chosen so that its centroid corresponds to the same center-of-mass energy as was used in the pion-induced experiments, enabling a direct comparison. Since this range is below the η -production threshold of 550 MeV, the event identification is clean. Figure 33 indicates that the strength in the distribution of $M_{\pi^0\pi^0}$ (but not $M_{\pi^0\pi^+/\pi^-}$) is shifted towards smaller invariant masses with increasing A .

A more recent analysis of $^{40}\text{Ca}(\gamma, \pi\pi)$, with higher statistics by Bloch *et al.* (2007), shown in Fig. 34, revealed that the invariant-mass spectra show a similar

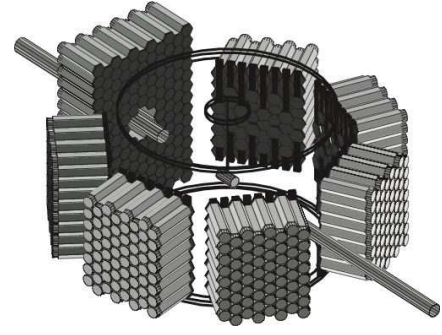


FIG. 32 Setup of the TAPS detector at the Mainz MAMI accelerator. The beam entered the target chamber from the lower right edge. (Bloch *et al.*, 2007; Kermani *et al.*, 1998)

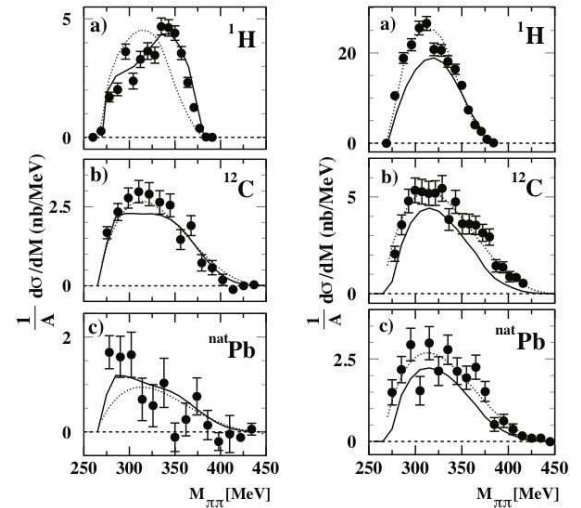


FIG. 33 (Left) Mass-number-normalized differential cross sections of the reaction $A(\gamma, \pi^0\pi^0)$ with $A = ^1\text{H}, ^{12}\text{C}, ^{\text{nat}}\text{Pb}$. (Right) The same for the reaction $A(\gamma, \pi^0\pi^\pm)$. Both panels are for incident photons in the energy range of 400 – 460 MeV (solid circles). Error bars denote statistical uncertainties. The dotted curves indicated phase-space distributions determined by the Monte Carlo model, and the solid curves are predictions by (Roca *et al.*, 2002). From Messchendorp *et al.* (2002).

softening effect as already found in Messchendorp *et al.* (2002) for carbon and lead nuclei⁵, and that the strength of the effect is comparable to carbon, but they also found that a sizable part of the in-medium effects can be explained by final-state interaction effects, namely, pion rescattering, as discussed below.

⁵ Note that the cross-section ratios $\sigma(\pi^0\pi^\pm)/\sigma(\pi^0\pi^0)$ are about 2 in Fig. 33, while they are about 5 in Fig. 34. This is likely due to the larger systematic errors in the $\pi^0\pi^\pm$ cross sections in Messchendorp *et al.* (2002) (Krusche, 2008).

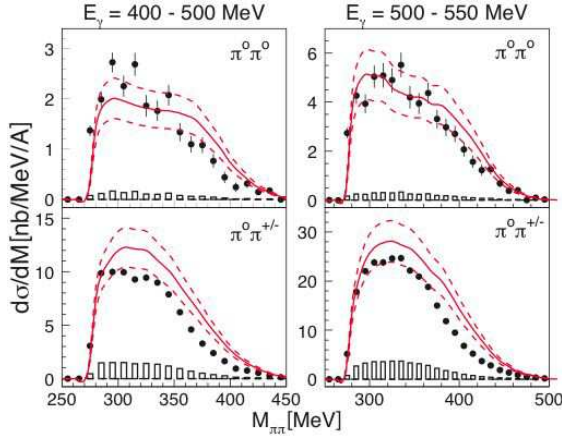


FIG. 34 Pion-pion invariant-mass distributions compared to results of the BUU model (Buss *et al.*, 2006). The bars at the bottom represent the systematic uncertainty of the data, the dashed lines represent the error band for the BUU calculation (Bloch *et al.*, 2007).

C. Final-state interaction (FSI) effects

The solid curves in Fig. 33 are predictions by Roca *et al.* (2002). Here, the meson-meson interaction in the $I = J = 0$ channel is studied in the framework of a chiral-unitary approach at finite baryon density. The model dynamically generates the σ resonance, reproducing the meson-meson phase shifts in vacuum and accounts for the absorption of the pions in the nucleus. In the model, the $\pi - \pi$ FSI modified by the nuclear medium produces a shift of strength of the $\pi\pi$ invariant mass distribution induced by the moving of the σ pole to lower masses and widths as the nuclear density increases. The data are described well by the model considering a theoretical uncertainty of 20%.

On the other hand, the curves in Fig. 34 are the results of the semi-classical Boltzmann-Uehling-Uhlenbeck (BUU) calculation (Buss *et al.*, 2006), which reproduce both $\pi^0\pi^0$ and $\pi^0\pi^{+/-}$ data reasonably well. This model does not contain the $\pi - \pi$ final-state interactions, but the “softening” of the $\pi^0\pi^0$ spectra is due to charge-exchange pion-nucleon scattering (i.e., $\pi - N$ FSI) which mixes the contributions from the different charge channels. Since the total cross-section for $\pi^0\pi^\pm$ production is much larger than the $\pi^0\pi^0$ cross-section, the latter receives significant side feeding from the mixed charge channel via $\pi^\pm N \rightarrow \pi^0 N$ scattering, which increases the fraction of re-scattered low-energy pions in this channel. In the same way, re-scattering of $\pi^+\pi^-$ contributes to the $\pi^0\pi^\pm$ channel.

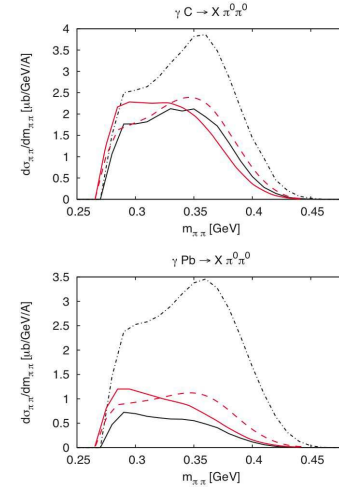


FIG. 35 (color) Two-pion invariant mass distributions for $\pi^0\pi^0$ photoproduction off ^{12}C and ^{208}Pb for $E_\gamma = 0.4 - 0.46$ GeV, calculated by Buss *et al.* (2006). Results without final-state interactions (black dash-dotted lines), and with FSI (black solid lines). These are compared with the results obtained by (Roca *et al.*, 2002), with in-medium final $\pi\pi$ interaction (red solid lines) and with the free-space $\pi\pi$ interaction (red dashed lines).

V. VECTOR MESONS: ρ, ω, ϕ IN NULCEI

A. Theoretical background

As is discussed in Sec.II.B.3, the direct signature of chiral restoration is the degeneracy between the vector spectral function ρ_V and axial-vector spectral function ρ_A . Since the vector current couples to virtual photons which eventually decay into dileptons (l^+l^-), ρ_V is directly related to the physical observable. For example, the emission rate of dileptons (number of dileptons emitted per space-time volume d^4x and per energy-momentum volume d^4p) from the hot/dense matter reads

$$\frac{d^8 N_{l^+l^-}}{d^4x d^4p} = \frac{\alpha^2}{3\pi^2 p^2} \frac{(2\rho_V^T + \rho_V^L)(\omega, \mathbf{p})}{e^{\omega/T} - 1} I(m_l^2/p^2). \quad (\text{V.76})$$

Here $p^\mu = (\omega, \mathbf{p})$ is the total four momentum of l^+ and l^- , the superscript T (L) implies transverse (longitudinal) and $I(z) = (1 + 2z)(1 - 4z)^{1/4}\theta(1 - 4z)$ with $z = m_l^2/p^2$ denotes the phase space correction from the finite lepton mass, m_l . Unlike the case of ρ_V , it is difficult to measure ρ_A by dilepton, since the decay occurs through Z^0 and is highly suppressed at low energies.

The spectral constraints on ρ_V itself are obtained from the operator product expansion (Hatsuda *et al.*, 1993; Hatsuda and Lee, 1992) similar to the derivation of the Weinberg-type sum rules in Sec.II.B.3:

$$\int_0^\infty \frac{d\omega^2}{\omega^2} (\rho_V(\omega) - \rho_{\text{pQCD}}(\omega)) = 0, \quad (\text{V.77})$$

$$\int_0^\infty d\omega^2 (\rho_V(\omega) - \rho_{\text{pQCD}}(\omega)) = \sum_i C_4^i \langle \mathcal{O}_4^i \rangle, \quad (\text{V.78})$$

$$\int_0^\infty d\omega^2 \omega^2 (\rho_V(\omega) - \rho_{\text{pQCD}}(\omega)) = \sum_i C_n^i \langle \mathcal{O}_6^i \rangle. \quad (\text{V.79})$$

Here \mathcal{O}_n^i are the local composite operators with dimension n with Lorentz indices in general, and C_n^i are the corresponding Wilson coefficients. In the SU(2) chiral limit $m_{u,d} = 0$, \mathcal{O}_4^i are all chirally symmetric, while \mathcal{O}_4^i contain both chirally symmetric and non-symmetric operators. Also, $\rho_{\text{pQCD}}(\omega)$ is the spectral function which reproduces the perturbative calculation of the correlation function (the l.h.s. of Eq.(II.31)) in the deep Euclidean region ($\omega^2 \rightarrow -\infty$). Then, $\rho_{\text{pQCD}}(\omega)$ is chirally symmetric by definition. These are the reasons why the Weinberg-type sum rules with only chirally asymmetric condensates in Sec.II.B.3 are obtained by taking the difference between vector and axial-vector correlations. Since chirally symmetric condensates do not have to vanish at the critical point of the chiral transition, one cannot immediately relate the spectral modification of vector mesons to the restoration of chiral symmetry.

Even if in-medium changes of $\langle \mathcal{O}_{4,6}^i \rangle$ are obtained exactly from lattice QCD simulations, the above sum rules only supply information on the weighted averages of the spectral function and not on the exact spectral shape. Nevertheless, these sum rules are useful to make a consistency check in various models of QCD (Klingl *et al.*, 1997; Kwon *et al.*, 2008). Also, these sum rules may be used to extract the information on $\langle \mathcal{O}_{4,6}^i \rangle$ by adopting the experimental dilepton spectrum after background subtraction in the l.h.s. of Eqs.(V.78,V.79) (Hatsuda, 1997).

In general, the spectral function receives peak-shift, broadening, new peaks, etc due to the complex interaction of the vector current with the medium (Rapp and Wambach, 2000). Also, such spectral changes may well depend on the spatial momentum of the current (Eletsky and Ioffe, 1997; Friman *et al.*, 1999; Jean *et al.*, 1994). Indeed, the transverse and longitudinal spectral functions $\rho_{V,A}^{\text{T,L}}(\omega, \mathbf{p})$ obey different Weinberg-type sum rules for $\mathbf{p} \neq 0$ (Kapusta and Shuryak, 1994). Because of these reasons, it is not appropriate to oversimplify the problem to “mass shift vs. width broadening”. Nevertheless, there is a theoretical suggestion that the width broadening at low temperature and/or baryon density is eventually taken over by the mass shift near the critical point of chiral transition (Yokokawa *et al.*, 2002)(Brown *et al.*, 2008). Experimentally, it is important to measure the full momentum dependence of the spectral function $\rho_V^{\text{T,L}}(\omega, \mathbf{p})$ instead of the projected invariant-mass spectra.

B. Dileptons, why and how?

Dileptons (l^+l^- pairs, where $l = e$ or μ) are an excellent tool to study possible in-medium modifications of vector mesons (Table I), ρ, ω and ϕ in nuclear media, because of their negligible final-state interactions. Due to their short lifetime, ρ^0 mesons have larger probabil-

ity of decaying in medium, while ω and ϕ tend to decay outside. In order to study ω/ϕ in-medium properties, it is important to choose a proper reaction and to select slow-moving mesons.

Obtaining dilepton distributions (usually presented in the form of l^+l^- invariant-mass spectra $M_{l^+l^-}$) is technically very demanding because of the small dilepton-decay branching ratios of these mesons (Tab. I), while there are many hadronic sources which can produce leptons. The detector therefore must have an excellent lepton-identification capability, and must also provide means to suppress combinatorial background, the background caused by an l^+ being erroneously paired up with an l^- from other origin (e.g., a e^+ from $\pi^0 \rightarrow \gamma e^+e^-$ paired up with an e^- from $\gamma \rightarrow e^+e^-$ occurring in the same event).

Even with the start-of-the-art dilepton detectors, the combinatorial background is severe, especially in high-energy heavy-ion collisions. For example, at CERN SPS (158 AGeV central collisions), the NA60 experiment ($\mu^+\mu^-$) reported a signal S to background B ratio of about 1/11 (Damjanovic, 2007), and it was about 1/22 in the case of the CERES experiment (e^+e^-) (Adamová *et al.*, 2008). At RHIC ($\sqrt{s_{NN}} = 200$ GeV Au+Au minimum bias), the PHENIX experiment (e^+e^-) reported a signal-to-background ratio of about 1/100 (Afanasiev *et al.*, 2007).

In order to reliably extract meaningful results despite such small signal-to-background ratios, methods such as event mixing and like-sign pair subtraction have been developed to reliably subtract combinatorics, as discussed in section V.B.3.

The combinatorics-subtracted $M_{l^+l^-}$ distribution still contains a broad continuous background due to Dalitz decays. In order to extract the vector-meson contributions, the measured distribution is compared with the “hadronic cocktail”, which contains all known sources of l^+l^- pairs produced in the detector acceptance.

1. $\mu^+\mu^-$ -pair detection

Muons produced in pion and kaon decays (e.g., $\pi^+ \rightarrow \mu^+\bar{\nu}$ and $K^+ \rightarrow \mu^+\bar{\nu}$) are much more abundant than those from vector-meson decays, and they contribute to the combinatorial background. It is therefore essential to absorb hadrons as close as possible to the interaction point in a thick absorber. Muon momenta are measured by magnetic spectrometer(s) placed behind the absorber, corrected for the energy loss and multiple scattering in the absorber, and the pair-mass distribution is reconstructed. This is exactly how $\Upsilon(b\bar{b})$ was first discovered by Herb *et al.* (1977).

This method works well for heavy-mass region (Υ as well as J/Ψ), where the decay-muons have high momenta, and the particle multiplicities are low, but the measurement of low-mass vector mesons is difficult due to larger combinatorial background and larger multiple scattering in the absorber (hence lower mass resolution).

TABLE I Properties of vector mesons. (Amsler *et al.*, 2008)

	Mass (MeV/c ²)	Γ (MeV/c ²)	$c\tau$ (fm)	Main decay	$\frac{\Gamma_{e^+e^-}}{\Gamma_{\text{tot}}}$ * ($\times 10^{-5}$)	$\frac{\Gamma_{\mu^+\mu^-}}{\Gamma_{\text{tot}}}$ * ($\times 10^{-5}$)	$\frac{\Gamma_{\pi^0\gamma}}{\Gamma_{\text{tot}}}$ *
ρ^0	775.49 ± 0.34	149.4 ± 1.0	1.3	$\pi^+\pi^-$ ($\sim 100\%$)	4.7	4.6	6.0×10^{-4}
ω	782.65 ± 0.12	8.49 ± 0.08	23.2	$\pi^+\pi^-\pi^0$ (89%)	7.2	9.0	8.9%
ϕ	1019.455 ± 0.020	4.26 ± 0.04	46.2	K^+K^- (49%)	29.7	28.6	12.7×10^{-4}

* These branching ratios are at the pole mass.

HELIOS/3 and NA60 at CERN SPS overcame these difficulties and successfully measured the dimuon spectra all the way down to the pair-mass threshold of $2m_\mu$.⁶

2. e^+e^- -pair detection

The spectrometer used in the discovery of $J/\Psi(c\bar{c})$ in the $p + \text{Be} \rightarrow e^+e^-X$ reaction (Aubert *et al.*, 1974) contains the essence of e^+e^- measurement, such as (i) excellent electron identification (hadron rejection), (ii) good momentum (pair-mass) resolution, and (iii) importance of rejecting e^+e^- pairs from photon conversion and Dalitz decays.

In the e^+e^- spectra, severe background sources are photons from meson decays such as $\pi^0 \rightarrow 2\gamma$ converting in the target ($\gamma \rightarrow e^+e^-$) and in detectors, and the Dalitz decays such as $\pi^0 \rightarrow \gamma e^+e^-$, $\eta \rightarrow \gamma e^+e^-$, $\eta' \rightarrow \gamma e^+e^-$ and $\omega \rightarrow \pi^0 e^+e^-$.

Although pairs from these sources have small opening angles and low masses, the limited track reconstruction efficiency and acceptance lead to a combinatorial background for events in which two or more of these low-mass pairs are only partially reconstructed. This is *the* central problem of any low-mass e^+e^- -pair experiment.

3. Combinatorial background

Uncorrelated sources can produce, in addition to unlike-sign (l^+l^-) pairs, like-sign (l^+l^+ and l^-l^-) pairs. Most experiments make use of this fact in evaluating the combinatorial background.

A typical method of subtracting the combinatorial background is as follows (Toia, 2006, 2007): Under the assumption that electron and positron multiplicities are

Poisson-distributed, and that the like sign pairs are uncorrelated, the combinatorial background B can be accounted for by

$$B = 2\sqrt{N^{++}N^{--}}, \quad (\text{V.80})$$

where N^{++} and N^{--} are the number of measured l^+l^+ and l^-l^- pairs, respectively. The number of signal pairs S is then obtained as $S = N^{+-} - B$, where N^{+-} is the number of measured unlike-sign pairs.

This would work if the detector acceptance is the same for like and unlike sign pairs, and if a sufficient number of like-sign pairs are collected. This is in general not the case. A mixed event technique is then used to compute the combinatorial background. In this method, unlike-sign tracks from different events (with similar event topology) are paired. Since the same track can be used many times, paired up with tracks from different events, the background spectra can be generated with high statistics. The accuracy of the technique can be tested by comparing the shape of the measured like-sign pair spectrum with that of the mixed combinatorial background. The generated background event distribution can be normalized to the number of expected unlike-sign pairs from Eq.(V.80).

C. High Energy Heavy Ion Reactions

Although the main subject of the present review is the behavior of mesons produced in nuclei with elementary reactions, we nevertheless touch upon the low-mass ($\lesssim 1\text{GeV}/c^2$) dileptons observed in heavy-ion collisions.

An enhanced yield of dilepton pairs in the low-mass region is ubiquitous from 1 AGeV (Bevalac/SIS), through SPS energies (40 – 200 AGeV), up to the RHIC energy of $\sqrt{s_{NN}} = 200$ GeV. Here, the “enhancement” is defined as the excess of the observed l^+l^- yield over the sum of the “hadronic cocktail” as discussed above.

⁶ Since muons must be energetic enough to penetrate the hadron absorber, the rapidity of the reconstructed pairs are high, e.g., $3.3 < y < 4.3$ in the case of NA60 (Damjanovic, 2007). For e^+e^- , pairs can be measured in the mid-rapidity region of $2.1 < \eta < 2.65$ (Agakichiev *et al.*, 2005).

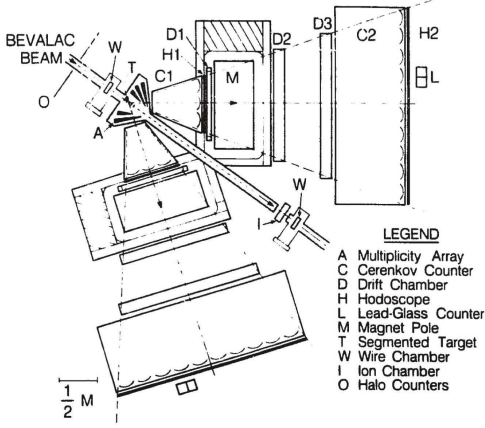


FIG. 36 Top view of the DLS (dilepton spectrometer) at Bevalac (Yegneswaran *et al.*, 1990).

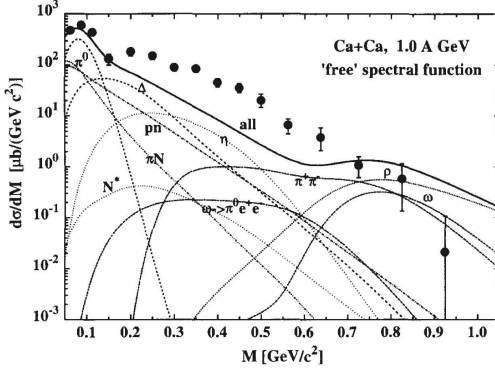


FIG. 37 The dilepton spectrum for Ca+Ca at 1.0 AGeV measured by the DLS collaboration (circles) (Porter *et al.*, 1997), compared with the “hadronic cocktail” assuming the “free” ρ spectral function (Bratkovskaya *et al.*, 1998).

1. Bevalac/SIS energies (1 ~ 2AGeV)

DLS

The first anomalous dilepton excess was reported by the DLS (dilepton spectrometer) experiment at Bevalac (1AGeV). Using a two-arm spectrometer as shown in Fig. 36, with a pair-mass resolution of $\Delta M/M \sim 10\%$, they succeeded for the first time to measure the dilepton spectra in heavy-ion collisions (Porter *et al.*, 1997). When the measured spectra were compared with transport theory calculations (Bratkovskaya and Cassing, 2008; Cassing and Bratkovskaya, 1999; Cozma *et al.*, 2006; Ernst *et al.*, 1998; Shekhter *et al.*, 2003), an excess of about a factor 6 – 7 was found in the mass range of $0.15 < M_{e^+e^-} < 0.4$ GeV (Fig. 37). Including the ρ -meson modifications in the medium (mass dropping) did not eliminate the discrepancy (the observed yield was still higher by about a factor of 3 over the HSD curve). This has become known as the “DLS puzzle”.

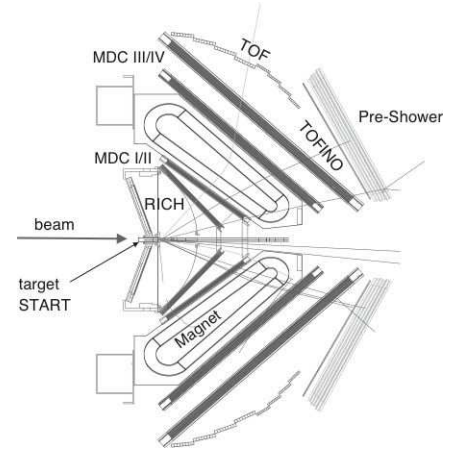


FIG. 38 A side view of HADES. The RICH detector, consisting of a gaseous radiator, a carbon fiber mirror and a tilted photon detector, is used for electron identification. Two sets of multiwire drift chambers (MDCs) are placed in front and behind the magnetic field to measure particle momenta. A time of flight wall (TOF/TOFNO) accompanied by a Pre-shower detector at forward angles is used for an additional electron identification and trigger purposes. For a reaction time measurement, a start detector is located near the target (Salabura *et al.*, 2004).

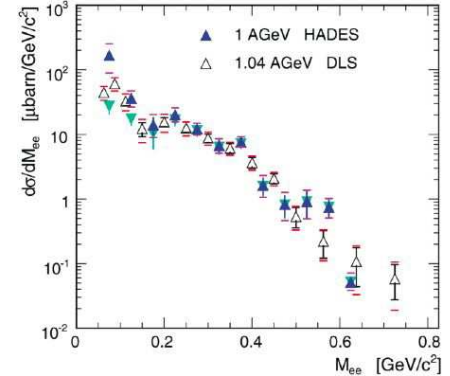


FIG. 39 Direct comparison of the dilepton pair mass distributions measured in C + C at 1 AGeV by HADES (within the DLS acceptance) and at 1.04 AGeV by DLS (Porter *et al.*, 1997). Statistical and systematic errors are shown. Overall normalization errors (not shown) are 20% for the HADES and 30% for the DLS data points (Agakishiev *et al.*, 2008).

HADES

This DLS puzzle has been recently revisited by the HADES (high acceptance dielectron spectrometer) collaboration at the heavy ion synchrotron SIS at GSI Darmstadt. HADES uses modern technologies such as a ring-imaging Čerenkov detector (RICH) to achieve good particle identification as well as a high mass resolution of $\Delta M/M \simeq 2.7\%$ (Fig. 38). They recently studied 1AGeV C + C collisions in a low-resolution mode ($\Delta M/M = 8\%$ at 0.8 GeV/ c^2 to emulate that of DLS) and projected the measured spectra into the DLS acceptance.

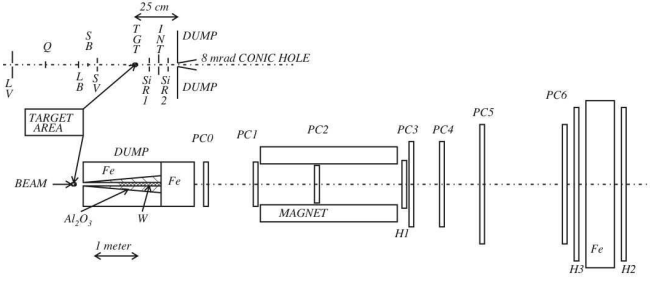


FIG. 40 Helios-3 setup (Angelis *et al.*, 2000).

The resulting spectrum, shown in Fig. 39, is consistent with that measured by DLS. For masses of $0.15 \text{ GeV}/c^2 < M_{e^+e^-} < 0.50 \text{ GeV}/c^2$ it exceeds expectations based on the known production and decay rates of hadrons (most important being the η meson) by a factor of about 7, thereby reconfirming the DLS data.

However, recent HADES measurements of $p + p \rightarrow e^+e^-X$ and $p + n \rightarrow e^+e^-X$ seem to show that the C + C spectrum at 1 AGeV agree well with the $\frac{1}{2}(pp + np)$ spectrum at 1.25 GeV, when scaled by the π^0 yield (Galatyuk *et al.*, 2009). This may be indicating that the DLS/HADES effect does not have nuclear (in-medium) origin, but that the NN bremsstrahlung cross sections are in fact larger than hitherto assumed (Kaptari and Kämpfer, 2006; Shyam and Mosel, 2003). With the enhanced bremsstrahlung cross sections implemented in the HSD transport code, Bratkovskaya and Cassing (2008) have recently shown that the calculated spectra agree well with DLS and HADES data.

2. SPS energies (40 ~ 200 AGeV)

At the CERN Super Proton Synchrotron (SPS), low-mass dilepton spectra were studied in the e^+e^- mode by the CERES collaboration, and in the $\mu^+\mu^-$ mode by the HELIOS/3 collaboration and the NA60 collaboration. These experiments all reported a low-mass dilepton enhancement.

HELIOS/3 ($\mu^+\mu^-$)

The HELIOS/3 experiment used a dimuon spectrometer shown in Fig. 40 to measure $\mu^+\mu^-$ distributions in proton on tungsten and sulphur on tungsten at 200 AGeV. The spectrometer consisted of a hadron absorber (placed 25 cm downstream from the target), six interaction lengths of Al_2O_3 and 100 cm of Fe, followed by a magnetic spectrometer and muon hodoscopes.

They found, by comparing the measured p -W and S-W dimuon distributions, each normalized to the charged-particle multiplicity (Fig. 41), an excess in S-W interactions relative to minimum-bias p -W interactions. The ob-

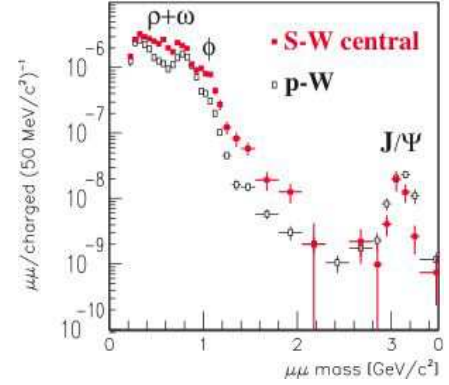


FIG. 41 $M_{\mu\mu}$ distribution normalized to the charged-particle multiplicity obtained by the HELIOS/3 collaboration for S-W (filled squares) and p -W (open squares) collisions at 200 AGeV (Angelis *et al.*, 2000).

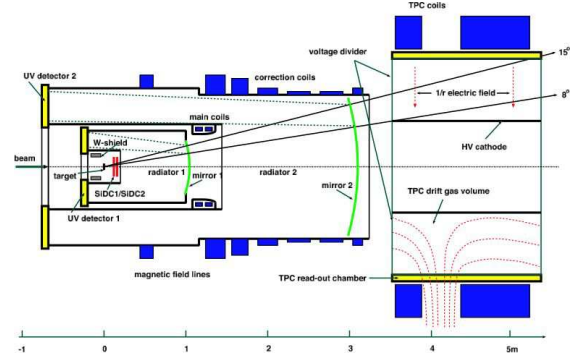


FIG. 42 Schematic view of the CERES spectrometer with a radial drift time projection chamber (TPC). The latter was added in NA45/2 for the Pb+Au runs (Marín, 2004).

served excess is continuous over the explored mass range and has no apparent resonant structure. In the low mass ($< 0.7 \text{ GeV}$) region the dimuon yield increases by $76 \pm 4\%$ of the corresponding p -W dimuon spectrum (in the higher mass region, the excess was higher).

CERES (NA45) (e^+e^-)

CERES is an innovative ‘hadron-blind’ axial-symmetric detector (Fig. 42) dedicated to the measurement of electron pairs in the low-mass range (up to $\sim 1.5 \text{ GeV}/c^2$). At the heart of CERES are the two coaxial ring-imaging Čerenkov detectors (shown in the left half of Fig. 42) having a high Čerenkov threshold of $\gamma_{\text{thr}} \simeq 32$, placed in a superconducting solenoid. With this setup, e^+e^- pairs in a window of $\Delta\eta = 0.53$ around mid-rapidity were selectively detected and reconstructed.

The dielectron pairs per charged particles, shown in Fig. 43 show that while the p -Be and p -Au data are reproduced within errors by Dalitz and direct decays of neutral mesons as known from p - p collisions, dielectrons from S-Au collisions reveal a substantial enhance-

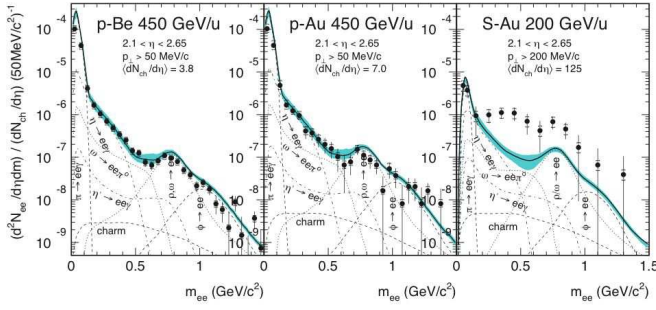


FIG. 43 CERES inclusive e^+e^- mass spectra of 450 GeV p -Be, p -Au, and 200 AGeV S-Au collisions (Agakichiev *et al.*, 1998, 1995). Plotted is the number of electron pairs per charged particle, both in the acceptance and per event. Contributions from various hadron decays as expected from p - p collisions are shown together with their sum (thick line), and the systematic error on the latter is indicated by the shaded area (Adamová *et al.*, 2008).

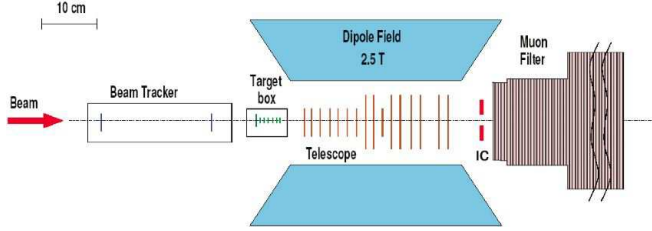


FIG. 44 Layout of the NA60 detectors in the vertex region (Usai, G. and others, 2005).

ment in the mass region $0.2 - 1.5 \text{ GeV}/c^2$ of a factor 5 (Agakichiev *et al.*, 1995).

This observation generated lots of excitement in the community. It has been attributed to the pion annihilation in the fireball, $\pi^+\pi^- \rightarrow \rho \rightarrow e^+e^-$ with a strong in-medium modification of the intermediate ρ , such as mass dropping (Brown and Rho, 2002) or broadening (Rapp and Wambach, 2000).

NA60 ($\mu^+\mu^-$)

The NA60 experiment added a telescope of radiation-tolerant silicon pixel detectors in between the target and the hadron absorber of the NA50 dimuon spectrometer (see Fig. 44). This enabled the collaboration to match muon tracks before and after the hadron absorber, both in angular and momentum space, thereby improving the dimuon mass resolution in the region of light vector mesons from ~ 80 to $\sim 20 \text{ MeV}/c^2$ (Arnaldi *et al.*, 2006; Damjanovic, 2007).

With this setup, NA60 succeeded to completely resolve ω and ϕ peaks in the In-In collisions at 158 AGeV, for the first time in nuclear collisions. This is shown in Fig. 45 (the mixed-event technique was employed here to subtract the combinatorial background).

By adjusting the cross section ratios η/ω , ρ/ω and ϕ/ω ,

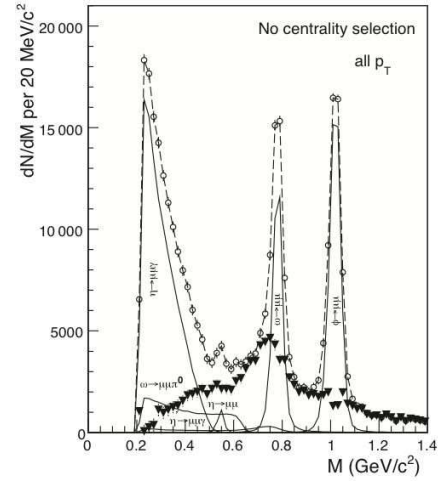


FIG. 45 Isolation of an excess above the hadron decay cocktail (see text). Total data (open circles), individual cocktail sources (solid), difference data (thick triangles), sum of cocktail sources and difference data (dashed) (Arnaldi *et al.*, 2006; Damjanovic, 2007).

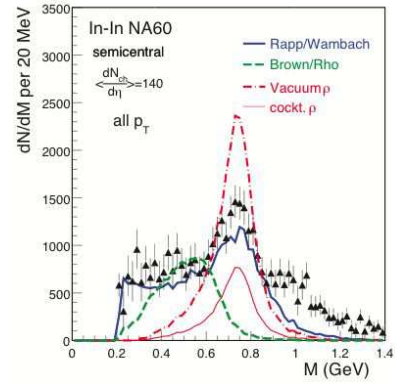


FIG. 46 Comparison of the excess mass spectrum for the semi-central bin to model predictions, made for In-In at $dN_{ch} = d\eta|_{\eta=0} = 140$. Cocktail ρ (thin solid red line), unmodified ρ (dashed-dotted red line), in-medium broadening ρ (Chanfray *et al.*, 1996; Rapp *et al.*, 1997; Rapp and Wambach, 2000) (thick solid blue line), in-medium moving ρ related to (Brown and Rho, 1991, 2002; Li *et al.*, 1995) (dashed green line). The errors are purely statistical. The systematic errors of the continuum are about 25%. From Arnaldi *et al.* (2006); Damjanovic (2008).

as well as the level of D meson pair decays, the peripheral data could be fitted by the expected electromagnetic decays of the neutral mesons, i.e., the 2-body decays of the η , ρ , ω and ϕ resonances and the Dalitz decays of the η , η' and ω . In the more central cases, a fit procedure is ruled out due to the existence of a strong excess with a priori unknown characteristics.

The excess was therefore isolated by subtracting the measured decay cocktail, without the ρ , from the data, as shown in Fig. 45. The resultant distribution shows some non-trivial centrality dependence, but is largely

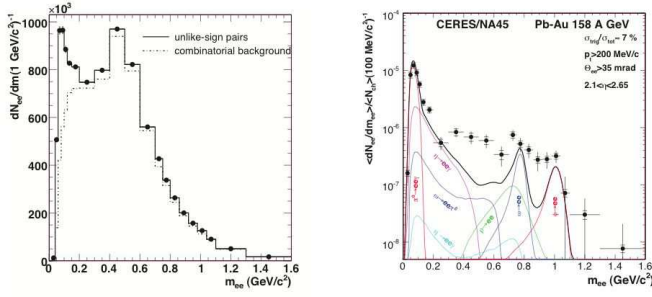


FIG. 47 (left) CERES unlike-sign pair yield (histogram) and combinatorial background (dashed curve). (right) Invariant e^+e^- mass spectrum compared to the expectation from hadronic decays (Adamová *et al.*, 2008).

consistent with a dominant contribution from $\rho \rightarrow \mu^+\mu^-$ annihilation. Fig. 46 shows a distribution obtained for semi-central collisions, compared with in-medium broadening (Rapp and Wambach, 2000) and mass-dropping (Brown and Rho, 2002) scenarios. The observed distribution (ρ spectral function) exhibits considerable broadening, but essentially no shift of the ρ -peak position.

CERES (NA45/2) (e^+e^-)

In preparation for the lead beam acceleration in the SPS, CERES upgraded the detector by adding a cylindrical time projection chamber (TPC) with a radial electric field (right half of Fig. 42). Among other things, this improved the mass resolution $\Delta m/m$ in the region of the ρ/ω from 9% to about 6% (Agakichiev *et al.*, 2005; Marín, 2004).

The dielectron distribution obtained in Pb-Au collisions at 158 AGeV before combinatorial subtraction, together with the normalized mixed-event background is shown in the left panel of Fig. 47. The background-subtracted distribution is compared with the hadronic cocktail in the right panel of Fig. 47. Here again, an enhancement over the cocktail is observed in the mass range $0.2 < m_{e^+e^-} < 1.1 \text{ GeV}/c^2$, the enhancement factor being 2.45 ± 0.21 (stat) ± 0.35 (syst) ± 0.45 (decays), where the last error is from the systematic uncertainty in the cocktail calculation.

Fig. 48 shows the dielectron yield after the hadronic-cocktail subtraction, compared with the mass dropping (left) and width broadening (right) assumptions. Although the error bars are larger than those in the NA60 spectra, the authors concluded that a substantial in-medium broadening of the ρ is favored over a density-dependent shift of the ρ pole mass.

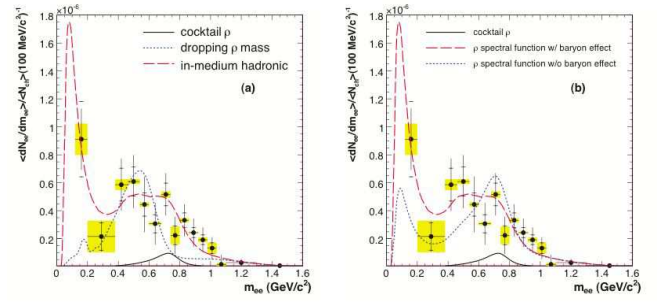


FIG. 48 CERES e^+e^- pair yield after subtraction of the hadronic cocktail. In addition to the statistical error bars, systematic errors of the data (horizontal ticks) and the systematic uncertainty of the subtracted cocktail (shaded boxes) are indicated. The broadening scenario (long-dashed line: (van Hees and Rapp, 2006; Rapp and Wambach, 2000)) is compared to a calculation assuming a density dependent dropping ρ mass (dotted line in (a): (Brown and Rho, 1991, 1996, 2002)) and to a broadening scenario excluding baryon effects (dotted line in (b)). From Adamová *et al.* (2008).

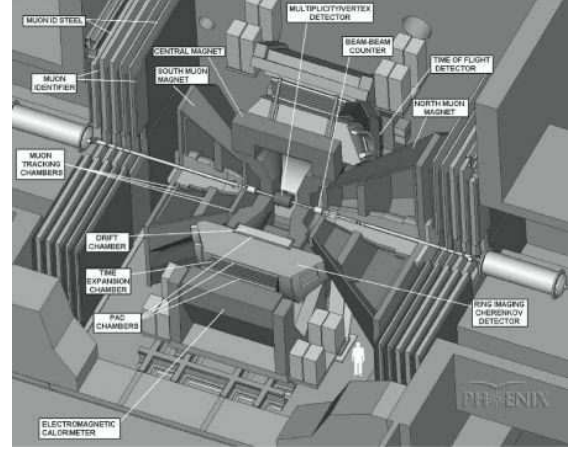


FIG. 49 The PHENIX experiment at RHIC (Adcox *et al.*, 2003).

3. RHIC ($\sqrt{s_{NN}} = 200 \text{ GeV}$)

At RHIC, the PHENIX experiment (Fig. 49) has been designed to measure dielectrons over a wide mass range. Electrons and positrons are reconstructed in the two central arm spectrometers using drift chambers, located outside an axial magnetic field. They are identified by hits in the ring imaging Čerenkov detector (RICH) and by matching the momentum with the energy measured in an electromagnetic calorimeter.

Fig. 50 shows a dielectron distribution observed by PHENIX in Au+Au minimum-bias collisions at $\sqrt{s_{NN}} = 200 \text{ GeV}$, after combinatorial background subtraction using the mixed event shape normalized to the like-sign pair yields (Afanasiev *et al.*, 2007). The dielectron yield in the minimum bias collisions, in the mass range between 150 and $750 \text{ MeV}/c^2$, is enhanced over the cocktail by

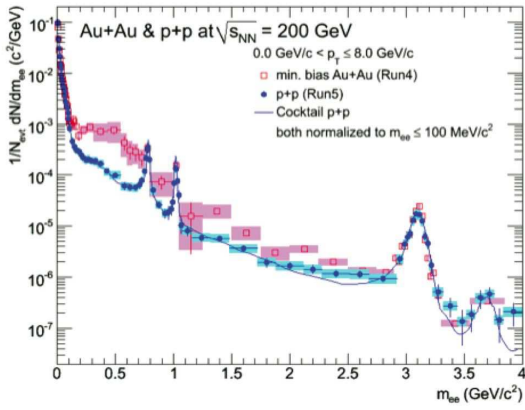


FIG. 50 Invariant e^+e^- pair yield observed by PHENIX in Au+Au minimum-bias and in $p+p$ collisions at $\sqrt{s_{NN}} = 200$ GeV. The curve is the hadronic cocktail for $p+p$. The $p+p$ spectrum and the cocktail curve were normalized to the Au+Au yield in the $m_{ee} < 100$ MeV/ c^2 region (Adare *et al.*, 2008; Afanasiev *et al.*, 2007; Toia, 2008).

a factor of $3.4 \pm 0.2(\text{stat.}) \pm 1.3(\text{syst.}) \pm 0.7(\text{model})$. A clear increase with centrality is also observed. No detailed analysis of the excess is available yet.

4. High energy heavy ion summary

An enhanced yield of dilepton pairs over the hadronic sources in the low-mass region has been observed, regardless of the bombarding energy.

At low beam energy of ~ 1 AGeV, the long-standing DLS puzzle (excess) has been confirmed by the recent HADES experiment. However, recent indications of C+C dielectron distribution agreeing with the $(pp+pn)/2$ distribution, if confirmed, may rule out the possibility of in-medium modification effects at this energy.

The two SPS experiments, CERES measuring dileptons and NA60 measuring dimuons, both established that there is a dilepton enhancement in the low-mass region. The excess here is consistent with $\pi^+\pi^- \rightarrow \rho \rightarrow l^+l^-$ with the ρ significantly broadened in the nuclear medium, while the data do not call for the simple ρ mass change.

At RHIC, the PHENIX experiment showed that there is a dilepton enhancement in the low-mass region, the magnitude of which increases faster with the centrality of the collisions than the number of participating nucleons, but the statistical errors are still fairly large in order to draw firm conclusions based on the data.

D. ρ , ω and ϕ mesons produced in nuclei with elementary reactions

1. TAGX at INS Electron Synchrotron

The TAGX experiment (Fig. 51) at the 1.3-GeV INS Electron Synchrotron (Institute for Nuclear Study, Tokyo

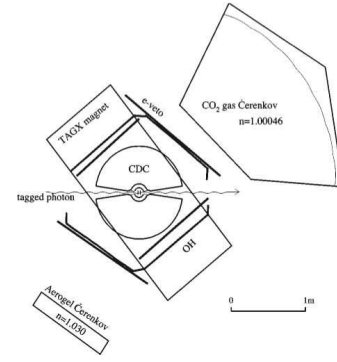


FIG. 51 A plan view of the TAGX spectrometer (Huber *et al.*, 2003).

University) used a tagged photon beam in the energy range of 600-1120 MeV to study the $\gamma A \rightarrow \pi^+\pi^-X$ reaction on $A = {}^2\text{H}$, ${}^3\text{He}$ and ${}^{12}\text{C}$ targets. This was a pioneering experiment which attempted to study in-medium modifications of ρ^0 with elementary reactions.

However, the claim of finding a ρ^0 mass shift of -160 ± 35 MeV/ c^2 in ${}^3\text{He}$ (Lolos *et al.*, 1998) was met with skepticism due to the inevitable pion rescattering effect even for light targets (the emitted pions being in the resonance region), the small target volume, and the much-larger-than-expected shift.

They later applied a helicity analysis to extract in-medium ρ_L^0 invariant mass distributions (Huber *et al.*, 2003), compared the spectra with various simulations (Post *et al.*, 2004; Rapp *et al.*, 1997; Saito *et al.*, 1997a), and obtained a smaller but still sizable mass shift of $-65 \sim -75$ MeV/ c^2 in the photon energy bin of $E_\gamma = 800 - 900$ MeV, and -45 MeV/ c^2 for $E_\gamma = 960 - 1120$ MeV. The ${}^{12}\text{C}$ distributions on the other hand, were found to be consistent with quasi-free ρ^0 production.

Why TAGX observed such a large effect only in ${}^3\text{He}$ is not yet understood, but in view of the fact that the $\gamma A \rightarrow e^+e^-X$ data of CLAS-g7 (section V.D.3) do not show any sign of ρ^0 mass shift, this is most likely unrelated to the ρ^0 in-medium modification.⁷

2. E325 experiment at KEK

The experiment E325 at the KEK 12 GeV Proton Synchrotron was the first to measure dileptons in search for the modification of the vector meson mass in a nucleus in elementary reactions. They measured the invariant mass spectra of e^+e^- pairs produced in 12 GeV proton-induced nuclear reactions. The setup is a two-arm spectrometer (Fig. 52), and was designed to measure the decays of

⁷ The incident photon energy range of TAGX was 0.6 – 1.12 GeV while it was 0.61 – 3.82 GeV in the CLAS-g7 experiment. Therefore, a more direct comparison would be to use low incident energy events of the CLAS-g7 data sample.

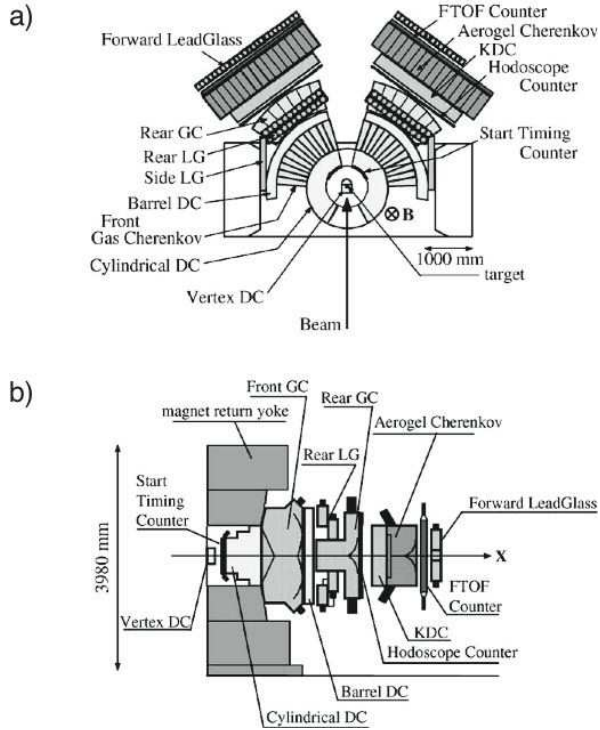


FIG. 52 Schematic view of the experimental setup of the E325 spectrometer: (a) the top view and (b) the side view. The side view shows the cross section along the center of the kaon arm (Ozawa *et al.*, 2001; Sekimoto *et al.*, 2004).

the vector mesons, $\phi \rightarrow e^+e^-$, $\rho/\omega \rightarrow e^+e^-$ as well as $\phi \rightarrow K^+K^-$.

For electron identification, two stages of electron-identification counters were used. The first was the front gas-Cherenkov counters (FGC). The second stage consisted of the rear gas-Cherenkov counters (RGC), the rear lead-glass electromagnetic (EM) calorimeters (RLG), the forward lead-glass EM calorimeters (FLG), and the side lead-glass EM calorimeters (SLG). The overall electron efficiency was 78% with a pion rejection power of 3×10^{-4} (Sekimoto *et al.*, 2004).

The mass resolution was estimated to be $8.0 \text{ MeV}/c^2$ and $10.7 \text{ MeV}/c^2$ for $\omega \rightarrow e^+e^-$ and $\phi \rightarrow e^+e^-$ decays, respectively.

The kinematical region covered was $0.5 < y < 2$ and $1 < \beta\gamma < 3$ for e^+e^- pairs (Fig. 53), where the decay probability inside the target nucleus was expected to be enhanced. Assuming that the meson decay widths are unmodified in nuclei, the coverage would correspond to the in-nucleus decay fractions shown in Table II.

The E325 invariant mass spectra for C and Cu targets are shown in Fig. 54. The data were taken with the “unlike-sign-double-arm” trigger condition, i.e., either a positron in the left arm and an electron in the right arm (LR event) or vice versa (RL event), to suppress the background from Dalitz decays and conversions, thereby precluding the possibility of normalizing the background to the like-sign pair distribution.

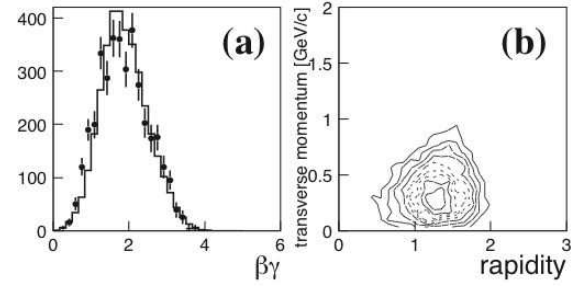


FIG. 53 Kinematical distributions of e^+e^- pairs in the ϕ mass region ($0.95 \rightarrow M_{e^+e^-} < 1.05 \text{ GeV}/c^2$) detected in the E325 spectrometer (points with error bars), together with the simulation result using the JAM nuclear cascade code (histogram, (Nara *et al.*, 1999)). (left) $\beta\gamma$ distribution. (right) Rapidity y vs pair transverse momentum p_T (Muto *et al.*, 2007).

TABLE II Expected in-nucleus decay fractions of vector mesons in the E325 kinematics, assuming that the meson decay widths are unmodified in nuclei, obtained by using a Monte Carlo-type model calculation (Muto *et al.*, 2007; Naruki *et al.*, 2006).

	C	Cu
ρ	46%	61%
ω	5%	9%
ϕ		6%*

* for slow ϕ mesons with $\beta\gamma < 1.25$.

The combinatorial background shape was obtained by the event-mixing method, and its normalization was obtained by fitting the data together with contributions from $\omega \rightarrow e^+e^-$, $\rho \rightarrow e^+e^-$, $\phi \rightarrow e^+e^-$, $\eta \rightarrow e^+e^-\gamma$ and $\omega \rightarrow e^+e^-\pi^0$. The relativistic Breit-Wigner distribution was used for the resonance shapes, and kinematical distributions of mesons were obtained by the nuclear cascade code JAM (Nara *et al.*, 1999), which is in good agreement with the experimental data (see, e.g., Fig. 53 (a)).

E325 results on the ρ/ω mesons

The striking features of the ρ/ω region of the E325 spectra are as follows. i) A significant excess can be seen on the low-mass side of the ω peak, which could not be fitted with the cocktail. Therefore, in the fit shown in Fig. 54, the range $0.6 < m_{e^+e^-} < 0.76 \text{ GeV}/c^2$ was excluded from the fit. ii) The ρ/ω ratio, which is known to be close to unity in pp collisions at this energy (Blobel *et al.*, 1974), is here $\rho/\omega < 0.15$ and < 0.31 for C and Cu targets, respectively (95% C.L.).

The disappearance of ρ and the appearance of the excess may be due to the in-medium dropping of the ρ

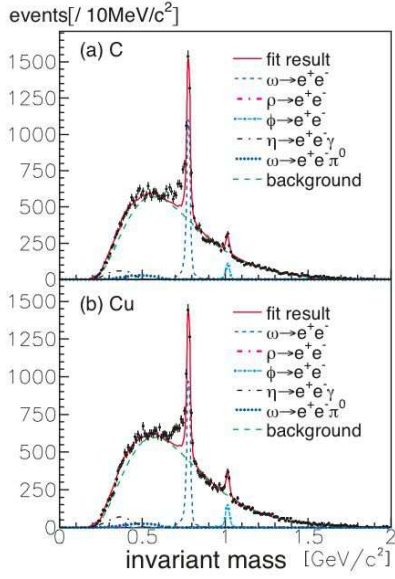


FIG. 54 Invariant mass spectra of e^+e^- for the (a) C and (b) Cu targets. The solid lines are the best-fit results, which is the sum of the known hadronic decays, $\omega \rightarrow e^+e^-$ (dashed line), $\phi \rightarrow e^+e^-$ (thick dash-dotted line), $\eta \rightarrow e^+e^-\gamma$ (dash-dotted line), and $\omega \rightarrow e^+e^-\pi^0$ (dotted line) together with the combinatorial background (long-dashed line). $\rho \rightarrow e^+e^-$ is not visible (Naruki *et al.*, 2006).

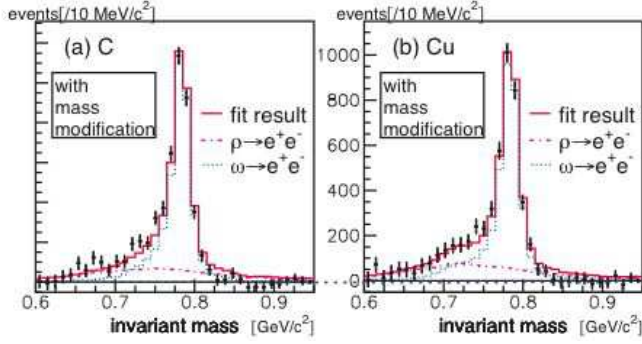


FIG. 55 Invariant mass spectra of e^+e^- . The combinatorial background and the shapes of $\eta \rightarrow e^+e^-\gamma$ and $\omega \rightarrow e^+e^-\pi^0$ were subtracted. The result of the model calculation considering the in-medium modification for the (a) C and (b) Cu targets. The solid lines show the best-fit results. In (a) and (b), the shapes of $\omega \rightarrow e^+e^-$ (dotted line) and $\rho \rightarrow e^+e^-$ (dash-dotted line) were modified according to the model using the formula $m_V(\rho)/m_V(0) = 1 - k(\rho/\rho_0)$ with $k = 0.092$ (Naruki *et al.*, 2006).

mass⁸, which would take away the strength from the normal ρ and put them in the excess region. This assumption

⁸ Alternatively, this may be due to the over-subtraction of the background component, as pointed out by the J-Lab CLAS g7 collaboration, whose results are in conflict with those of KEK E325. See Section V.D.3.

was tested by fitting the background-subtracted spectra using a Monte Carlo-type model including the mass-dropping model,

$$m_V(\rho)/m_V(0) = 1 - k(\rho/\rho_0). \quad (\text{V.81})$$

The vector mesons were generated on the surface of an incident hemisphere of the target (supported by the $A^{2/3}$ dependence of the ω production cross section (Tabaru *et al.*, 2006)), propagated through the nucleus which was modeled by a Woods-Saxon density distribution. The parameter k was common for ω and ρ as well as for C and Cu targets. The ρ/ω ratio was also allowed to vary.

The best fit results are, $k = 0.092 \pm 0.002$ and a ρ/ω ratio of 0.7 ± 0.1 and 0.9 ± 0.2 respectively, for C and Cu targets. The best-fit curves are superimposed on the background-subtracted spectra shown in Fig. 55. They also examined whether or not the $\rho - \omega$ interference can account for the observed shoulder, but found that the interference cannot explain the data even though the ρ/ω ratio and the mixing angle were scanned over a wide range.

So, for the ρ/ω region, E325 concluded that both ρ and ω masses are shifted by 9% at the normal nuclear density. Fits with density-proportional width broadening did not fit the data; the fit results favored the zero-broadening case (Naruki *et al.*, 2006). This is in conflict with the J-Lab CLAS g7 result discussed in V.D.3.

E325 results on the ϕ meson

Due to the long lifetime of the ϕ meson, in-medium modification effects, if any, are expected only for the slow-moving mesons which have a chance to decay inside the target nucleus. E325 therefore divided the data in three parts based on the $\beta\gamma$ values of the observed e^+e^- pairs, $\beta\gamma < 1.25$, $1.25 < \beta\gamma < 1.75$ and $1.75 < \beta\gamma$ (see Fig. 53).

The $\beta\gamma$ -selected spectra are shown in Fig. 56, together with fit results. The ϕ was assumed to have in-vacuum mass and width, convoluted over the detector response in the simulation according to the JAM-generated kinematical distributions of the ϕ meson in each $\beta\gamma$ region. A quadratic background was added to the simulated peak, and the background parameters and the ϕ abundance were obtained from the fit.

The fits are satisfactory, except for the $\beta\gamma < 1.25$ region of Cu data, in which a large excess of $N_{\text{excess}}/(N_{\text{excess}} + N_\phi) = 22\%$ was found. If this excess is to be ascribed to the in-medium ϕ modification, not only the mass but also the width need to be varied, since the JAM-based simulation indicates only 6% of the ϕ meson produced in copper nuclei with $\beta\gamma < 1.25$ would decay in the target nucleus if broadening is not introduced (see Tab. II).

It was thus attempted to fit the data by introducing both the density-linear mass shift

$$m_\phi(\rho)/m_\phi(0) = 1 - k_1(\rho/\rho_0)$$

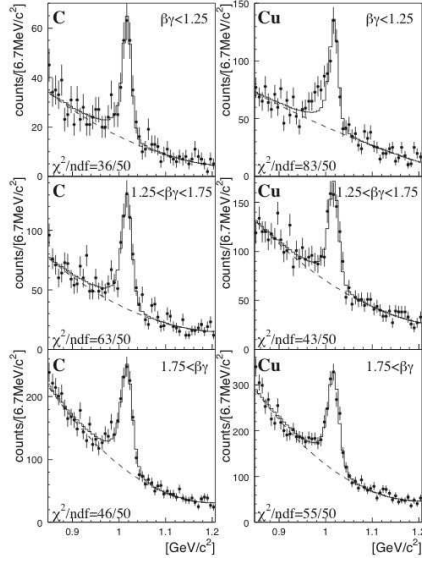


FIG. 56 Obtained e^+e^- distributions with the fit results. The target and $\beta\gamma$ region are shown in each panel. The points with error bars represent the data. The solid lines represent the fit results with an expected $\phi \rightarrow e^+e^-$ shape and a quadratic background. The dashed lines represent the background (Muto *et al.*, 2007).

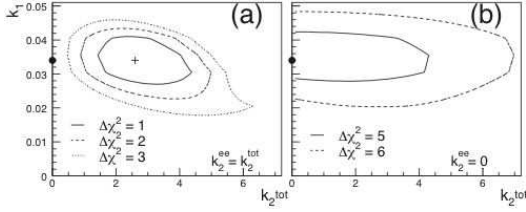


FIG. 57 Confidence ellipsoids for the modification parameters k_1 and k_2^{tot} in cases (i) in (a) and (ii) in (b). The values of $\Delta\chi^2$ s in both panels are the differences from the χ^2_{min} ($= 316.4$) at the best-fit point in case (i) which is shown by the cross in the panel (a). The best-fit point in case (ii) is shown by the closed circle in the panel (b), and also in (a) since the ordinates are common to both cases in parameter space (Muto *et al.*, 2007).

and the density-linear width broadenings

$$\Gamma_{\phi}^{\text{tot}}(\rho)/\Gamma_{\phi}^{\text{tot}}(0) = 1 + k_2^{\text{tot}}(\rho/\rho_0), \text{ and}$$

$$\Gamma_{\phi}^{ee}(\rho)/\Gamma_{\phi}^{ee}(0) = 1 + k_2^{ee}(\rho/\rho_0),$$

where $\Gamma_{\phi}^{\text{tot}}$ is the total width and Γ_{ϕ}^{ee} is the e^+e^- partial-decay width.

Figure 57 shows the fit result for the two cases examined, (a) $k_2^{ee} = k_2^{\text{tot}}$ (i.e., the branching ratio $\Gamma_{\phi}^{ee}/\Gamma_{\phi}^{\text{tot}}$ remains unchanged in the medium), and (b) $k_2^{ee} = 0$ (i.e., $\Gamma_{\phi}^{\text{tot}}$ increases but Γ_{ϕ}^{ee} does not increase in the medium).

The fit favors the former case. The obtained values are $k_1 = 0.034_{-0.007}^{+0.006}$ and $k_2^{\text{tot}} = k_2^{ee} = 2.6_{-1.2}^{+1.8}$, indicating the in-medium ϕ -meson mass shift of 3.4% and width

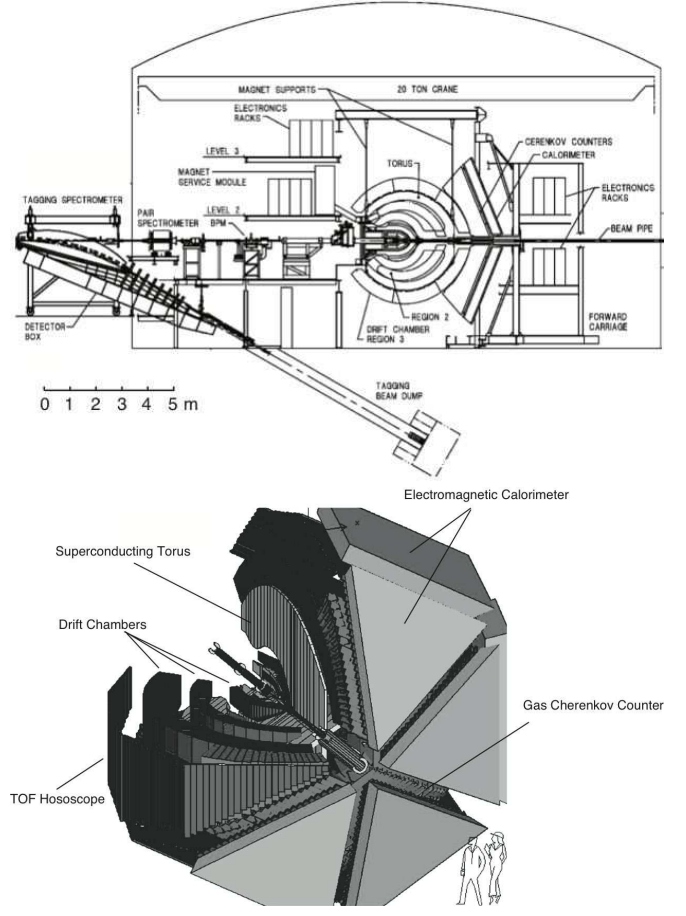


FIG. 58 (top) Side view of the CLAS detector in Hall B of J-Lab, with the photon-tagging system. (bottom) CLAS cut-away view (Mecking *et al.*, 2003).

increase of a factor of 3.6 ($\Gamma_{\phi}^{\text{tot}} \simeq 15\text{MeV}/c^2$) at normal nuclear density.

3. J-Lab E01-112 (g7) experiment

J-Lab E01-112, better known as the CLAS experiment g7, was conducted in Hall-B of Jefferson Laboratory (Fig. 58). An electron beam accelerated by the Continuous Electron Beam Accelerator Facility (CEBAF) was used to produce a tagged photon beam having an energy range of 0.61 – 3.82 GeV.

The CEBAF Large Acceptance Spectrometer (CLAS) is a nearly 4π -detector based on a six-coil superconducting toroidal magnet, and was designed to track charged particles with momenta greater than 200 MeV/c over the polar angle range from 8° to 142° , while covering up to 80% of the azimuth. The CLAS detector is divided into six identical spectrometers (sectors), each made of three regions of drift chambers (DC), time-of-flight scintillators, Čerenkov counters (CC) and electromagnetic calorimeters (EC) (Fig. 58 bottom). The target materials were liquid deuterium (LD_2), carbon, titanium, iron,

TABLE III Mass and width of the ρ meson obtained by the CLAS-g7 collaboration from the simultaneous fits to the mass spectra for each target and the ratio to ${}^2\text{H}$.

Target	M_ρ	Γ_ρ
${}^2\text{H}$	773.0 ± 3.2	185.2 ± 8.6
C	726.5 ± 3.7	176.4 ± 9.5
Fe, Ti	779.0 ± 5.7	217.7 ± 14.5

and lead (simultaneously in the beam). To reduce the low-energy e^- and e^+ background from pair production in the targets, a “mini-torus” magnet was situated just beyond the target region and inside the DC.

The e^+e^- event selection and the rejection of the very large $\pi^+\pi^-$ background were done through cuts on the EC and the CC. The pion rejection factor was 5.4×10^{-4} per track, or 2.8×10^{-7} for the pair. The pair-mass resolution was $10 \text{ MeV}/c^2$ for the ϕ peak. The pair momenta of $\sim 0.8 \sim 1.8 \text{ GeV}/c$ were accepted, similar to the KEK E325 acceptance (Djalali, 2008).

In reconstructing the e^+e^- pairs, the two leptons were required to be detected in different sectors of the CLAS detector. This requirement removed the large background due to pair-production, Bethe-Heitler processes, and π^0 and η Dalitz decays that have a small opening angle.

The combinatorial background⁹ was approximated by an event-mixing technique, and was normalized to the number of expected opposite-charge pairs, calculated from the number of observed like-sign pairs using Eq.(V.80). The spectra shown in Fig. 59 (left) are the reconstructed e^+e^- distributions, compared with the normalized combinatorial background (Wood *et al.*, 2008). The uncertainty of the normalization was estimated at $\pm 7\%$.

Monte Carlo calculations using a code based on a semi-classical BUU transport model were used to fit the background-subtracted spectra (Fig. 59, right). In the model, the particles produced as a result of the γN reaction in the target nucleus were propagated through the nucleus allowing for final-state interactions (Effenberger *et al.*, 1999). The acceptance-corrected BUU mass shapes for the ρ , ω and ϕ mesons were scaled separately to match the experimental mass spectra. A substantial contribution from the ρ meson was found (dot-dashed curves in Fig. 59, right) unlike in the KEK E325 analysis.

As the probabilities of the ω and ϕ mesons decaying inside the nucleus are low, the simulated ω and ϕ mass shapes were subtracted from the data, to obtain the ρ

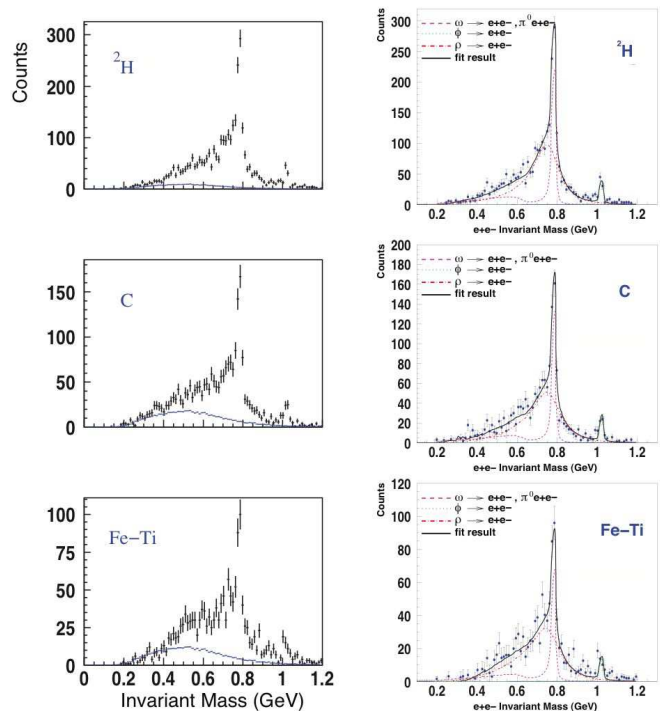


FIG. 59 (left) Normalized combinatorial background for individual targets compared with the data. (right) Result of the fits to the e^+e^- invariant mass spectrum obtained for the ${}^2\text{H}$ (top), C (middle), and Fe-Ti (bottom) data (Wood *et al.*, 2008). The curves on the right panels are Monte-Carlo calculations by the BUU model for various vector meson decay channels (Effenberger *et al.*, 1999; Effenberger and Mosel, 2000).

mass spectra. The results are shown in Fig. 60. The curves therein are Breit-Wigner/ μ^3 fits (μ being the invariant mass). Here, the μ^3 factor comes from the mass dependence of the $\Gamma_{e^+e^-}(\mu)/\Gamma_{\text{tot}}(\mu)$ ratio; $\Gamma_{e^+e^-}(\mu) \propto 1/\mu^4$ and $\Gamma_{\text{tot}}(\mu) \propto \mu$.

The mass and width of the ρ meson in various targets were obtained by performing a simultaneous fit to the mass spectra and the ratio of each spectrum to the ${}^2\text{H}$ data (so as to impose more constraints on the fits), and the fit results are shown in Table III. These are consistent with collisional broadening without mass modification.

The mass shift coefficient k as defined in Eq.(V.81) was obtained by analyzing the ratio of the Fe-Ti to the ${}^2\text{H}$ distributions to be 0.02 ± 0.02 , which corresponds to an upper limit of $k = 0.053$ with a 95% confidence level. These results are quite different from those obtained by the KEK E325 experiment.

4. CBELSA/TAPS experiment

The CBELSA/TAPS collaboration at the electron stretcher accelerator (ELSA) in Bonn used the $\gamma A \rightarrow \pi^0 \gamma X$ reaction to study the ω meson in-medium behavior using the Crystal Barrel (CB) and TAPS crystal spec-

⁹ In the CLAS g7 experiment, the probability of an untagged photon and a tagged photon being in the same radio-frequency timing bunch was about 25%. This contributed to the combinatorics, in addition to the usual case of picking up a wrong lepton produced in the same event.

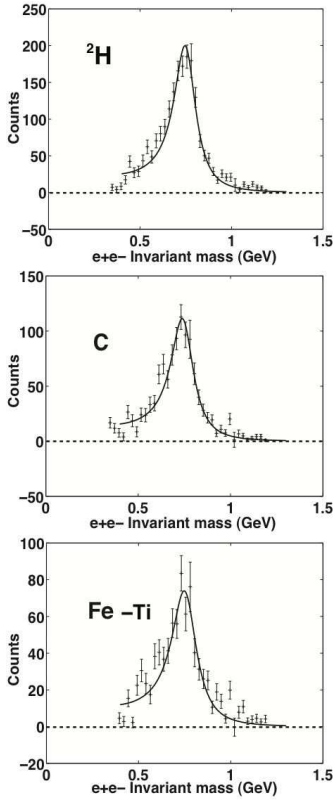


FIG. 60 Individual Breit-Wigner/ μ^3 fits to the ρ mass spectra (background and ω , ϕ contributions subtracted) (Wood *et al.*, 2008).

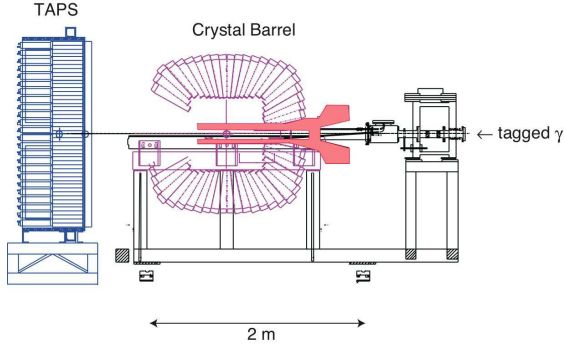


FIG. 61 Side view of the Crystal Barrel (CB) and TAPS detector combination.

trometers shown in Fig. 61. Tagged photons in the energy range of 0.64–2.53 GeV were incident on targets (Nb and LH_2) mounted in the center of the CB, a photon calorimeter consisting of 1290 CsI(Tl) crystals with an angular coverage of 30° to 168° in the polar angle and a complete azimuthal angle coverage. Reaction products emitted in forward direction were detected in the TAPS detector, which consisted of 528 hexagonally shaped BaF_2 detectors covering polar angles between 4° and 30° and the complete 2π azimuthal angle. The resulting geometrical solid angle coverage of the combined system was 99% of

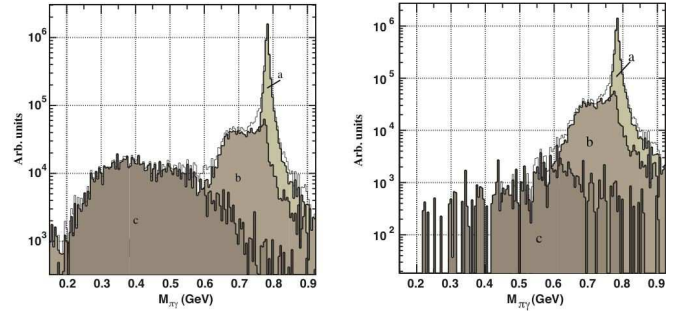


FIG. 62 (left) The $\pi^0\gamma$ mass distribution obtained from a Monte Carlo simulation of the process $\gamma + \text{Nb} \rightarrow \pi^0\gamma + X$ at $E_\gamma = 1.2$ GeV. The spectrum is decomposed into different contributions corresponding to the fraction of ω -mesons decaying outside the nucleus (a), the fraction of ω -mesons decaying inside for which the π^0 does not rescatter (b), and the fraction of ω -mesons decaying inside the nucleus for which π^0 rescatters (c). In the simulation a drop of the ω mass by 16% at normal nuclear density was assumed. (right) The same as the left panel, with the additional condition of $T_{\pi^0} > 150$ MeV (Messchendorp *et al.*, 2001).

4π . Charged particles were identified with a scintillating fiber detector placed inside the CB, and a plastic scintillator mounted in front of each TAPS crystal (Aker *et al.*, 1992; Janssen *et al.*, 2000; Novotny, 1991).

The $\omega \rightarrow \pi^0\gamma$ decay mode has a large branching ratio of 8.9% and is a clean and exclusive mode to study the ω in-medium properties since the $\rho \rightarrow \pi^0\gamma$ branching ratio is only 6.0×10^{-4} (see Table I). Therefore, the study of this mode is complementary to the dilepton decays (Sibirtsev *et al.*, 2000). A serious disadvantage are possible strong final-stage interactions of the π^0 meson within the nucleus. Monte Carlo simulations (Messchendorp *et al.*, 2001) show that the rescattering effect is small in the mass range of interest, and can be further reduced by removing low-energy pions ($T_\pi < 150$ MeV), as depicted in Fig. 62.

The $\pi^0\gamma$ events are reconstructed from three photons, and the invariant mass spectra are shown in the left panel of Fig. 63. Here, in order to maximize the in-nucleus decay probability, slow-moving ω mesons with $|\mathbf{p}_\omega| < 0.5 \text{ GeV}/c$ were selected. The large continuum background is due to four-photon decays of $\pi^0\pi^0$ and $\pi^0\eta$ where one of the four photons is missed. A smooth polynomial background was assumed and was subtracted, and the resultant LH_2 and Nb data are compared in the right panel. As shown, a shoulder on the low-mass side of the ω peak was found on the Nb target. This was taken as evidence for an ω in-medium mass reduction by 60_{-35}^{+10} MeV at an average nuclear density of $0.6\rho_0$, or in terms of the mass shift coefficient k as defined in Eq.(V.81), this gives $k \simeq 0.14$. The width was found to be $\Gamma = 55 \text{ MeV}/c^2$, dominated by the experimental resolution.

The background-subtraction procedure was criticized by Kaskulov *et al.* (2007), who pointed out *if* the same background shape is used both for LH_2 and

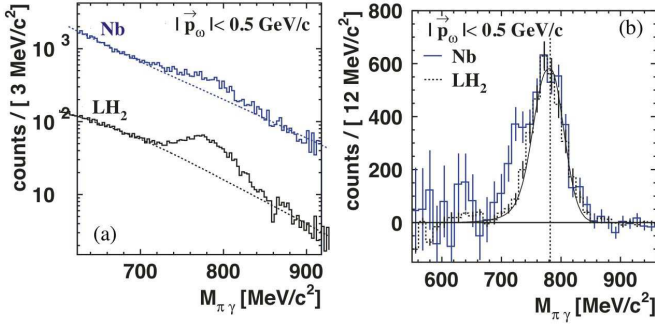


FIG. 63 (a) Inclusive $\pi^0\gamma$ invariant mass spectra for momenta less than 500 MeV/c. Upper histogram: Nb data, lower histogram: LH₂ target reference measurement. The dashed lines indicate fits for the respective background. (b) $\pi^0\gamma$ invariant mass for the Nb data (solid histogram) and LH₂ data (dashed histogram) after background subtraction. The error bars show statistical uncertainties only. The solid curve represents the simulated line shape for the LH₂ target (Trnka *et al.*, 2005).

Nb, the shoulder structure would disappear. The CBELSA/TAPS group pointed out that the experimental data clearly show that the background distributions are different and hence it is not justified to *assume* the same background shape (Metag, 2008a). However, the fact that slightly different background assumptions lead to a complete different conclusion on the ω mass shift is quite alarming.

The CBELSA/TAPS group has therefore started to employ the event-mixing technique to generate the background distribution, instead of using a polynomial function. Preliminary results were presented in (Metag, 2008a), but these were later found to contain some problems, and are being further investigated (Metag, 2008b). Therefore, until the reanalysis is finalized by the group, the ω mass shift reported in (Trnka *et al.*, 2005) cannot be regarded as a conclusive evidence for the in-medium ω modification.

E. Vector-meson in-medium width from transparency-ratio measurements

Instead of obtaining the in-medium meson width from fits to the observed invariant-mass peak, an alternative method of using the transparency ratio T , defined as

$$T = \frac{\sigma_{\gamma A \rightarrow VX}}{A\sigma_{\gamma N \rightarrow VX}}, \quad (\text{V.82})$$

was proposed (Hernández and Oset, 1992; Kaskulov *et al.*, 2007; Mühlich and Mosel, 2006), and has been used to extract ϕ (Ishikawa *et al.*, 2005) and ω (Kotulla *et al.*, 2008) in-medium widths. Here, $\sigma_{\gamma A \rightarrow VX}$ is the inclusive nuclear vector-meson (V) photo-production cross section and $\sigma_{\gamma N \rightarrow VX}$ is the cross section on a free nucleon. The ratio T is a measure

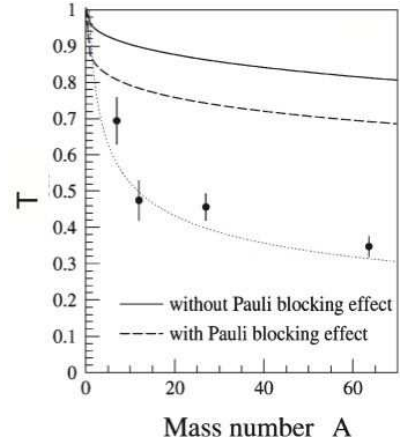


FIG. 64 Mass number (A) dependence of the transparency ratio T . The dotted line corresponds to $\sigma_A \propto A^{0.72}$. The solid and dashed curves show the theoretical calculation (Cabrera *et al.*, 2004) without (solid curve) and with (dashed curve) Pauli-blocking correction for the ϕ meson scattering angle in the laboratory frame of 0° (Ishikawa *et al.*, 2005).

for the loss of vector-meson flux via inelastic processes in nuclei, and is related to the absorptive part of the meson-nucleus potential.

This is conceptually a simple measurement, but extracting the in-medium meson width from the A dependence of the ratio T requires comparison with theory calculations.

The ϕ attenuation

The photo-production of ϕ mesons from Li, C, Al and Cu targets was measured at $E_\gamma = 1.5 - 2.4$ GeV, using the laser-electron photon facility at SPring-8 (LEPS), in the $\gamma A \rightarrow K^+ K^- X$ channel (Ishikawa *et al.*, 2005). The A dependence of the incoherent ϕ photo production cross section was found to be $\sigma_A \propto A^{0.72 \pm 0.07}$ (or $T = A^{-0.28}$, as shown in Fig. 64). Using a Glauber-type model calculation, the in-medium ϕ -nucleon cross section was deduced to be $\sigma_{\phi N} = 35^{+17}_{-11}$ mb, which is much larger than the free-space value of $\sigma_{\phi N}^{\text{free}} = 140 \mu\text{b}$ used as an input to the model calculation (Amsler *et al.*, 2008). Theoretical calculations (Cabrera *et al.*, 2004) predicted much larger T values (solid and dashed curves in Fig. 64).

Using the classical low-density relation

$$\Gamma_V = \hbar\rho\beta c\sigma, \quad (\text{V.83})$$

this would correspond to a width of $\Gamma_\phi \simeq 80$ MeV/ c^2 at $\rho = \rho_0$ and $\beta \simeq 0.7$ (i.e., $\beta\gamma \simeq 1$), where the KEK E325 experiment reported a much smaller in-medium ϕ width of 15 MeV/ c^2 (see section V.D.2)¹⁰.

¹⁰ This discrepancy may at least partly be due to the way the trans-

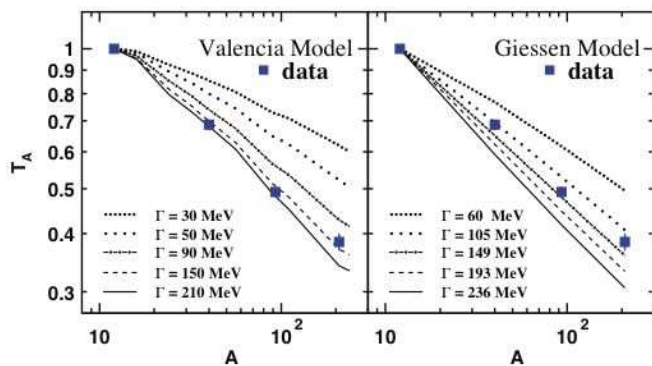


FIG. 65 Experimentally determined transparency ratio normalized to the carbon data in comparison with a theoretical Monte Carlo simulation (Kaskulov *et al.*, 2007) (left) and a BUU calculation (Muehlich *et al.*, 2004) (right) varying the width at 1.1 GeV/c momentum, respectively. The width is given in the nuclear rest frame. Only statistical errors are shown (Kotulla *et al.*, 2008).

The ω attenuation

The CBELS/TAPS collaboration measured the A dependence of the ω photoproduction cross section on the nuclei C, Ca, Nb and Pb. The average momenta of the mesons was 1.1 GeV/c, so that almost all ω mesons decay outside the nuclear target. Since the ω photoproduction cross section on the neutron is not known, they took the transparency ratio normalized to the carbon data, as shown in Fig. 65.¹¹

The data were then compared with three different types of models, i) a Glauber model similar to the LEPS analysis, ii) a BUU analysis (Muehlich *et al.*, 2004) and iii) a calculation by the Valencia group (Kaskulov *et al.*, 2007). In all cases, the inelastic ω width was found to be 130 – 150 MeV/c² at $\rho = \rho_0$ for an average ω momentum of 1.1 GeV/c, or in terms of ωN cross section, $\sigma_{\omega N} \simeq 70$ mb.

VI. CONCLUDING REMARKS

The QCD vacuum shows the dynamical breaking of chiral symmetry. In the hot/dense QCD medium, the chiral order parameter such as $\langle \bar{q}q \rangle$ (chiral condensate) is expected to change as a function of temperature T and

density ρ of the medium, and its experimental detection is one of the main challenges in modern hadron physics.

Pion

Theoretically, all hadrons receive various spectral changes due to their strong interaction with the medium. Among those, the in-medium modification of the pion decay constant $f_\pi^t(\rho)$ and $f_\pi^t(T)$ is theoretically well understood at low T and ρ , and have close relation to the in-medium change of the chiral condensate (II.42,II.43). The predicted reduction at low density, $\langle \bar{q}q \rangle_\rho / \langle \bar{q}q \rangle_0 \simeq 1 - (0.3 \sim 0.4)\rho/\rho_0$, has now been experimentally demonstrated by comparing the isovector pion-nucleon b_1 and pion-nucleus $b_1(\rho)$ scattering lengths derived from pionic hydrogen and deeply-bound pionic Sn atoms, respectively, as well as by analyzing the differential cross sections for low-energy π^\pm elastic scattering by several nuclei.

σ meson

One of the interesting signals associated with the in-medium chiral restoration would be the spectral enhancement on the σ channel near the 2π threshold. Intriguing experimental results of “softening” of the $(\pi\pi)_{I=J=0}$ distribution (i.e., shift of the peak position to lower masses) have been obtained. These agree fairly well with (i) in-medium modifications of the $\pi\pi$ interaction, as well as with (ii) rescattering of outgoing pions with the nucleons without in-medium $\pi\pi$ interaction. In fact, the results of two calculations, Roca *et al.* (2002) and Buss *et al.* (2006), predict very similar spectra, as shown in Fig. 35. However, as long as the rescattering scenario can reproduce most of the observed “softening” trend, we cannot yet extract the predicted partial chiral restoration signature from the $\pi\pi$ spectra. New high-statistics data taken on C, Ca, Pb with the Crystal Ball/TAPS detector, which is being analyzed, may help shed some light on this problem (Metag, 2008b).

Vector mesons

Significant experimental work has been done to detect the possible in-medium “mass shift” of vector mesons, both using heavy-ion collisions and using elementary-particle beams. In general, the vector spectral function receives a shift of the peak, broadening, new structures, etc., due to the complex interaction of the vector current with the medium. Also, such a spectral shift may well depend on the spatial momentum of the current. Therefore, it would not be appropriate to oversimplify the problem to “mass shift vs. width broadening”. With this caution in mind, we list experimental results on the in-medium mass and width of the ρ , ω and ϕ mesons produced with

parency ratio was normalized to the production cross section on the nucleon in Fig. 64). While the γp cross section is sufficiently well known, the γn cross section is not. This was partly avoided in Ishikawa *et al.* (2005) by taking ${}^7\text{Li}$ as a reference.

¹¹ For this reason, the ratio shown in Fig. 65 is named T_A instead of T . This leads to different values of the transparency ratio since the transparency loss in C is normalized away. This normalization takes into account ω production processes on two nucleons which may be relevant in nuclei.

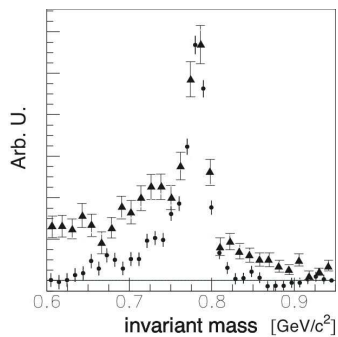


FIG. 66 Comparison of the dielectron invariant-mass spectrum (carbon target) of E325 (circles) and CLAS g7 (triangles).

elementary reactions, measured in different experiments in Table IV. The TAGX results are not included here for the reasons discussed in section V.D.1. The ω mass shift from CBELSA/TAPS is listed in the table, but it may change after the ongoing reanalysis, and hence we do not include this in the summary discussion.

Upon examining this table, we realize that there are some inconsistencies, and we discuss the two most pressing issues below.

(i) E325 and g7 disagree on the $\rho(\omega)$ mass shift: The E325 result is both ρ and ω masses get reduced at ρ_0 by 9% (the mass shift parameter $k = 0.092 \pm 0.002$), while the CLAS g7 placed a 95% confidence upper limit at $k = 0.053$. The comparison of the background-subtracted dielectron distributions (carbon target) measured by the two experiments (Fig. 66) shows that the two spectra are very different¹².

Wood *et al.* (2008) pointed out that this difference must be due to the way the combinatorial background was subtracted in E325. In the E325 analysis, due to the lack of a sample of same-charged leptons by which to extract the normalization of the combinatorial background, the background contribution was fit along with the ω - and ϕ -meson shapes. Without an absolute determination of the combinatorial background, the ρ -meson signal was suppressed and included in the background shape. Indeed, if the background normalization was free to vary in the CLAS-g7 fit, the g7 spectra were found to be consistent with $k \approx 0.16$ (Djalali, 2006)¹³.

(ii) E325 and CBELSA/TAPS disagree on the ω width: While an ω width broadening was not observed by the E325 experiment, CBELSA/TAPS found an

unexpectedly large in-medium broadening. These two observations are mutually inconsistent. Even though the extraction of the in-medium width depends on theory, the observed A -dependent reduction of the transparency ratio T clearly shows that the ω meson is attenuated in the target nucleus. This conclusion must be robust.

Table IV clearly shows that experimental results have not yet converged, and more work is needed to obtain consistent understanding of the in-medium behavior of vector mesons. In view of the robustness of the method, the in-medium broadening of vector mesons deduced from the transparency-ratio measurements are hard to rule out. On the other hand, problem(s) have been pointed out for all experiments which observed in-medium mass shifts, and hence those results must be treated with caution and further studies are needed.

ACKNOWLEDGMENTS

This article is based on a talk given by RH at the International Nuclear Physics Conference held in Tokyo (INPC 2007). During its preparation, the authors have benefited from the assistance of so many of their colleagues that it would be impossible to mention them all by name. However, we should like to acknowledge the specific contributions of Y. Akaishi, C. Djalali, H. En'yo, D. Gotta, D. Jido, V. Metag, U. Mosel, M. Naruki, E. Oset, K. Ozawa, P. Salabura, and S. Schadmand. It is a pleasure to acknowledge, too, the many insightful discussions at various times with S. Hirenzaki, P. Kienle, T. Kunihiro, H. Toki, and T. Yamazaki.

This work is supported in part by Grant-in-Aid for Specially Promoted Research (20002003), Grant-in-Aid for Scientific Research (C) (18540253), and the Global COE Program “the Physical Sciences Frontier”, MEXT, Japan.

REFERENCES

- Aarts, G., C. Allton, M. B. Oktay, M. Peardon, and J.-I. Skullerud, 2007, Phys. Rev. **D76**, 094513.
- Adamová, D., *et al.* (CERES Collaboration), 2008, Physics Letters B **666**, 425.
- Adare, A., *et al.* (PHENIX Collaboration), 2008, eprint 0802.0050.
- Adcox, K., *et al.* (PHENIX Collaboration), 2003, Nucl. Instr. and Meth. A **499**, 469.
- Afanasyev, S., *et al.* (PHENIX Collaboration), 2007, eprint 0706.3034.
- Agakichiev, G., M. Appenheimer, R. Averbek, F. Ballester, R. Baur, A. Benschede, J. Diaz, A. Drees, U. Faschingbauer, J. L. Ferrero, P. Fischer, Z. Fraenkel, *et al.*, 1998, The European Physical Journal C **4**, 231.
- Agakichiev, G., R. Baur, A. Breskin, R. Chechik, A. Drees, C. Jacob, U. Faschingbauer, P. Fischer, Z. Fraenkel, C. Fuchs, *et al.*, 1995, Physical Review Letters **75**, 1272.

¹² Note that the ρ/ω ratio in the pp collisions at the KEK energy is about unity (Blobel *et al.*, 1974), while that in the γp collisions at the CLAS energy is about 3 to 1 (Barth *et al.*, 2003; Erbe *et al.*, 1968; Wu *et al.*, 2005), which may account for the bulk of the difference found in Fig. 66.

¹³ In reality, there is no such freedom in the g7 background normalization. This was done just for the sake of g7-E325 comparison.

TABLE IV Compilation of experimental results on the in-medium mass and width of the ρ , ω and ϕ mesons produced with elementary reactions, measured in different experiments. This is based on and updating the table prepared by Metag (2008a)

	Invariant mass			Attenuation	
	E325 @ KEK	CLAS g7 @ Jlab	CBELSA/TAPS		LEPS @ SPring-8
Reaction	pA 12 GeV	γ A 0.6 – 3.8 GeV	γ A 0.7 – 2.5 GeV		γ A 1.5 – 2.5 GeV
Momentum	$p > 0.5$ GeV/c	$p > 0.8$ GeV/c	$p < 0.5$ GeV/c	$0.4 < p < 1.7$ GeV/c	$1.1 < p < 2.2$ GeV/c
ρ	\uparrow $\Delta m(\rho_0)/m = -9\%$	$\Delta m \approx 0$ some broadening	–	–	–
ω	\downarrow no broadening	–	$\Delta m(\rho_0)/m = -14\%^\dagger$	$\Gamma_\omega(\rho_0) = 130-150$ MeV/c ² $\rightarrow \sigma_{\omega N} \approx 70$ mb	–
ϕ	$\Delta m(\rho_0)/m = -3.4\%$ $\Gamma_\phi(\rho_0) \approx 15$ MeV/c ²	–	–	–	$\sigma_{\phi N} = 35$ mb $\rightarrow \Gamma_\phi(\rho_0) \approx 80$ MeV/c ²

\dagger This may change as a result of the ongoing reanalysis (Metag, 2008b).

- Agakichiev, G., *et al.*, 2005, The European Physical Journal C **41**, 475.
- Agakishiev, G., C. Agodi, H. Alvarez-Pol, A. Balanda, R. Bassini, G. Bellia, D. Belver, A. Belyaev, A. Blanco, M. Böhmer, A. Bortolotti, J. L. Boyard, *et al.*, 2008, Physics Letters B **663**, 43.
- Aker, E., C. Amsler, I. Augustin, C. Baker, B. Barnett, C. Batty, R. Beckmann, P. Birien, J. Bistirlich, P. Blüm, *et al.*, 1992, Nucl. Instr. and Meth. A **321**, 69.
- Alam, J., S. Sarkar, P. Roy, T. Hatsuda, and B. Sinha, 2001, Annals Phys. **286**, 159.
- Amsler, C., *et al.* (The Particle Data Group), 2008, Physics Letters B **667**, 1.
- Angelis, A. L. S., *et al.* (Helios/3 Collaboration), 2000, The European Physical Journal C **13**, 433.
- Anthony, I., J. D. Kellie, S. J. Hall, G. J. Miller, and J. Ahrens, 1991, Nucl. Instr. and Meth. A **301**, 230.
- Aoki, S., *et al.* (PACS-CS Coll.), 2008, eprint 0807.1661.
- Aouissat, Z., R. Rapp, G. Chanfray, P. Schuck, and J. Wambach, 1995, Nucl. Phys. **A581**, 471.
- Arnaldi, R., R. Averbeck, K. Banicz, J. Castor, B. Chaurand, C. Cicalò, A. Colla, P. Cortese, S. Damjanovic, A. David, A. D. Falco, A. Devaux, *et al.* (NA60 Collaboration), 2006, Physical Review Letters **96**, 162302.
- Asakawa, M., T. Hatsuda, and Y. Nakahara, 2001, Prog. Part. Nucl. Phys. **46**, 459.
- Asakawa, M., T. Hatsuda, and Y. Nakahara, 2003, Nucl. Phys. **A715**, 863.
- Asakawa, M., and C. M. Ko, 1993, Phys. Rev. **C48**, 526.
- Asakawa, M., C. M. Ko, P. Levai, and X. J. Qiu, 1992, Phys. Rev. **C46**, 1159.
- Aubert, J. J., U. Becker, P. J. Biggs, J. Burger, M. Chen, G. Everhart, P. Goldhagen, J. Leong, T. McCarriston, T. G. Rhoades, M. Rohde, S. C. C. Ting, *et al.*, 1974, Phys. Rev. Lett. **33**, 1404.
- Barth, J., W. Braun, J. Ernst, K. H. Glander, J. Hannappel, N. Jöpen, H. Kalinowsky, F. Klein, F. Klein, E. Klempt, R. Lawall, J. Link, *et al.*, 2003, The European Physical Journal A - Hadrons and Nuclei **18**(1), 117.
- Batty, C. J., S. F. Biagi, E. Friedman, S. D. Hoath, J. D. Davies, G. J. Pyle, G. T. A. Squier, D. M. Asbury, and A. Guberman, 1979, Nuclear Physics A **322**(2-3), 445.
- Batty, C. J., E. Friedman, and A. Gal, 1983, Nucl. Phys. **A402**, 411.
- Batty, C. J., E. Friedman, and A. Gal, 1997, Phys. Rept. **287**, 385.
- Bernard, V., N. Kaiser, and U.-G. Meissner, 1993, Physics Letters B **309**(3-4), 421.
- Bernard, V., N. Kaiser, and U.-G. Meissner, 1995, Phys. Rev. C **52**(4), 2185.
- Bernard, V., U. G. Meissner, and I. Zahed, 1987, Phys. Rev. Lett. **59**, 966.
- Blobel, V., H. Fesefeldt, H. Franz, B. Hellwig, U. Idschok, J. W. Lamsa, D. Mkemeyer, H. F. Neumann, D. Roedel, W. Schrankel, B. Schwarz, F. Selonke, *et al.*, 1974, Physics Letters B **48**, 73.
- Bloch, F., J. Ahrens, J. Annand, R. Beck, L. Fog, D. Hornidge, S. Janssen, M. Kotulla, B. Krusche, J. McGeorge, *et al.*, 2007, The European Physical Journal A **32**, 219.
- Bochkarev, A. I., and M. E. Shaposhnikov, 1986, Nucl. Phys. **B268**, 220.
- Bonutti, F., P. Camerini, E. Fragiaco, N. Grion, R. Rui, P. Amaudruz, J. Brack, L. Felawka, E. Gibson, G. Hofman, *et al.*, 1996, Physical Review Letters **77**, 603.
- Bonutti, F., P. Camerini, E. Fragiaco, N. Grion, R. Rui, J. T. Brack, L. Felawka, E. F. Gibson, G. Hofman, M. Kermani, E. L. Mathie, S. McFarland, *et al.*, 1997, Phys. Rev. C **55**, 2998.
- Bonutti, F., P. Camerini, E. Fragiaco, N. Grion, R. Rui, J. T. Brack, L. Felawka, E. F. Gibson, G. Hofman, M. Kermani, E. L. Mathie, S. McFarland, *et al.*, 1999, Phys. Rev. C **60**, 018201.
- Bonutti, F., P. Camerini, E. Fragiaco, N. Grion, R. Rui, J. T. Brack, L. Felawka, E. F. Gibson, G. Hofman, M. Kermani, E. L. Mathie, R. Meier, *et al.*, 2000, Nuclear Physics A **677**, 213.
- Bowman, P. O., U. M. Heller, D. B. Leinweber, M. B. Parappilly, A. G. Williams, and J. Zhang, 2005, Phys. Rev. **D71**, 054507.
- Bratkovskaya, E. L., and W. Cassing, 2008, Nuclear Physics A **807**, 214.
- Bratkovskaya, E. L., W. Cassing, R. Rapp, and J. Wambach, 1998, Nuclear Physics A **634**, 168.
- Brown, G. E., M. Harada, J. W. Holt, M. Rho, and C. Sasaki, 2008, eprint 0804.3196.

- Brown, G. E., and M. Rho, 1991, Phys. Rev. Lett. **66**, 2720.
- Brown, G. E., and M. Rho, 1996, Phys. Rept. **269**, 333.
- Brown, G. E., and M. Rho, 2002, Phys. Rept. **363**, 85.
- Buballa, M., 2005, Phys. Rept. **407**, 205.
- Buss, O., L. Alvarez-Ruso, P. Muehlich, and U. Mosel, 2006, Eur. Phys. J. **A29**, 189.
- Cabrera, D., D. Fernandez-Fraile, and A. G. Nicola, 2008, eprint 0809.5237.
- Cabrera, D., E. Oset, and M. J. Vicente Vacas, 2005, Phys. Rev. **C72**, 025207.
- Cabrera, D., L. Roca, E. Oset, H. Toki, and M. J. Vicente Vacas, 2004, Nuclear Physics A **733**, 130.
- Caillon, J. C., and J. Labarsouque, 1993, Phys. Lett. **B311**, 19.
- Camerini, P., E. Fragiaco, N. Grion, S. Piano, R. Rui, J. Clark, L. Felawka, E. F. Gibson, G. Hofman, E. L. Mathie, R. Meier, G. Moloney, *et al.*, 2004, Nuclear Physics A **735**, 89.
- Camerini, P., E. Fragiaco, N. Grion, R. Rui, J. Brack, E. Gibson, G. Hofman, E. Mathie, R. Meier, K. Raywood, *et al.*, 2001, Physical Review C **64**, 067601.
- Caprini, I., G. Colangelo, and H. Leutwyler, 2006, Phys. Rev. Lett. **96**, 132001.
- Cassing, W., and E. L. Bratkovskaya, 1999, Phys. Rept. **308**, 65.
- Chanfray, G., R. Rapp, and J. Wambach, 1996, Phys. Rev. Lett. **76**, 368.
- Chanfray, G., and P. Schuck, 1993, Nucl. Phys. **A555**, 329.
- Chatellard, D., J. P. Egger, E. Jeannet, A. Badertscher, M. Bogdan, P. F. A. Goudsmit, M. Janousch, H. J. Leisi, E. Matsinos, H. C. Schröder, D. Sigg, Z. G. Zhao, *et al.*, 1997, Nuclear Physics A **625**, 855.
- Cheng, M., N. H. Christ, S. Datta, J. Van der Heide, C. Jung, F. Karsch, O. Kaczmarek, E. Laermann, R. D. Mawhinney, C. Miao, P. Petreczky, K. Petrov, *et al.*, 2008, Phys. Rev. **D77**, 014511.
- Chiku, S., and T. Hatsuda, 1998a, Phys. Rev. **D58**, 076001.
- Chiku, S., and T. Hatsuda, 1998b, Phys. Rev. **D57**, 6.
- Cohen, T. D., R. J. Furnstahl, and D. K. Griegel, 1992, Phys. Rev. **C45**, 1881.
- Cozma, M., C. Fuchs, E. Santini, and A. Fässler, 2006, Physics Letters B **640**(4), 170 .
- Damjanovic, S. (NA60 Collaboration), 2007, The European Physical Journal C **49**, 235.
- Damjanovic, S. (NA60 Collaboration), 2008, Journal of Physics G: Nuclear and Particle Physics **35**, 104036 (8pp).
- De Vries, H., C. W. De Jager, and C. De Vries, 1987, Atomic Data and Nuclear Data Tables **36**, 495.
- Delbourgo, R., and M. D. Scadron, 1982, Phys. Rev. Lett. **48**, 379.
- Dey, M., V. L. Eletsky, and B. L. Ioffe, 1990, Phys. Lett. **B252**, 620.
- Djalali, C., 2006, Invited talk at YKIS06, Kyoto.
- Djalali, C., 2008, Private communication.
- Döring, M., and E. Oset, 2008, Phys. Rev. **C77**, 024602.
- Drukarev, E. G., and E. M. Levin, 1991, Prog. Part. Nucl. Phys. **27**, 77.
- Dürr, S., *et al.* (BMW Coll.), 2008, Science **322**, 1224.
- Effenberger, M., E. L. Bratkovskaya, and U. Mosel, 1999, Phys. Rev. C **60**, 044614.
- Effenberger, M., and U. Mosel, 2000, Phys. Rev. C **62**(1), 014605.
- Eichstaedt, F., S. Leupold, U. Mosel, and P. Muehlich, 2007, Prog. Theor. Phys. Suppl. **168**, 495.
- Eletsky, V. L., 1993, Phys. Lett. **B299**, 111.
- Eletsky, V. L., and B. L. Ioffe, 1997, Phys. Rev. Lett. **78**, 1010.
- Erbe, R., *et al.* (Aachen-Berlin-Bonn-Hamburg-Heidelberg-München Collaboration), 1968, Phys. Rev. **175**, 1669.
- Ericson, M., and G. Chanfray, 2007, Eur. Phys. J. **A34**, 215.
- Ericson, M., and T. E. O. Ericson, 1966, Ann. Phys. **36**, 323.
- Ericson, T. E. O., and L. Tauscher, 1982, Phys. Lett. **B112**, 425.
- Ericson, T. E. O., and W. Weise, 1988, *Pions and Nuclei* (Clarendon, Oxford).
- Ernst, C., S. A. Bass, M. Belkacem, H. Stöcker, and W. Greiner, 1998, Phys. Rev. C **58**(1), 447.
- Fernandez-Fraile, D., A. Gomez Nicola, and E. T. Herruzo, 2007, Phys. Rev. **D76**, 085020.
- Fricke, G., C. Bernhardt, K. Heilig, L. Schaller, L. Schellenberg, E. Spera, and C. de Jager, 1995, Atomic Data and Nuclear Data Tables **60**.
- Friedman, E., 2002a, Nucl. Phys. **A710**, 117.
- Friedman, E., 2002b, Phys. Lett. **B524**, 87.
- Friedman, E., M. Bauer, J. Breitschopf, H. Clement, H. Denz, E. Doroshkevich, A. Erhardt, G. J. Hofman, S. Kritichman, R. Meier, G. J. Wagner, and G. Yaari, 2005, Phys. Rev. C **72**(3), 034609.
- Friedman, E., M. Bauer, J. Breitschopf, H. Clement, H. Denz, E. Doroshkevich, A. Erhardt, G. J. Hofman, R. Meier, G. J. Wagner, and G. Yaari, 2004, Phys. Rev. Lett. **93**(12), 122302.
- Friedman, E., and A. Gal, 2007, Phys. Rept. **452**, 89.
- Friedman, E., and G. Soff, 1985, J. Phys. **G11**, L37.
- Friman, B., S. H. Lee, and H.-C. Kim, 1999, Nucl. Phys. **A653**, 91.
- Friman, B., and H. J. Pirner, 1997, Nucl. Phys. **A617**, 496.
- Fukaya, H., *et al.* (JLQCD Coll.), 2009, eprint 0911.5555.
- Galatyuk, T., *et al.* (HADES Collaboration), 2009, eprint 0911.2411.
- Gasser, J., M. A. Ivanov, E. Lipartia, M. Mojziz, and A. Rusetsky, 2002, The European Physical Journal C **26**, 13.
- Gasser, J., H. Leutwyler, and M. E. Sainio, 1991, Phys. Lett. **B253**, 252.
- Gebhardt, W., and U. Krey, 1980, *Phasenübergänge und Kritische Phänomene* (Friedr. Vieweg and Sohn, Braunschweig/Weisbaden).
- Geissel, H., H. Gilg, A. Gillitzer, R. Hayano, S. Hirenzaki, K. Itahashi, M. Iwasaki, P. Kienle, M. Münch, G. Münzenberg, *et al.*, 2002, Physical Review Letters **88**, 122301.
- Gell-Mann, M., and M. Levy, 1960, Nuovo Cim. **16**, 705.
- Gell-Mann, M., R. J. Oakes, and B. Renner, 1968, Phys. Rev. **175**, 2195.
- Gerber, P., and H. Leutwyler, 1989, Nucl. Phys. **B321**, 387.
- Goity, J. L., and H. Leutwyler, 1989, Phys. Lett. **B228**, 517.
- Gotta, D., F. Amaro, D. F. Anagnostopoulos, S. Biri, D. S. Covita, H. Gorke, A. Gruber, M. Hennebach, A. Hirtl, T. Ishiwatari, P. Indelicato, T. Jensen, *et al.*, 2008, Precision Physics of Simple Atoms and Molecules , 165.
- Grion, N., M. Bregant, P. Camerini, E. Fragiaco, S. Piano, R. Rui, E. F. Gibson, G. Hofman, E. L. Mathie, R. Meier, M. E. Sevir, G. R. Smith, *et al.*, 2005, Nuclear Physics A **763**, 80.
- Gross, D. J., 2005, Proc. Nat. Acad. Sci. **102**, 9099.
- Harada, M., Y. Kim, and M. Rho, 2002, Phys. Rev. **D66**, 016003.

- Harada, M., and C. Sasaki, 2002, Phys. Lett. **B537**, 280.
- Harada, M., and C. Sasaki, 2006, Phys. Rev. **D73**, 036001.
- Harada, M., and K. Yamawaki, 2003, Phys. Rept. **381**, 1.
- Hatsuda, T., 1997, in *International conference of soft dilepton production at LBNL*, (http://macdls.lbl.gov/DLS_WWW_Files/DLSWorkshop/prbaskings.html).
- Hatsuda, T., Y. Koike, and S.-H. Lee, 1993, Nucl. Phys. **B394**, 221.
- Hatsuda, T., and T. Kunihiro, 1985, Phys. Rev. Lett. **55**, 158.
- Hatsuda, T., and T. Kunihiro, 1987a, Phys. Lett. **B185**, 304.
- Hatsuda, T., and T. Kunihiro, 1987b, Prog. Theor. Phys. Suppl. **91**, 284.
- Hatsuda, T., and T. Kunihiro, 1994, Phys. Rept. **247**, 221.
- Hatsuda, T., and T. Kunihiro, 2001, eprint nucl-th/0112027.
- Hatsuda, T., T. Kunihiro, and H. Shimizu, 1999, Phys. Rev. Lett. **82**, 2840.
- Hatsuda, T., and S. H. Lee, 1992, Phys. Rev. **C46**, 34.
- Hatsuda, T., S. H. Lee, and H. Shiomi, 1995, Phys. Rev. **C52**, 3364.
- Hatsuda, T., H. Shiomi, and H. Kuwabara, 1996, Prog. Theor. Phys. **95**, 1009.
- Hatsuda, T., M. Tachibana, and N. Yamamoto, 2008, Phys. Rev. **D78**, 011501.
- van Hees, H., and R. Rapp, 2006, Physical Review Letters **97**(10), 102301 (pages 4).
- Herb, S. W., D. C. Hom, L. M. Lederman, J. C. Sens, H. D. Snyder, J. K. Yoh, J. A. Appel, B. C. Brown, C. N. Brown, W. R. Innes, K. Ueno, T. Yamanouchi, *et al.*, 1977, Phys. Rev. Lett. **39**, 252.
- Hernández, E., and E. Oset, 1992, Zeitschrift für Physik A Hadrons and Nuclei **341**, 201.
- Herrmann, M., B. L. Friman, and W. Norenberg, 1993, Nucl. Phys. **A560**, 411.
- Hidaka, Y., O. Morimatsu, T. Nishikawa, and M. Ohtani, 2004, Phys. Rev. **D70**, 076001.
- Hidaka, Y., O. Morimatsu, and M. Ohtani, 2006, Phys. Rev. **D73**, 036004.
- Hirezaki, S., H. Nagahiro, T. Hatsuda, and T. Kunihiro, 2002, Nucl. Phys. **A710**, 131.
- Hirezaki, S., H. Toki, and T. Yamazaki, 1991, Phys. Rev. **C44**, 2472.
- Huber, G. M., G. J. Lolos, Z. Papandreou, A. Shinozaki, E. J. Brash, M. Iurescu, G. Garino, K. Maruyama, K. Maeda, T. Suda, A. Toyofuku, B. K. Jennings, *et al.*, 2003, Phys. Rev. C **68**, 065202.
- Ishikawa, T., D. S. Ahn, J. K. Ahn, H. Akimune, W. C. Chang, S. Daté, H. Fujimura, M. Fujiwara, K. Hicks, T. Hotta, K. Imai, H. Kawai, *et al.*, 2005, Physics Letters B **608**, 215.
- Iwasaki, M., A. Trudel, A. Celler, O. Häusser, R. Hayano, R. Helmer, R. Henderson, S. Hirezaki, K. Jackson, Y. Kuno, *et al.*, 1991, Physical Review C **43**, 1099.
- Janssen, S., W. Doring, V. Metag, and R. Novotny, 2000, Nuclear Science, IEEE Transactions on **47**(3), 798.
- Jean, H. C., J. Piekarewicz, and A. G. Williams, 1994, Phys. Rev. **C49**, 1981.
- Jido, D., T. Hatsuda, and T. Kunihiro, 2001, Phys. Rev. **D63**, 011901.
- Jido, D., T. Hatsuda, and T. Kunihiro, 2008, Physics Letters B **670**, 109 .
- Jin, X.-m., and D. B. Leinweber, 1995, Phys. Rev. **C52**, 3344.
- Kaiser, N., and W. Weise, 2009, Physics Letters B **671**(1), 25338.
- Kapusta, J. I., and E. V. Shuryak, 1994, Phys. Rev. **D49**, 4694.
- Karsch, F., 2002, Lect. Notes Phys. **583**, 209.
- Karsch, F., and E. Laermann, 2003, eprint hep-lat/0305025.
- Kern, D., J. Hernandez, and E. Oset, 2007, The European Physical Journal A **31**, 245.
- Kermani, M., O. Patarakin, G. R. Smith, P. A. Amaudruz, F. Bonutti, J. T. Brack, P. Camerini, L. Felawka, E. Fragaicomo, E. F. Gibson, N. Grión, G. J. Hofman, *et al.*, 1998, Phys. Rev. C **58**, 3431.
- Kienle, P., and T. Yamazaki, 2001, Physics Letters B **514**, 1.
- Kittel, C., 2004, *Introduction to solid state physics* (John Wiley and Sons, New Jersey), 8th edition.
- Klevansky, S. P., 1992, Rev. Mod. Phys. **64**, 649.
- Klingl, F., N. Kaiser, and W. Weise, 1997, Nucl. Phys. **A624**, 527.
- Kogan, I. I., A. Kovner, and M. A. Shifman, 1999, Phys. Rev. **D59**, 016001.
- Koike, Y., and A. Hayashigaki, 1997, Prog. Theor. Phys. **98**, 631.
- Kolomeitsev, E. E., N. Kaiser, and W. Weise, 2003a, Nucl. Phys. **A721**, 835.
- Kolomeitsev, E. E., N. Kaiser, and W. Weise, 2003b, Phys. Rev. Lett. **90**, 092501.
- Konijn, J., C. T. A. M. de Laat, A. Taal, and J. H. Koch, 1990, Nucl. Phys. **A519**, 773.
- Kotulla, M., D. Trnka, P. Mühlich, G. Anton, J. C. S. Bacelar, O. Bartholomy, D. Bayadilov, Y. A. Beloglazov, R. Bogendörfer, R. Castelijns, V. Crede, H. Dutz, *et al.* (CBELSA/TAPS Collaboration), 2008, Physical Review Letters **100**, 192302.
- Krusche, B., 2008, Private communication.
- Kunihiro, T., S. Muroya, A. Nakamura, C. Nonaka, M. Sekiguchi, and H. Wada, 2009, Nuclear Physics B - Proceedings Supplements **186**, 294 , proceedings of the QCD 08, 14th High-Energy Physics International Conference On Quantum ChromoDynamics.
- Kurasawa, H., and T. Suzuki, 1990, Prog. Theor. Phys. **84**, 1030.
- Kwon, Y., M. Procura, and W. Weise, 2008, eprint 0803.3262.
- de Laat, C., A. Taal, J. Konijn, P. David, H. Hänscheid, F. Risse, C. Rösler, W. Schrieder, and C. Petitjean, 1991, Nuclear Physics A **523**, 453.
- Leupold, S., W. Peters, and U. Mosel, 1998, Nucl. Phys. **A628**, 311.
- Leutwyler, H., 2008, AIP Conf. Proc. **1030**, 46.
- Li, G. Q., C. M. Ko, and G. E. Brown, 1995, Phys. Rev. Lett. **75**, 4007.
- Loiseau, B., T. E. O. Ericson, and A. W. Thomas, 2001, Nuclear Physics A **684**, 380.
- Lolos, G., G. Huber, Z. Papandreou, F. Farzanpay, M. Iurescu, A. Weierman, G. Garino, K. Maruyama, K. Maeda, A. Shinozaki, *et al.*, 1998, Physical Review Letters **80**, 241.
- Marín, A. (CERES Collaboration), 2004, Journal of Physics G: Nuclear and Particle Physics **30**, S709.
- Mecking, B. A., *et al.* (CLAS Collaboration), 2003, Nucl. Instr. and Meth. A **503**, 513.
- Meissner, U. G., J. A. Oller, and A. Wirzba, 2002, Annals Phys. **297**, 27.
- Messchendorp, J., S. Janssen, M. Kotulla, J. Ahrens, J. Annand, R. Beck, F. Bloch, G. Caselotti, L. Fog, D. Hornidge, *et al.*, 2002, Physical Review Letters **89**, 222302.

- Messchendorp, J. G., A. Sibirtsev, W. Cassing, V. Metag, and S. Schadmand, 2001, *The European Physical Journal A* **11**, 95.
- Metag, V., 2008a, *Progress in Particle and Nuclear Physics* **61**, 245.
- Metag, V., 2008b, Private communication.
- Miransky, V. A., 2002, eprint hep-ph/0208180.
- Mosel, U., 2008, *MODERN PHYSICS LETTERS A* **23**, 2371.
- Muehlich, P., T. Falter, and U. Mosel, 2004, *The European Physical Journal A* **20**, 499.
- Muehlich, P., and U. Mosel, 2006, *Nucl. Phys.* **A773**, 156.
- Muroya, S., A. Nakamura, C. Nonaka, and T. Takaishi, 2003, *Prog. Theor. Phys.* **110**, 615.
- Muto, R., J. Chiba, H. En'yo, Y. Fukao, H. Funahashi, H. Hamagaki, M. Ieiri, M. Ishino, H. Kanda, M. Kitaguchi, S. Mihara, K. Miwa, *et al.* (KEK-PS E325 Collaboration), 2007, *Physical Review Letters* **98**, 042501.
- Nagahiro, H., D. Jido, and S. Hirenzaki, 2005, *Nucl. Phys.* **A761**, 92.
- Nambu, Y., 1960, *Phys. Rev. Lett.* **4**, 380.
- Nambu, Y., 1966, in *Preludes in Theoretical Physics, in honor of V. F. Weisskopf*, edited by A. de Shalit, H. Feshbach, and L. van Hove (North-Holland, Amsterdam), p. 133.
- Nambu, Y., and G. Jona-Lasinio, 1961a, *Phys. Rev.* **122**, 345.
- Nambu, Y., and G. Jona-Lasinio, 1961b, *Phys. Rev.* **124**, 246.
- Nara, Y., N. Otuka, A. Ohnishi, K. Niita, and S. Chiba, 1999, *Phys. Rev. C* **61**, 024901.
- Naruki, M., Y. Fukao, H. Funahashi, M. Ishino, H. Kanda, M. Kitaguchi, S. Mihara, K. Miwa, T. Miyashita, T. Murakami, T. Nakura, F. Sakuma, *et al.* (KEK-PS E325 Collaboration), 2006, *Physical Review Letters* **96**, 092301.
- Nieves, J., E. Oset, and C. Garcia-Recio, 1993, *Nuclear Physics A* **554**(4), 509.
- Novotny, R., 1991, *IEEE Transactions on Nuclear Science* **38**, 379.
- Ohnishi, A., N. Kawamoto, and K. Miura, 2008, *Mod. Phys. Lett.* **A23**, 2459.
- Oller, J. A., E. Oset, and A. Ramos, 2000, *Prog. Part. Nucl. Phys.* **45**, 157.
- Ozawa, K., H. En'yo, H. Funahashi, M. Kitaguchi, M. Ishino, H. Kanda, S. Mihara, T. Miyashita, T. Murakami, R. Muto, *et al.* (KEK-PS E325 Collaboration), 2001, *Physical Review Letters* **86**, 5019.
- Patkos, A., Z. Szep, and P. Szepefalusy, 2002, *Phys. Rev.* **D66**, 116004.
- Pennington, M. R., 2007, *Mod. Phys. Lett.* **A22**, 1439.
- Pisarski, R. D., 1982, *Phys. Lett.* **B110**, 155.
- Pisarski, R. D., and M. Tytgat, 1996, *Phys. Rev.* **D54**, 2989.
- Politzer, H. D., 2005, *Proc. Nat. Acad. Sci.* **102**, 7789.
- Porter, R. J., S. Beedoe, R. Bossingham, M. Bougteb, W. B. Christie, J. Carroll, W. G. Gong, T. Hallman, L. Heilbronn, H. Z. Huang, G. Igo, P. Kirk, *et al.*, 1997, *Phys. Rev. Lett.* **79**, 1229.
- Post, M., S. Leupold, and U. Mosel, 2004, *Nucl. Phys.* **A741**, 81.
- Prelovsek, S., 2008, eprint 0804.2549.
- Rapp, R., G. Chanfray, and J. Wambach, 1997, *Nucl. Phys.* **A617**, 472.
- Rapp, R., and J. Wambach, 2000, *Adv. Nucl. Phys.* **25**, 1.
- Roberts, C. D., and S. M. Schmidt, 2000, *Prog. Part. Nucl. Phys.* **45**, S1.
- Roca, L., E. Oset, and M. J. Vicente Vacas, 2002, *Physics Letters B* **541**, 77.
- Ruppert, J., T. Renk, and B. Muller, 2006, *Phys. Rev.* **C73**, 034907.
- Saito, K., T. Maruyama, and K. Soutome, 1989, *Phys. Rev.* **C40**, 407.
- Saito, K., and A. W. Thomas, 1995, *Phys. Rev.* **C51**, 2757.
- Saito, K., K. Tsushima, and A. W. Thomas, 1997a, *Phys. Rev. C* **56**, 566.
- Saito, K., K. Tsushima, and A. W. Thomas, 1997b, *Phys. Rev. C* **55**, 2637.
- Saito, K., K. Tsushima, and A. W. Thomas, 2007, *Prog. Part. Nucl. Phys.* **58**, 1.
- Salapura, P., *et al.* (HADES Collaboration), 2004, *Progress in Particle and Nuclear Physics* **53**, 49.
- Schröder, H., A. Badertscher, P. Goudsmit, M. Janousch, H. Leisi, E. Matsinos, D. Sigg, Z. Zhao, D. Chatellard, J. Egger, *et al.*, 2001, *The European Physical Journal C* **21**, 473.
- Schuck, P., W. Norenberg, and G. Chanfray, 1988, *Z. Phys.* **A330**, 119.
- Seki, R., and K. Masutani, 1983, *Phys. Rev.* **C27**, 2799.
- Sekimoto, M., J. Chiba, H. Funahashi, H. Hamagaki, M. Ieiri, M. Ishino, M. Kitaguchi, S. Mihara, T. Miyashita, T. Murakami, R. Muto, M. Naruki, *et al.* (KEK-PS E325 Collaboration), 2004, *Nucl. Instr. and Meth. A* **516**, 390.
- Shekhter, K., C. Fuchs, A. Faessler, M. Krivoruchenko, and B. Martemyanov, 2003, *Phys. Rev. C* **68**(1), 014904.
- Shifman, M. A., A. I. Vainshtein, and V. I. Zakharov, 1979a, *Nucl. Phys.* **B147**, 448.
- Shifman, M. A., A. I. Vainshtein, and V. I. Zakharov, 1979b, *Nucl. Phys.* **B147**, 385.
- Shiomi, H., and T. Hatsuda, 1994, *Phys. Lett.* **B334**, 281.
- Shyam, R., and U. Mosel, 2003, *Phys. Rev. C* **67**, 065202.
- Sibirtsev, A., V. Hejny, H. Stroher, and W. Cassing, 2000, *Phys. Lett.* **B483**, 405.
- Smith, G. R., P. A. Amaudruz, J. T. Brack, L. Felawka, A. Gorelov, R. A. Henderson, D. F. Ottewell, P. Vincent, Y. Wu, F. Bonutti, P. Camerini, N. Grion, *et al.*, 1995, *Nucl. Instr. and Meth. A* **362**, 349.
- Starostin, A., H. Staudenmaier, C. Allgower, V. Bekrenev, E. Berger, W. Briscoe, M. Clajus, J. Comfort, K. Craig, D. Grosnick, *et al.*, 2000, *Physical Review Letters* **85**, 5539.
- Suganuma, H., and T. Tatsumi, 1991, *Ann. Phys.* **208**, 470.
- Suzuki, K., M. Fujita, H. Geissel, H. Gilg, A. Gillitzer, R. Hayano, S. Hirenzaki, K. Itahashi, M. Iwasaki, P. Kienle, *et al.*, 2004, *Physical Review Letters* **92**, 72302.
- Tabaru, T., H. En'yo, R. Muto, M. Naruki, S. Yokkaichi, J. Chiba, M. Ieiri, O. Sasaki, M. Sekimoto, K. Tanaka, *et al.* (KEK-PS E325 Collaboration), 2006, *Physical Review C* **74**, 25201.
- Tauscher, L., 1971, -meson nucleus interaction, proceedings of the International Seminar on -Meson Nucleus Interaction Strasbourg 1971, CNRS-Strasbourg (unpublished), p. 45.
- Terashima, S., H. Sakaguchi, H. Takeda, T. Ishikawa, M. Itoh, T. Kawabata, T. Murakami, M. Uchida, Y. Yasuda, M. Yosoi, J. Zenihiro, H. P. Yoshida, *et al.*, 2008, *Physical Review C (Nuclear Physics)* **77**(2), 024317 (pages 10).
- Thomas, R., T. Hilger, and B. Kampf, 2007, *Nucl. Phys.* **A795**, 19.
- Thomas, R., S. Zschocke, and B. Kampf, 2005, *Phys. Rev. Lett.* **95**, 232301.
- Thorsson, V., and A. Wirzba, 1995, *Nucl. Phys.* **A589**, 633.
- Toia, A. (PHENIX Collaboration), 2006, *Nuclear Physics A* **774**, 743.
- Toia, A. (PHENIX Collaboration), 2007, *The European Physical Journal C* **49**, 243.

- Toia, A., 2008, Journal of Physics G: Nuclear and Particle Physics **35**(10), 104037 (9pp).
- Toki, H., S. Hirenzaki, and T. Yamazaki, 1991a, Nuclear Physics A **530**, 679.
- Toki, H., S. Hirenzaki, T. Yamazaki, and R. Hayano, 1991b, Nuclear Physics A **527**, 455.
- Toki, H., S. Hirenzaki, T. Yamazaki, and R. S. Hayano, 1989, Nucl. Phys. **A501**, 653.
- Toki, H., and T. Yamazaki, 1988, Phys. Lett. **B213**, 129.
- Tomozawa, Y., 1966, Nuovo Cim. **46A**, 707.
- Toublan, D., 1997, Phys. Rev. **D56**, 5629.
- Trnka, D., G. Anton, J. C. S. Bacelar, O. Bartholomy, D. Bayadilov, Y. A. Beloglazov, R. Bogendörfer, R. Castelijns, V. Crede, H. Dutz, A. Ehmans, D. Elsner, *et al.* (CBELSA/TAPS Collaboration), 2005, Physical Review Letters **94**, 192303.
- Trzcińska, A., J. Jastrzębski, P. Lubiński, F. J. Hartmann, R. Schmidt, T. von Egidy, and B. Klos, 2001, Phys. Rev. Lett. **87**, 082501.
- Umemoto, Y., S. Hirenzaki, K. Kume, and H. Toki, 2000, Phys. Rev. **C62**, 024606.
- Usai, G. and others (NA60 Collaboration), 2005, The European Physical Journal C **43**, 415.
- Vafa, C., and E. Witten, 1984, Nucl. Phys. **B234**, 173.
- Vogl, U., and W. Weise, 1991, Prog. Part. Nucl. Phys. **27**, 195.
- Volkov, M. K., E. A. Kuraev, D. Blaschke, G. Ropke, and S. M. Schmidt, 1998, Phys. Lett. **B424**, 235.
- Watanabe, Y., K. Fukushima, and T. Hatsuda, 2004, Prog. Theor. Phys. **111**, 967.
- Weinberg, S., 1966, Phys. Rev. Lett. **17**, 616.
- Weinberg, S., 1990, Phys. Rev. Lett. **65**, 1177.
- Weise, W., 2000, Acta Phys. Polon. **B31**, 2715.
- Weise, W., 2001a, Nucl. Phys. **A690**, 98.
- Weise, W., 2001b, Nuclear Physics A **690**, 98.
- Wilczek, F., 2005, Proc. Nat. Acad. Sci. **102**, 8403.
- Wilson, K. G., 2005, Nucl. Phys. Proc. Suppl. **140**, 3.
- Wood, M. H., R. Nasseripour, D. P. Weygand, C. Djalali, C. Tur, U. Mosel, P. Muehlich, G. Adams, M. J. Amarian, P. Ambrozewicz, M. Anghinolfi, G. Asryan, *et al.* (CLAS Collaboration), 2008, Physical Review C **78**, 015201.
- Wu, C., J. Barth, W. Braun, J. Ernst, K. H. Glander, J. Hannappel, N. Jpen, H. Kalinowsky, F. J. Klein, F. Klein, E. Klempt, R. Lawall, *et al.*, 2005, The European Physical Journal A - Hadrons and Nuclei **23**(2), 317.
- Yagi, K., T. Hatsuda, and Y. Miake, 2005, *Quark-gluon plasma: From big bang to little bang* (Cambridge Univ. Press, London).
- Yamazaki, T., R. Hayano, K. Itahashi, K. Oyama, A. Gillitzer, H. Gilg, M. Knulle, M. Munch, P. Kienle, W. Schott, *et al.*, 1996, Zeitschrift fur Physik A **355**, 219.
- Yamazaki, T., and S. Hirenzaki, 2003, Physics Letters B **557**, 20.
- Yamazaki, T., S. Hirenzaki, R. S. Hayano, and H. Toki, 2008, to appear in Physics Reports .
- Yegneswaran, A., S. Beedoe, J. Bystricky, J. Carroll, S. Christo, G. Claesson, P. Force, R. Fulton, J. F. Gilot, J. Gordon, T. Hallman, D. L. Hendrie, *et al.*, 1990, Nucl. Instr. and Meth. A **290**, 61.
- Yokokawa, K., T. Hatsuda, A. Hayashigaki, and T. Kunihiro, 2002, Phys. Rev. **C66**, 022201.
- Zemp, P., 2003, in *Proc. of Chiral Dynamics 2003*, *arXiv: hep-ph/0311212v1*, p. 128.